Alma Mater Studiorum - Università di Bologna

DOTTORATO DI RICERCA IN

ASTROFISICA

Ciclo 35

Settore Concorsuale: 02/C1 - ASTRONOMIA, ASTROFISICA, FISICA DELLA TERRA E DEI PIANETI

Settore Scientifico Disciplinare: FIS/05 - ASTRONOMIA E ASTROFISICA

CROSS-POPULATION RADIO GALAXIES AS A TEST OF THE JET-ACCRETION RELATIONSHIP

Presentata da: Duccio Macconi

Coordinatore Dottorato

Andrea Miglio

Supervisore

Paola Grandi

Co-supervisore

Cristian Vignali

Esame finale anno 2023

Abstract

Radio galaxies (RGs) are extremely relevant in addressing important unknowns concerning the interaction among black hole accretion, radio jets, and the environment. RGs are characterized by two accretion modes, as measured by their optical excitation lines: radiatively inefficient (namely LERGs) and radiatively efficient (named HERGs). From the radio point of view, RGs show two main radio morphologies, edge-darkened (FRIs) and edge-brightened (FRIIs). Such morphological classification neatly translates into a radio power difference, with FRIIs characterized by larger values than FRIs. A strong link between the accretion mode and the radio morphology was also suggested: the higher the accretion rate, the more powerful jets are launched. The observation of FRII-LERGs, i.e., sources with an inefficient engine and edge-brightened radio emission, broke the standard accretion-ejection scheme. For this reason, they constitute a suitable population to explore how accretion and ejection are linked and evaluate the environment's role in shaping the jet at large distances. Over the years, many hypotheses have been proposed to explain the AGN jets' power and morphology variety. Some focus on the nuclear properties, others on the jet interaction with the medium through which the plasma propagates. These solutions are not mutually exclusive. However, it still needs to be determined which of them plays the key role. To shed light on this issue, we performed a multiwavelength study of different RGs catalogs spanning from Jy to mJy flux densities. At first, we investigated the X-ray properties of a complete sample of 19 FRII-LERGs belonging to the 3CR catalog (flux density threshold at ~ 9 Jy, Bennett 1962), exploiting Chandra and XMM-Newton archival data. Our results highlight the FRII-LERGs intermediate properties in terms of moderate intrinsic column density ($N_H \approx 10^{22} cm^{-2}$) and Eddington-scaled X-ray luminosity compared to the classical FRIs sand FRIIs. At least two hypotheses can be invoked to explain the X-ray results of Jy FRII-LERGs: (i) they are evolving from classical FRIIs because of the depletion of accreting cold gas in the nuclear region, while the extended radio emission is the heritage of a past efficiently accreting activity; (ii) the nuclei of FRII-LERGs, while not as powerful as in classic FRII-HERGs, can still form FRII morphologies due, for instance, to favorable environmental conditions. As a successive step, we explored the myJ sky by studying optical-radio properties of hundreds RGs at $z < 0.3$ observed by both deep radio FIRST/NVSS (Condon et al. 1998; Becker et al. 1995) and optical SDSS (Abazajian et al. 2009) surveys (i.e., the Best and Heckman 2012 sample). In particular, our statistical study, limited to ($z \leq 0.15$) (FR catalog, Capetti et al. 2017b,a), shows that most nearby mJy objects are in a late stage of their life. FRII-LERGs appear more similar to the old FRI-LERGs than to the young FRII-HERGs. Although these results point towards an evolutive scenario, the time scales related to nuclear changes, star population aging, and large kpc/Mpc radio structure modification do not agree. We then reconsider the possibility that the observed differences could be intrinsic. Actually, LERGs with similar masses and accretion rates (FRI-LERG and FRII-LERGs) can expel jets of different power. We speculated that different black hole properties (spin and magnetic field at its horizon) could determine the observed spread in jet luminosity. The last question to be addressed was the role of the Mpc environment. A galaxy clusters sample built by Wen and Han 2015 using the SDSS survey allowed us to investigate the habitat of 7219 RGs belonging to the Best and Heckman 2012 sample up to $z < 0.3$. The most astonishing result is the preference of RGs to live in poor environments. This is also true for FRI-LERGs, which generally are thought to lie in the cluster center preferentially. The observational differences in the RG classes are still present if only the objects outside the clusters are considered, strongly reducing the impact of the surrounding medium in splitting RGs into different radio/optical classes.

Contents

Chapter 1

Introduction

1.1 Active Galactic Nuclei

1.1.1 An historical introduction

Active Galactic Nuclei (hereafter AGN) represent extremely energetic astrophysical phenomena powered by accretion onto supermassive black holes (SMBHs) at the center of galaxies. Every massive galaxy is found to host at its center a BH with mass of $\approx 10^6$–10^9 $M_\odot$. The BH mass is found to depend on the galaxy dynamics (Magorrian et al., 1998; Tremaine et al., 2002; McConnell et al., 2011), suggesting a strong AGN/galaxy co-evolution (see Kormendy and Ho, 2013, for a complete review on co-evolution). The discovery of SMBHs, lying at the center of nearby galaxies (Kormendy and Richstone, 1995), supported the theory that SMBHs are the central engine for the AGN emission through gravitational accretion phenomena (Salpeter, 1964; Lynden-Bell, 1978). High-excitation nuclear emission lines were associated for the first time by Seyfert (1943) to optical spectra of spiral nebulae (see Figure 1.1) in the form of strong and broad emission lines. However, the interest in AGN grew considerably when quasi-stellar objects (QSOs) were discovered for the first time and associated with high-redshift galaxies, becoming the brightest and more distant objects known (Schmidt, 1963).

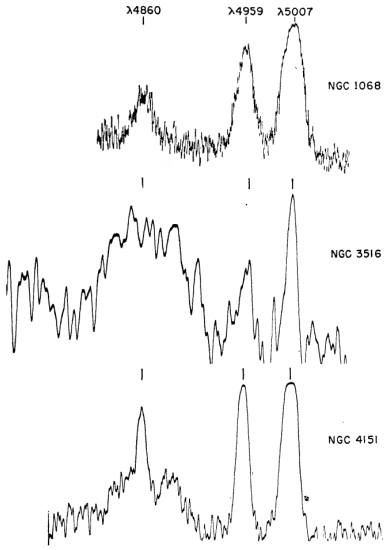

Figure 1.1: First optical spectra of Seyfert 1 and 2 optical spectra produced by Seyfert (1943). The three brightest nuclei in their sample are reported: NCG 1068, NGC 3516, and NGC 4151. The highlighted emission lines are, from left to right, Hβ (4861 Å), and the [OIII] doublet (4959 and 5007 Å).

Even if all massive galaxies have a SMBH, only a small percentage of galaxies are found to host an AGN in the local Universe: $\lesssim 1\%$ (Padovani et al., 2017). These peculiar sources can emit over the entire electromagnetic spectrum, from the radio band up to the γ-rays.

AGN showing broad and narrow optical emission lines are defined as type 1 AGN. Conversely, type 2 AGN are found to show only narrow lines (both permitted and forbidden). The observation of sources less luminous than Seyfert galaxies and characterized by narrow low-ionization lines (LINERS; Heckman 1980) revealed later that an optical classification based on the lines' width was insufficient to describe the AGN variety. Thus, a more quantitative approach became necessary. In this regard, Baldwin et al. (1981) built diagnostic diagrams (hereafter BPT diagrams) using the relative intensities of some of the strongest optical narrow emission-line components. Depending on the predominant excitation mechanism at work, a galaxy is expected to occupy a different position in the diagram, distinguishing between stellar (e.g., planetary nebulae, HII regions) and non-stellar excitation processes (photoionization and shock-heated, see Figure 1.2), with LINERs occupying the right part of the diagram and QSOs/Seyferts the upper part. Since then, other diagrams were built using different line ratios, thus becoming powerful tools to distinguish LINERs, Seyfers/QSOs, and normal galaxies with intense stellar activity (starburst galaxies). This is further discussed in Section 2.2.3.

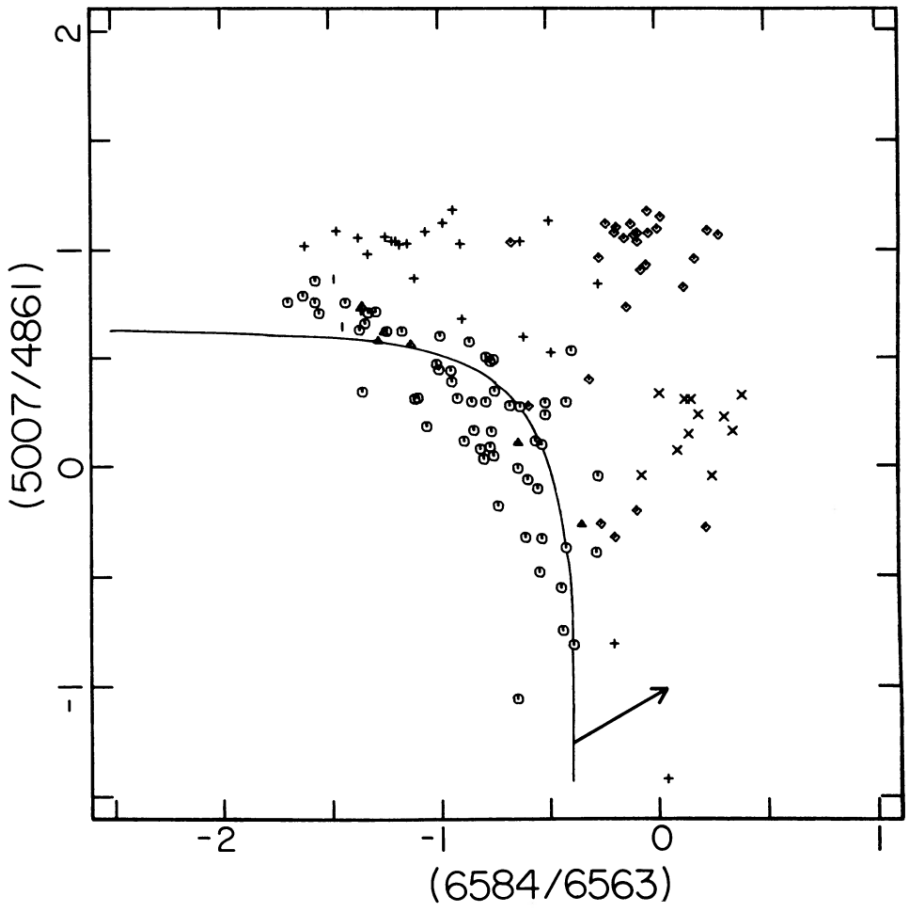

Figure 1.2: Emission-line ratio as originally reported by Baldwin et al. (1981): [NII] at 6584 Å / Hα at 6563 Å vs. [OIII] at 5007 Å / Hβ at 4861 Å. The dataset shows different symbols indicating different excitation mechanisms responsible for the emitting lines, as classified in different works in literature. They can be due to either stellar excitation mechanisms (H II regions photoionized by O and B stars, planetary nebulae) or not (photoionization by a power-law continuum source, shock-heated galaxies): octagons indicate normal HII regions, triangles are galaxies with detached extragalactic HII regions, "+" is for planetary nebulae, vertical bars are upper limits on the [OIII]/Hβ ratio, diamonds are due to power-law photoionization and crosses are for shock-heated galaxies.

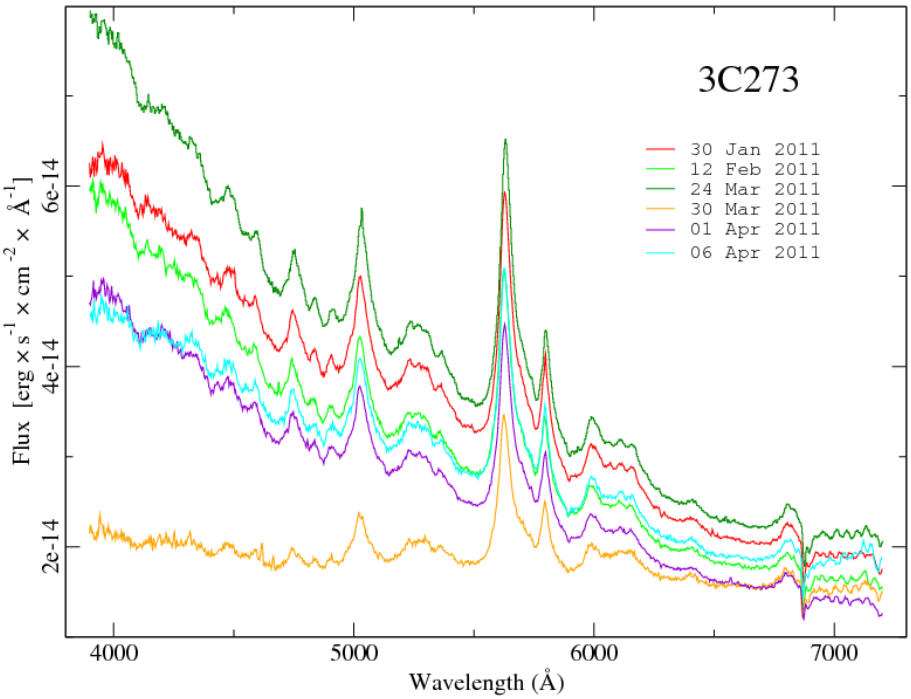

Figure 1.3: Example of strong optical spectral variability of the famous AGN 3C 273 (Schmidt, 1963). Observations were carried out at the Observatorio Astrofisico Guillermo Haro ((OAGH), Patiño-Álvarez et al., 2013).

Another fundamental AGN property was discovered to be their capability of very rapid variations in the emission features (down to daily variations, see Figure 1.3). Thus, a fundamental ingredient in AGN studies is also the timing: an AGN observed in different epochs can show different features and power. As discussed in the following Section, both AGN orientation and intrinsic phenomena (e.g., absorption, accretion rate) can be responsible for it.

A small percentage of AGN were also found to show strong radio emission (now it is known that they are less than 1%, Padovani et al. 2017).

Many works in literature have analyzed the properties of AGN using simultaneous radio and optical observations (see Figure 1.4, Bolton et al. 1949; Matthews et al. 1964). Radio-emitting and radio-silent AGN were found to be characterized by similar optical spectra.

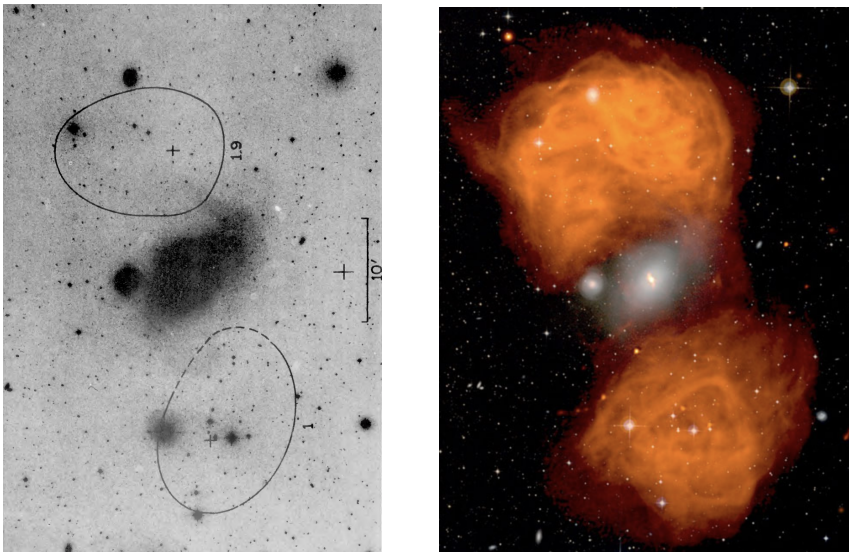

Figure 1.4: Two images of Fornax A, a well-known radio-loud AGN. In the *left panel*, the radio contours calculated more than 50 years ago from Owens Valley Radio Observatory (OVRO) observations are superimposed as black curves to the optical emission (3000-6000 Å) half-intensity (Matthews et al., 1964); *right panel*: the same source with radio emission (orange color) over the optical emission is observed with a new generation interferometer: the Very Large Array (VLA, Credit NRAO).

Although AGN can be divided into two main classes based on their radio power, i.e., radio-loud and radio-quiet AGN (hereafter RL and RQ, see below for a couple of definitions), a large quantity of different AGN classes were defined, depending on the observing band. Different definitions of "radio loudness" have been given over the years. It was initially based on the AGN radio power only (Peacock et al., 1986); later, it was measured as the ratio of flux densities in two different bands, e.g., radio vs. optical band ($R = \frac{F_{5\ GHz}}{F_B} > 10$, Kellermann et al., 1989). More recently, Terashima and Wilson (2003) proposed a definition based on radio vs. X-ray emission: $log\ R = \frac{L_{core}(5GHz)}{L_{core}(2-10keV)} \geq -4.5$. The latter definition, based on radio/X-ray luminosities, was found to be less affected by dust extinction (which is particularly relevant in the optical band) and, thus, it is a more efficient way to characterize also obscured AGN. However, also the X-ray band can suffer from significant gas obscuration and this could alter the robustness of this radio loudness definition. For this reason, it was proposed that such a definition can be valid only for type 1 AGN, where the extinction/obscuration phenomena are not present or typically negligible (Bonzini et al., 2013). To avoid misclassifications, in particular for the class of type 2 AGN, Padovani (2016) proposed to leave the obsolete nomenclature of RL and RQ AGN by using "jetted" and "non-jetted" AGN, since the jet presence/absence represents the discriminant factor between the two classes of AGN.

1.1.2 AGN topography

AGN consists of different components:

- **Central Super Massive Black Hole (SMBH):** it is the AGN engine accreting matter from

the surrounding. Its mass can range between $\approx 10^6 M_\odot$ and $\approx 10^9 M_\odot$. A reference size of the BH is the gravitational radius, which can be defined as $r_g = GM_{BH}/c^2$ (where G is the gravitational constant and c is the speed of light). It can be described broadly as the region from which the light cannot escape. The SMBH is the AGN engine: its gravitational potential energy is converted into radiation through the infalling gas ($L_{rad} = \varepsilon \dot{M}_{BH} c^2$, where ε represents the process efficiency, $\dot{M}_{BH}$ is the mass accretion rate and c is the speed of light [1]) and in the case of radio-loud also in jet kinetic ($L_{kin} = \eta \dot{M}_{BH} c^2$, where η is the efficiency). Given a specific M_{BH}, the maximum accretion luminosity (i.e., the maximum luminosity produced by radiative emission phenomenon, above which the radiative pressure overwhelms gravity: this quantity is referred to as Eddington limit) is defined by theory as the Eddington luminosity: $L_{Edd} = 1.26 \times 10^{38} M/M_\odot$. Thus, the accreting luminosity can be rescaled by the Eddington one (L/L_{Edd}) and used as a proxy of the accretion rate. Two other ingredients characterize the SMBH: the spin (J) and the charge (Q). The last one is assumed as 0, since the BH is considered neutral. Instead, J can span between 0 and 1, representing respectively the non-rotating ($J = 0$, Schwarzschild metric) and maximally rotating BH ($J = 1$, Kerr metric);

- **Accretion disc:** it is a viscous disc of gas accreting onto the central SMBH. It is responsible for the continuum of thermal emission in the optical/UV band. The accretion causes friction that heats the gas. The most famous disc model is the Shakura-Sunyaev Disc (SSD,Shakura and Sunyaev 1973). It is characterized by an optically thick, geometrically thin configuration and by a high accretion rate ($> 1\%$ L_{Edd}). Its temperature spans from $\approx 10^4$ to 10^6 K, depending on the distance from the SMBH. The continuum emission is the sum of black bodies with different temperatures. The peak emission depends on the BH mass. The emission usually peaks below 4000 Å and is named "Big Blue Bump" (BBB). Its ability to cool down and emit radiation constitutes the bulk of its energetic output;

- **Hot Corona:** composed of optically thin highly-ionized gas, it is characterized by a temperature of about 10^{8-9} K. The corona is thought to be located above the accreting structure (within a few tens of gravitational radii) and to be responsible for the primary X-ray continuum emission due to thermal Comptonization (Haardt and Maraschi, 1991) of optical/UV photons coming from the disc. The photon energy distribution is described by a power-law in the form $N(E) = N_0 E^{-\Gamma}$, where Γ is the photon index, with typical values of 1.6-1.9 (e.g., Piconcelli et al., 2005). The power-law comprises the “overlap" of many orders of scattering events (both single or multiple): photons can be upscattered until their energy approaches the electron thermal energy ($E_{photon} \approx E_{electrons}$). This phenomenon produces a cut-off of the spectrum at high energy, which is used to estimate the electron temperature. The X-ray photons produced by the hot corona are responsible for two other features in the hardest part of the X-ray spectrum: (i) the “Compton hump" (also named reflection hump), a feature in the 20-50 keV range produced by Compton down-scattering of the primary X-ray power-law photons by the disc. A fraction of the hot corona X-ray photons can impact the disc and be reprocessed by its cold gas, producing the typical broad X-ray hump (Lightman and White, 1988); (ii) the Fe $K\alpha$ emission line, produced by fluorescence. When X-ray photons ($E > 7.1$ keV) irradiate a neutral Fe atom, an electron in the K-shell (n=1) is removed. Another electron from the L-shell drops into the K-shell to reach a lower

[1] In RQ AGN $L_{rad} \approx L_{acc}$

atomic energy state, thus producing a photon with an energy of 6.4 keV; conversely, if the electron moves from the higher M-shell level to the K-shell, the emitted energy is 7.05 keV and the line is called Fe $K\beta$. The Fe $K\alpha$ line can be shaped by Doppler and gravitational effects if produced in the SMBH vicinity (Fabian et al., 2000);

- **Broad Line Region (BLR):** within $\approx (1-10) \times 10^{17}$ cm from the center, it is thought to comprise a collection of warm dense clouds (with density values up to 10^{10}cm^{-3}) at 10^4 K excited/ionized by the AGN central emission. The high density allows the presence of permitted lines only, while the proximity to the SMBH causes high-speed rotation of clouds ($\Delta v \approx 10^4$ km s^{-1}) and, consequently, the broadening of spectral lines caused by the Doppler effect. This region is responsible of the broad lines in the optical spectra;

- **Torus:** its distance from the SMBH can range from a few pc to tens of pc. It is an optically thick structure, primarily composed of dust with a still debated geometry: it can be either clumpy or smooth (or a combination of the two), although the clumpy distribution of clouds is currently favored (e.g., Burtscher et al., 2013). In Circinus galaxy (Tristram et al., 2007) and NGC 1068 (Raban et al., 2009), very well-studied in the mid-IR band, the torus is resolved into a large, almost round, structure containing a compact disc component; this complex structure must be clumpy to explain the low surface brightness. The torus is responsible for the mid-IR emission via optical/UV/X-rays photon absorption (i.e., dust reprocessing). In general, the peak of this emission is in the mid-IR band at wavelengths of 10-20 μm (the so-called "IR bump"), corresponding to a temperature $\leq$ 1000 K, and such emission is more marked the more the AGN is obscured in the optical band. To have a dusty torus structure, the dust grains' temperature has to be below their sublimation temperature ($\leq$ 1000 K). It implies that the more the AGN is powerful in emitting photons (the so-called radiative pressure), the more the cold dusty torus must be distant from the center to avoid sublimation (as suggested by Lawrence, 1991);

- **Narrow Line Regions (NLR):** they occupy a farther region from the center with respect to BLR, reaching distances of 100-1000 pc. They are composed of low-density clouds ($10^3 - 10^4 cm^{-3}$) which emit permitted and forbidden narrow lines ($\Delta v \leq 10^3$ km s^{-1}) in the optical spectrum. It is important to note that, since this region is at a larger distance from the center than the torus, its properties are isotropic and not affected by dust extinction. They represent the farthest structures still ionized/excited by the AGN central photons. Many emission lines coming from this region are important, as the [OIII] line at 5007 Å , which is considered a powerful tracer of the central accreting-structure efficiency ($L_{bolometric} = 3500 \times L_{[OIII]}$). This line has a limited contribution from star-formation processes and it is usually the strongest feature in the optical spectra of type 2 AGN (Heckman et al., 2004);

- **Jets:** collimated beams of non-thermal plasma ejected by the central AGN regions. They can reach large distances (beyond the host-galaxy size, up to Mpc scales). In the radio band, they emit through the synchrotron mechanism. The fundamental ingredients are relativistic particles (electrons) spiraling around magnetic field lines. Because of the continuous change of the electrons' direction of motion, they emit. For each particle, the emission is at a specific frequency ($\nu \propto BE^2$, where ν is the characteristic emitting frequency, B is the magnetic field intensity, and E is the particle energy). Given that the energy distribution of (non-thermal) electrons can be represented by a power-law in the form of $N(E) \propto E^{-\delta}$

(where δ is the electron energy index), the cumulative synchrotron emission reproduces a power-law spectrum in the radio band (i.e., in the MHz-GHz frequency interval): $F = k\nu^{-\alpha}$, where F is the flux density at the frequency ν, k is a constant and $\alpha = (\delta - 1)/2$ represents the radio spectral index. However, jets can also be detected in different bands up to γ-rays (E>100 MeV). The most relevant mechanism in this band is the Inverse Compton (IC) scattering: photons are up-scattered to high energies when interacting with relativistic electrons. Such seed photons can either come from external regions (External Compton) or be produced by the relativistic electron themselves via the synchrotron mechanism (Synchrotron Self Compton, SSC). In the former case, the IC spectral distribution depends on the seed photons' energy distribution. In the SSC case, the power-law spectral index is the same as the synchrotron one. In the case of single scattering, the final frequency of the scattered photon relates to the initial one as $\nu_f \propto \gamma^2 \nu_i$, in which γ is the Lorentz factor: $\gamma = \sqrt{1-\beta^2}$, with $\beta = \frac{v}{c}$. These structures, typical of only RL AGN, will be discussed more deeply in the following Sections, being the main topic of this thesis.

The AGN regions discussed above can be "recovered" in the Spectral Energy Distribution (SED) of a typical AGN from radio to γ-ray bands, as shown in Figure 1.5. The SED is the sum of different components, each corresponding to one of the AGN regions described above (the optical lines are not shown).

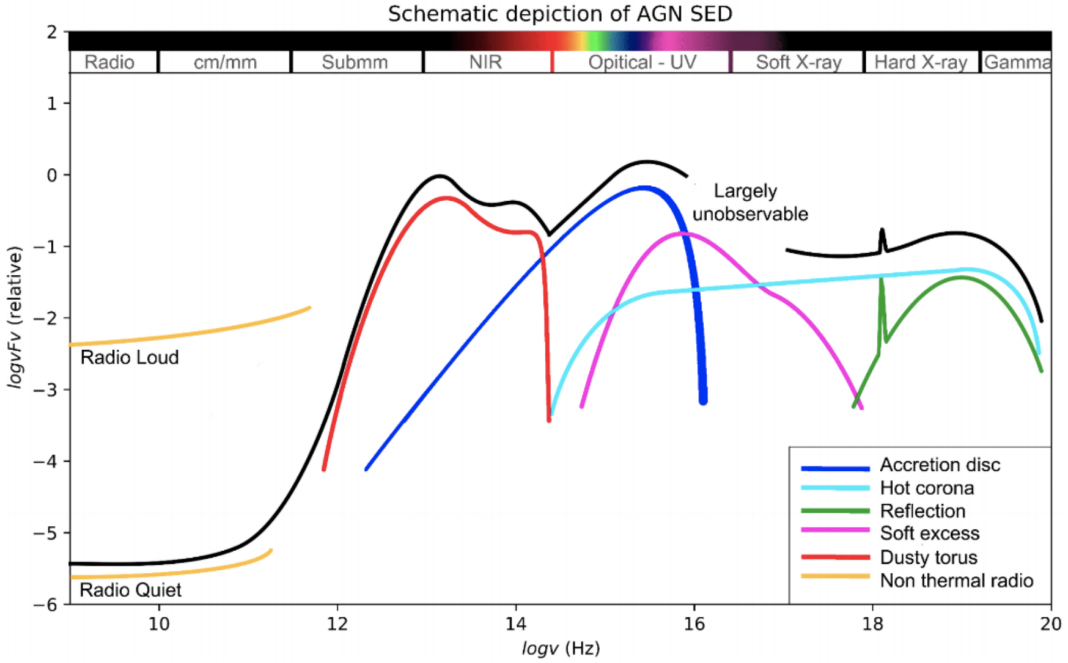

Figure 1.5: Spectral Energy Distribution (SED) of different AGN (credits: P. Monaco, https://adlibitum.oats.inaf.it/monaco/Lectures/notes_AGN_18_19.pdf) from radio to γ-rays. The solid black line represents the cumulative SED emission, while the various AGN components are reported with different colors, as shown in the bottom-right small panel.

Figure 1.6 is a zoom of the X-ray region. The primary power-law, the Compton hump and the iron line are shown.

In the soft part of the X-ray SED ($E \leq 1$ keV), the so-called “soft excess" is highlighted. Its origin is still debated (Done et al., 2012), with two possible explanations: it represents the extension at higher energies of the BBB emission or the extension at lower energies of the electrons' thermal populations in the hot corona. However, the soft excess temperature is found to not vary significantly with the SMBH mass, disfavoring the BBB possibility (Fabian and Miniutti, 2005). Another feature is present in the soft X-ray SED of many type 1 AGN, i.e, the “warm absorber": absorption lines observed below 2 keV and ascribed to photoionized gas ($T \approx 10^{4-5}K$), are often found to be outflowing at 100-1000 km s^{-1} (e.g., Reynolds and Fabian, 1995; Krolik and Kriss, 1995).

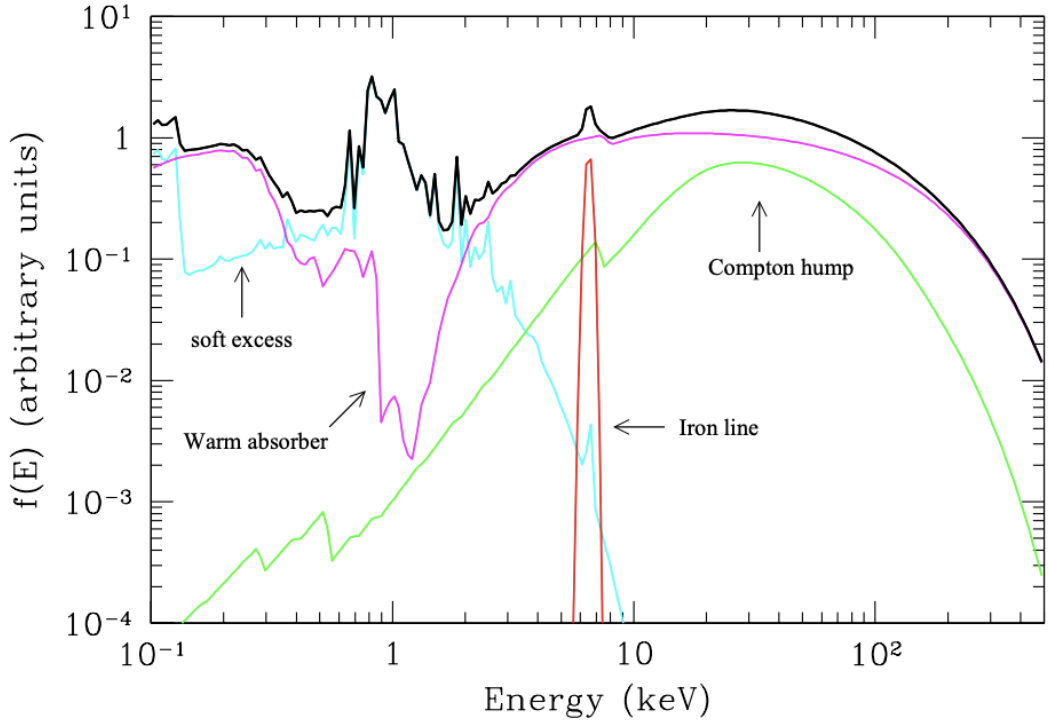

Figure 1.6: Average X-ray spectrum (black curve) with the main components highlighted with different colors for type 1 AGN. The purple line is the main power-law emission in this band. The spectrum is taken from Risaliti and Elvis (2004).

1.2 AGN unification

Since their discovery in the 1950s, AGNs have been observationally classified into many different types, depending on the particular wavelengths range used for the observations. Unification models for AGN (Barthel, 1989; Antonucci, 1993; Urry and Padovani, 1995) were developed later. In particular, in type 2 AGN the observer line of sights intercepts the dusty structure (torus). Only the emission lines from the NLRs are visible, as the torus hides the BLRs. In RL AGN, another source of anisotropy is the jet. Plasma moving at a velocity close to the speed of light suffers from relativistic effects, that can modify the apparent jet luminosity. The key parameter is the Doppler factor, defined as $\delta = [\gamma(1-\beta cos\theta)]^{-1}$, being $\beta = v/c$ the bulk velocity, $\gamma = \sqrt{1-\beta^2}$

the Lorentz factor and θ the angle between the jet and the line of sight. The Doppler factor relates intrinsic and observed luminosity (Urry and Padovani, 1995): $L_{obs} = \delta^p L_{intr}$, where p is a function of the spectral distribution of the electrons in the jet, L_{obs} is the observed luminosity and L_{intr} is the intrinsic luminosity. If θ is small ($< 10°$), the jet luminosity overwhelms the other emissions. In this case, AGN are classified as Blazars.

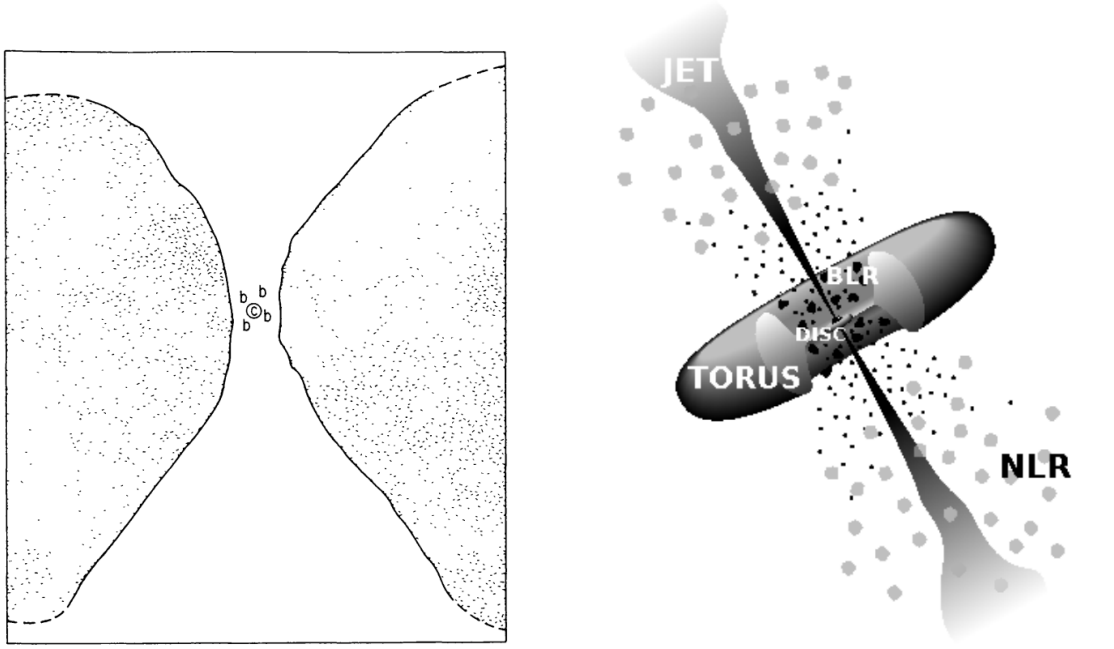

Figure 1.7: Two famous schemes for AGN unification. On the *let panel* a sketch from Antonucci (1993): the SMBH is at the center and is surrounded by the BLR, while the large toroidal structure can obscure the center along various (mostly “edge-on") lines of sight; in the *right panel*, the famous image from Urry and Padovani (1995) for radio-emitting AGN is reported, showing the accretion disc surrounding the SMBH, a dusty torus obscuring the BLR, the NLR and the first part of the jet emission.

The anisotropic nature of AGN (torus/jet) was insufficient to explain the properties of LINERs and other active nuclei that do not show signatures from torus and BLRs (Chiaberge et al., 2002; Netzer, 2015; Heckman and Best, 2014; Padovani et al., 2017). AGN can have different accretion regimes, implying that there is no one unique type of AGN seen at different orientations. In this direction, the Advection Dominated Accretion Flow (ADAF) disc, proposed by Narayan and Yi (1994), can explain the low-luminosity AGN emission. Such disc model consists of an optically thin, geometrically thick configuration, as explained below.

1.2.1 Inefficient engine

While in SSD, the gravitation power conversion into radiation is very efficient, in the ADAF solution, the viscous energy is stored in the gas as thermal energy (instead of being radiated) and advected onto the SMBH. The accreting material, having a low density, cannot cool efficiently, and

the cooling time becomes longer than the accretion time. Ions and electrons are thermally decoupled and very hot: $T_{ion} \approx 10^{12}/r$ K (where r is the Schwarschild radius, i.e., twice the gravitational radius) and $T_e \approx 10^{9-10}$ K. The accretion flow is radiatively inefficient ($< 1\%$ L_{Edd}), geometrically thick ($H/R \approx 1$, being H and R the disc height and radius, respectively), and optically thin. In Figure 1.8, the ADAF SED is reported, along with the main emission processes: synchrotron, bremsstrahlung, and Compton scattering.

The synchrotron emission is produced by relativistic thermal electrons. Its peak emission comes from the SMBH vicinity, while the radiation at lower frequencies is produced by the external part of the disc. The Compton scattering is produced by the interaction between hot electrons and low-frequency photons produced by synchrotron emission, up to 100 keV. If the accretion decreases, the Compton becomes less efficient and X-rays are dominated by bremsstrahlung emission, which cuts off at the electron temperatures. In Figure 1.8, three possible accretion rate configurations are highlighted: high accretion near the ADAF limit (dotted line), where the Compton scattering is dominant, intermediate accretion (dashed line), and, low accretion (solid line), where the Compton scattering component is less important, because of a lower optical depth ($\tau_e \propto \dot{m}$ Narayan et al. 1998a).

The γ–ray radiation is produced by the decay of neutral pions created in proton–proton collisions.

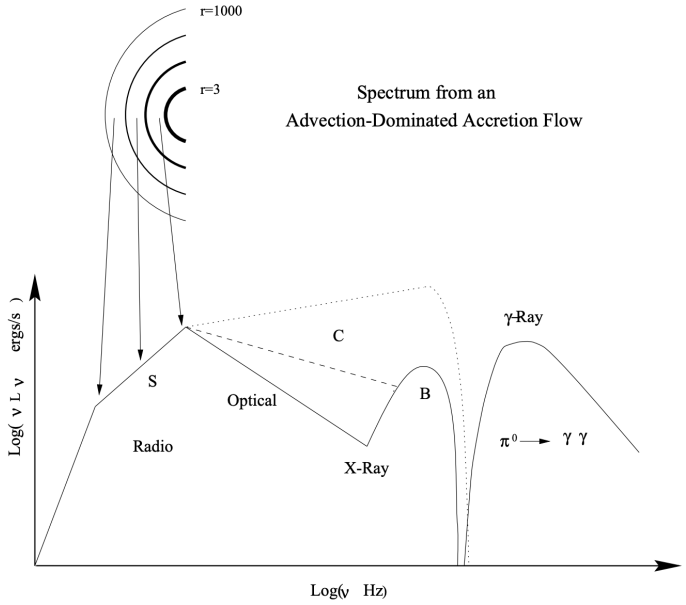

Figure 1.8: The ADAF schematic spectrum is reported (Narayan et al., 1998a). The component S refers to synchrotron emission, C to Compton scattering and B to bremsstrahlung. The solid line is the lowest admitted accretion rate value, the dashed line is an intermediate accretion, and the dotted one is for high accretion, near the critical ADAF value. γ–rays are due to the decay of neutral pions from proton-proton collisions.

Later, this basic model was further refined, and other accretion configurations were explored. For example, the ADIOS model can also reproduce hot, inefficient discs. In this case, the inward decrease of accretion is due to disc winds driving mass outward (Blandford and Begelman, 1999).

Chapter 2

Jetted AGN

AGN produce the most powerful, persistent jets in the universe. Many aspects of the jet nature are still debated, although the main ingredients necessary to launch a collimated, relativistic plasma are known. They consist in: (i) a gravitational body that is accreting material (SMBH with an accretion disc), (ii) a strong poloidal magnetic field, and (iii) a rotation of the central body (i.e., the SMBH spin), to create the so-called “magnetic tower". In this structure, the magnetic field lines twist helically along the axis of rotation. This magnetical structure envelops and drives the trapped plasma from the vicinity of the SMBH outwards, the jet can be launched (Meier et al. 2001, see Figure 2.1).

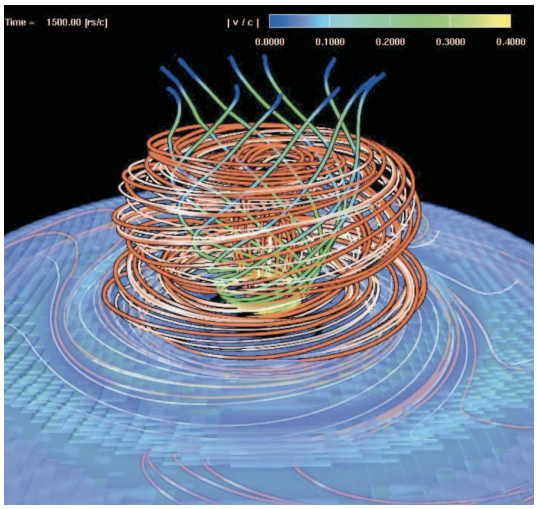

Figure 2.1: Simulation of the magnetic tower by Kato et al. (2004): the magnetic field lines dragged by the rotation of the SMBH and accretion disc are accumulated toward the poloidal plane, allowing the jet launching mechanism.

The energy needed to launch the jet can be extracted: (i) directly from the SMBH rotation (Blandford and Znajek, 1977, the BZ effect); (ii) from the accretion disc (Blandford and Payne, 1982, the BP effect), with field lines leaving it and extending to larger distances in the poloidal direction. In both cases, the magnetic tower power is built bringing together many weak field lines along this poloidal structure through matter accretion.

In the first case (BZ), the jet power is proportional to the square of its mass (M_{BH}), spin (J), and poloidal magnetic field (B_p) at its horizon[1] ($P_{jet} \propto (JM_{BH}B_p)^2$). In the second case (BP), the jet power depends both on the poloidal magnetic field and accretion disc configuration ($P_{jet} \propto B_p^2 R^3 \Omega$, where B_p is the poloidal magnetic field, R is the accretion disc radius and Ω is its angular velocity, see equation 4 of Meier 1999).
It should be stressed that a collimated jet is not the only possible outcome. Depending on the magnetic field strength, plasma density and BH/disc rotation, the launched material can have different structures: from a broad slow uncollimated wind to a strongly collimated relativistic jet.

After the jet launching, the plasma is accelerated and collimated along an extended region ($\gg$ 1 pc, Vlahakis and Königl 2004; Boccardi et al. 2021). Along this path, the magnetic energy is converted into kinetic energy of the plasma, which reaches relativistic velocities ($v \approx c$). Then, the magnetic field becomes negligible and the kinetic-flux dominated jet composed of relativistic particles continues its way outward up to hundreds kpc/Mpc scales. The jet can be described by dynamic gas laws: shocks (Blandford and Königl, 1979) and instabilities (Blake, 1972) can develop. The final part of the jet path is characterized by the loss of collimation and, thus, the loss of kinetic power in favor of radiation (dissipative phenomena) on scales $\geq$100 kpc (see Figure 2.2 for a scheme of the jet propagation by Boccardi et al. 2017). Compact hot-spots can be visible on very large scales (>100 kpc); in these cases, the dissipation is not efficient and the jet is still relativistic.

The non-thermal structures observed in a jetted AGN are:

- *the core:* it is a very compact region with a flat ($\alpha \sim 0$) spectrum in the radio band. Generally, it is an unresolved region, even at the Very Large Baselines Interferometer (VLBI) angular resolution ($<$ milli-arcsec);

- *the lobes:* they are the most extended structures. They are composed of plasma transported by the jet after shocking with the external medium and can be observed in the radio, X-ray and γ-ray bands. The low-frequency radiation is emitted by synchrotron, while the high energy photons are due to inverse Compton processes, where cosmic microwave background photons are up-scattered by lobes electrons (Kataoka and Stawarz, 2005; Migliori et al., 2007; Abdo et al., 2010; Ackermann et al., 2016);

- *the hot-spots:* they are very compact (usually point-like) and bright regions (observed from radio to X-rays) due to the impact of the jet with the external medium. Because of the high speed of the jet (supersonic), the jet structure is destroyed in the impact and shocks, able to re-accelerate the electrons, are produced. Hot-spots are observed not only in the radio band, but also at other frequencies, including X-rays (Wilson et al., 2001).

[1] It is defined as the radius at which the escape velocity is equal to the speed of light.

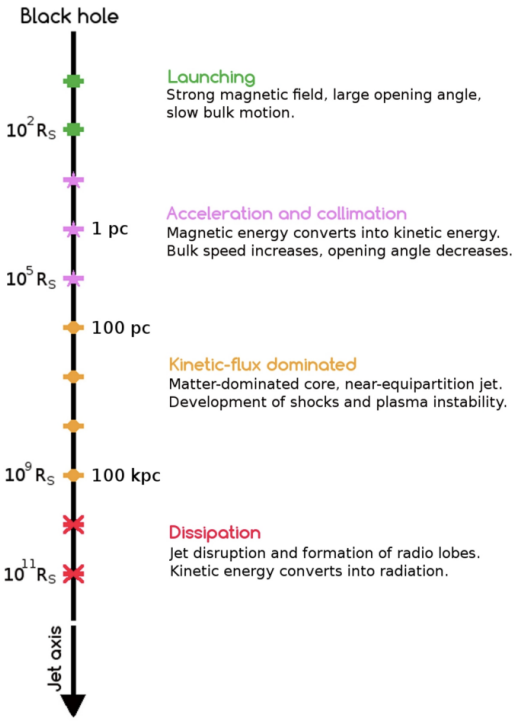

Figure 2.2: The jet path from the launching region in the SMBH vicinity up to the dissipative regions on kpc/Mpc scales. The distances are reported both in units of R_S (the Schwarzschild radius, i.e., twice the gravitational radius R_G) and in pc (valid for a SMBH with mass 10^9 $M_\odot$). Credit Boccardi et al. (2017).

All these structures can be observed in jetted AGN if the jet points away from the observer. If the jet axis is close to the line of sight, as discussed in section 2.1, relativistic effects strongly amplify the jet emission, making detecting any other AGN emission (except from the jet) challenging. Jetted AGN can be divided into blazars (jet-dominated) and Radio Galaxies (RGs), depending on the jet orientation. It is generally assumed that RGs have jet inclinations larger than 10 degrees.

2.1 Blazars

In blazars, the non–thermal jet radiation is amplified by relativistic effects (beaming), giving rise to flat radio spectra, large polarization and strong variability. It is possible to distinguish Blazars in BL Lacs and Flat Spectrum Radio Quasars (FSRQ, see, e.g. Kellermann et al., 1994). Generally, FSRQs show strong continuum emission and emission lines in the optical spectrum (see, e.g., Figure 1.3), signatures of an accretion disc which is efficient in accreting and radiating (SSD-like); conversely, BL Lacs lack strong emitting lines (due to their inefficient accretion disc, ADAF-like) and show a weaker continuum emission. In their SEDs, Blazars show the typical two-peaked emission (Fossati et al., 1998): the low-power peak is due to synchrotron emission (from radio to optical/UV wavelengths), while the high-energy one is produced by Compton mechanisms (SSC and IC from external photons, see Figure 2.3). Depending on the position of the two peaks, Blazars are divided into High Synchrotron Peaked (HSP), Intermediate Synchrotron Peaked (ISP) and Low

Synchrotron Peaked (LSP), with a synchrotron peak threshold at $\approx 10^{14-15}$ Hz.

The power of the source can change the position and intensity of the two peaks: the more the source is powerful (FSRQs), the more radiative field is present and the more IC phenomena (from both internal and external photons) can cool relativistic particles (the so-called "Compton dominance"). In the case of FSRQs, both the synchrotron and IC peaks are at “low" frequencies (IR band and soft γ-rays, respectively) and the higher frequency peak is found to dominate over the synchrotron one. Conversely, for sources characterized by lower intrinsic power and weaker radiation field (BL Lacs), the particle cooling from IC mechanism is less effective. Hence particles can be present at higher energies with lower cooling. Thus, both emissions peak at higher energies (up to soft X-rays for synchrotron and hard γ-rays for IC) and the Compton dominance is found to be small (Ghisellini et al., 1998). This is referred to as the “Blazar sequence" (see Figure 2.3).

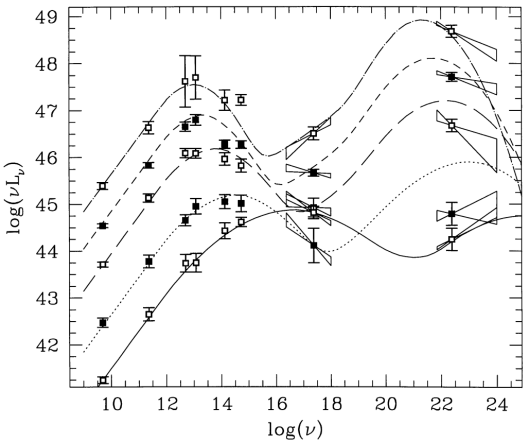

Figure 2.3: Blazar sequence from Fossati et al. (1998). At increasing power of the Blazar (i.e., increasing luminosity), both peaks move toward lower energies and the Compton domincance is more relevant (i.e., the ratio between the IC peak and the synchrotron peak). This is because the cooling mechanism through IC phenomena becomes more important in powerful Blazars with strong radiative field presence.

2.2 Radio galaxies

In the following Section, we will describe RGs in terms of radio and optical classifications and properties.

2.2.1 Radio classification

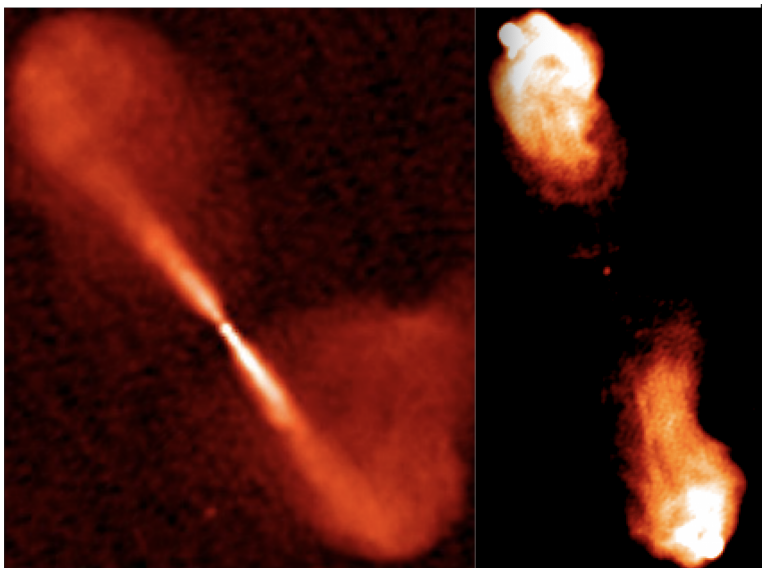

Figure 2.4: Radio luminosity emission at 21 cm observed with VLA of two famous RGs. On the *left*, 3C 296, a typical edge-darkened FRI where the bulk of emission is near the center (edge-darkened); on the *right*, Cygnus A, one of the most famous FRII RGs (edge-brightened), which shows bright hot-spots and lobes and weak emission near the source core. Credit NRAO.

The first classification, performed by Fanaroff and Riley (1974) in the radio band, followed morphological criteria. They introduced an R parameter defined as the ratio between the distance of the two radio emission peaks in both sides and the total dimension of the source. The sources with bulk of emission near the center ($R < 0.5$) are defined Fanaroff-Riley type 1 (hereafter FRIs), while the sources with radio emission peaks near to the extremities (i.e., $R > 0.5$) are FRIIs. For this reason, FRIs are also known as “edge-darkened", while FRIIs are named “edge-brightened" (see Figure 2.4 for an example of an FRI and an FRII). Fanaroff and Riley (1974) found that this morphological dichotomy reflected into a radio power dichotomy, with FRIs characterized, on average, by lower radio luminosities than FRIIs (with a threshold at $L_{150\ MHz} = 10^{26}$ W Hz^{-1}, Fanaroff and Riley, 1974; Tadhunter, 2016).

Over the years, the jet radio luminosity (L_{radio}) was found to be connected to the total jet power (P_{jet}); the more the jet is powerful, the more it is expected to radiate (see Willott et al. 1999; Godfrey and Shabala 2013). This was found to be true also comparing the jets’ radio luminosity with their mechanical luminosity, i.e., the work done by the jet in excavating the external medium (as estimated through X-ray cavities studies, see, e.g., Bîrzan et al. 2004, 2008; Cavagnolo et al. 2010).

Thus, the radio classification is both morphological and power-dependent.

2.2.2 Optical classification

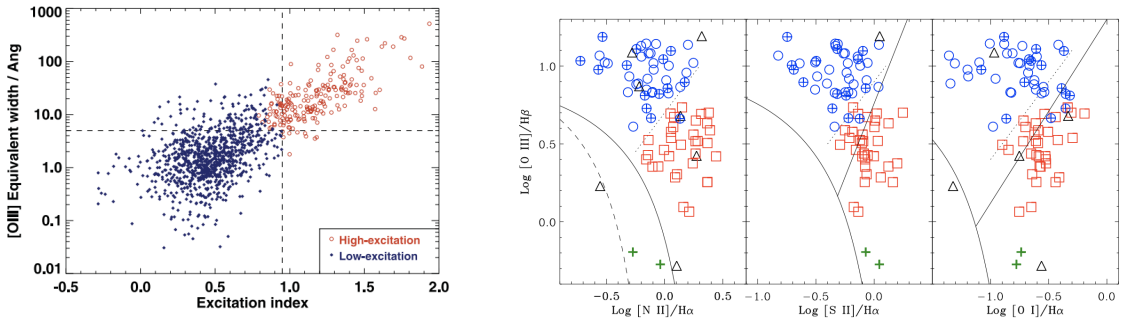

Figure 2.5: HERGs vs. LERGs classified by Buttiglione et al. (2010). *Left panel:* plot of EI (see Section 2.2.2) vs. [OIII] EW for LERGs (blue) and HERGs (red). The two quantities are well correlated, demonstrating that the distinction of HERGs from LERGs in terms of [OIII] EW and EI is reliable (credit Best and Heckman 2012). *right panel:* BPT diagrams showing the clear distinction between LERGs (red) and HERGs (blue), taking into account the excitation-line ratio.

As for RQ AGN, optical emission lines are helpful for RGs classification. In 1994, Laing et al. (1994) defined an optical classification based on the [OIII] and Hα narrow emission lines. Both come from the NLR and reflect the excitation level of the gas: the more photons are produced by the accretion disc, the more the NLR lines are excited. They proposed to split RGs into High Excitation Radio Galaxies (HERGs) and Low Excitation Radio Galaxies (LERGs): HERGs are characterized by $\frac{[OIII]}{H\alpha} > 0.2$ and [OIII] Equivalent Width (EW) >3 Å, while LERGs have low [OIII] luminosities and EWs. They are found to reside in different regions of BPT diagrams, with HERGs occupying the top-left region and LERGs the bottom-left, as shown in the right panel of Figure 2.5. For this reason, Buttiglione et al. (2009) defined an Excitation Index (EI) based on line ratios of six emission lines produced in the NLRs (H_α, H_β, [OIII], [NII], [SII], [OI])[2], able to distinguish between RGs with high-excitation level and low-excitation level of NLRs, depending on the radiative field produced by the central engine (see the left panel of Figure 2.5).

Then, Best and Heckman (2012) updated the optical HERG/LERG classification, adopting different criteria (Kewley et al., 2006; Buttiglione et al., 2009; Cid Fernandes et al., 2010), depending on the signal-to-noise ratio of the six cited lines.

Summarizing, the HERG/LERG classification reflects the accretion regime of the AGN central engine, since different excitation modes of the NLR are associated with different accretion rates (Gendre et al., 2013; Heckman and Best, 2014).

In particular, HERGs accrete efficiently ($L/L_{Edd} > 0.1$), i.e., the potential energy of the gas accreted by the SMBH is efficiently converted into radiation. Conversely, LERGs are characterized by low accretion rates, typical of radiatively inefficient hot accretion flows ($L/L_{Edd} \leq 0.01$-0.1), and the jet carries the bulk of the AGN energy output (Narayan et al., 1998b; Heckman and Best, 2014).

[2] $EI = log(\frac{[OIII]}{H_\beta}) - \frac{1}{3}\left[(\frac{[NII]}{H_\alpha}) + log(\frac{[SII]}{H_\alpha}) + log(\frac{[OI]}{H_\alpha})\right]$

2.2.3 Cross-classification: the general picture

As discussed in the previous two Sections, optical and radio classifications of RGs reflect different aspects of AGN emission: the optical classification reflects the AGN accretion rate (HERG/LERG), the radio classification characterizes the jet morphology and, consequently, its power (FRI/FRII).

Over the last years, observations showed that a link between accretion and ejection is present in RL AGN. In this direction, (i) Willott et al. (1999) found a positive correlation between the NLR luminosity and the extended radio luminosity for a sample of 211 FRII RGs belonging to the 3CRR and 7C catalogs at $z \leq 1.5$; (ii) Ghisellini and Celotti (2001) interpreted the FRI/FRII dichotomy from Ledlow and Owen (1996) diagram (galaxy r-band magnitude vs. radio power) as a difference in the central accreting process: the different jet morphology and power could correspond to a change in the accretion mode, with FRIIs being highly accreting RGs and FRIs being lowly accreting RGs; (iii) a similar result was found to be true also for Blazars: a linear correlation between accretion luminosity and jet power for 217 such objects was discovered by Ghisellini et al. (2014).

In particular, in such an accretion-ejection framework, the central engine activity is reflected in the radio band of RGs: inefficient engines (LERGs) are commonly associated with FRI morphologies and power (FRI-LERGs), while efficient engines (HERGs) are always (with only a few exceptions) found to be powerful FRIIs (FRII-HERGs).

FRI-LERGs and FRII-HERGs represent the two main categories of the local AGN population, depending on the central engine activity (Heckman and Best, 2014): FRI-LERGs are in a "jet-mode regime", i.e., ADAF-like engine (Narayan and Yi 1994, see Section 1.2.1), whose most energetic emission is represented by relativistic jets, thought to decelerate to transonic/subsonic velocities when interacting with the host galaxy; FRII-HERGs host a "radiative-mode engine", an efficient SSD-like disc (see Section 1.1.2, Shakura and Sunyaev 1973), able to produce powerful and collimated jets. Their features are summarized in Figure 2.6.

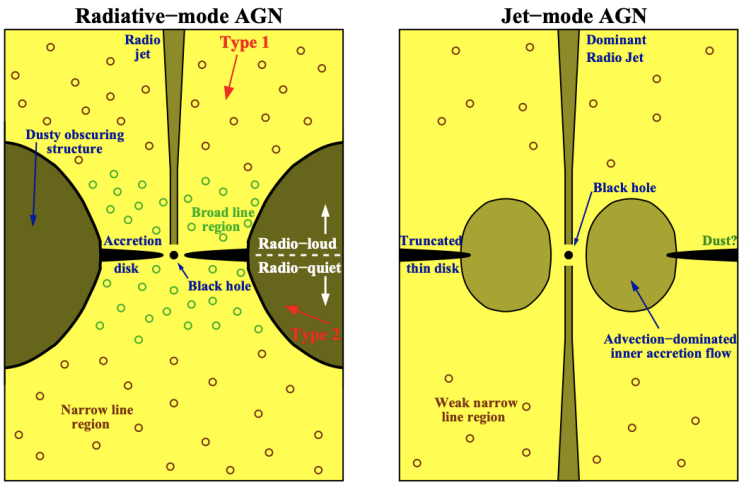

Figure 2.6: Schematic representation of the central engines of radiative-mode and jet-mode AGN as presented in Best and Heckman (2012). *Left panel:* the radiative-mode AGN is shown. The bulk of emission is represented by radiation, produced by an optically thick, geometrically thin accretion disc (SSD-like, i.e., HERGs). A powerful radio jet (FRII) is produced in a small percentage of cases. *Right panel:* the accretion is hot, geometrically thick and optically thin (ADAF-like, Narayan and Yi 1994, i.e., LERGs), even if at larger radii an outer geometrically thin disc can be present. These sources are usually found to produce radio jets (FRI-like), representing the bulk of their energetic output, while radiative emission is strongly reduced for the advection-dominated accreting structure.

2.3 Problems with the classical scheme of RGs

Since 1979, the classical scheme for which low-accreting RGs are associated to FRIs, while high-accreting RGs to FRII sources, was questioned (Hine and Longair, 1979):

> "The most striking result of the analysis of the radio morphological types is that class A radio galaxies [strong emission line spectra] are almost exclusively associated with powerful classical double sources, whereas class B galaxies [without strong emission lines] are associated with radio sources of all morphological types."

Tadhunter et al. (1998), analyzing the Southern sky with the 2Jy survey (Wall and Peacock, 1985), found a similar result: a population of RGs with NLR low-excitation signatures associated with powerful radio emission. Chiaberge et al. (2002) analyzed the optical spectra of 3CR RGs at $z < 0.3$ and similarly found that the optical nuclear properties of FRII sources can vary from source to source, suggesting that there is not a one-to-one correlation between the central engine and the jets morphology. They found that ≈ 20 % of FRIIs are LERGs. In 2010, when Buttiglione et al. defined a rigorous way to distinguish between 3CR LERGs and HERGs at $z < 0.3$ through diagnostic diagrams (see Section 2.2.2), the fraction of FRII-LERGs further increased (25%). This high percentage indicates that FRII-LERGs are not rare and exotic objects. As cross-population of RGs, FRII-LERGs break the classical scheme. Thus, they represent a key class to test the accretion-jet connection and the mechanisms involved in shaping different jet morphologies.

Chapter 3

The Jy regime

As discussed in the previous Section, FRII-LERGs do not fit into the classical accretion/ejection picture of RGs, since they show an inefficient engine associated with powerful jets. For this reason, they represent the most suited RGs class to explore the strongly debated shaping mechanism in RGs and its link with the AGN central engine.
We performed an X-ray spectral analysis of the RGs belonging to the 3CR sample at $z < 0.3$ with radio and optical classification available. FRII-LERGs represent the key targets of our study. Our goal is to investigate X-ray properties of such sources, since the X-ray band is a fundamental tool to explore the RGs central engine activity (as discussed in Section 1.1.2): (i) X-rays trace the AGN activity in the SMBH vicinity ($\leq$pc), enabling us to estimate the accretion rate on the smallest scales; (ii) they allow measuring the cold gas column density, i.e., to trace the possible AGN fuel availability on pc-kpc-scales. Throughout this work, the cosmological parameters adopted are: H_0=70 km s^1 Mpc^1, $\Lambda_\Omega = 0.73$, and $\Lambda_m = 0.27$ (in agreement with the *Planck 2015 Results*, see Planck Collaboration et al., 2016).

3.1 The analyzed sample

The Third Revised Cambridge Catalog (3CR, Bennett 1962) constitutes the most suited catalog for RGs, since it is the largest and most comprehensive catalog of radio sources to date, analyzed by almost all the ground-based and space facilities from radio to X-rays. Radio images are available from the VLA archives and surveys, optical counterparts (both spectra, photometry and images) were collected with different telescopes (Martel et al., 1999; Buttiglione et al., 2009) and also an X-ray survey with the Chandra satellite is available (Massaro et al., 2010, 2012).

Thanks to such a multi-wavelength dataset, 3CR sources at $z < 0.3$ are classified both in the optical (HERGs vs. LERGs) and radio bands (FRIs vs FRIIs). Following the accurate classification by Buttiglione et al. (2009), the RGs classified in both bands are 79. They can be distinguished as: 13 FRI-LERGs (hereafter only FRIs), 47 FRII-HERGs[1] and 19 FRII-LERGs. FRIIs are more frequently observed (66 out of 79) and span the entire redshift range. Conversely, FRIs are less common (13 out of 79) and at low redshift (z<0.05). FRIs are characterized by the lowest radio

[1] 17 out of 47 are Broad-Lines Radio Galaxies (BLRGs). They are, as well, classified as HERGs according to their NLR emission. The only difference of BLRGs with HERGs is the presence of broad permitted lines in the optical spectrum, coming from the BLRs. Hereafter, BLRGs are considered HERGs.

power on average ($L_{178\ \mathrm{MHz}}$ in erg s^{-1}, see Figure 3.1), while FRIIs span the same radio luminosity, independently of their optical classification (LERG/HERG).

Given the FRI low radio power, the limit in their maximum observed redshift ($z = 0.05$) could depend on the flux density limit of the survey (Jy-limited).

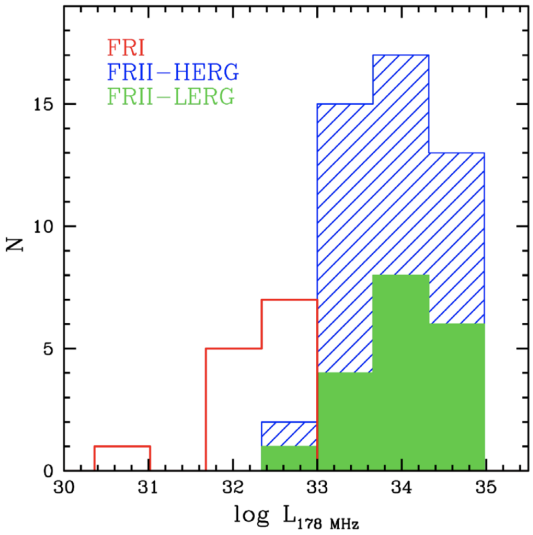

Figure 3.1: Radio luminosity distribution at 178 MHz in erg s^{-1} of the analyzed 3CR sample. FRIs are represented by the red line, FRII-HERGs are shown as the blue line containing oblique lines, FRII-LERGs are represented by the green area. The only difference observed is between FRIIs and FRIs (observed only at $z < 0.05$).

For the first time, FRII-LERGs are explored as a separate class. Their X-ray and multi-frequency properties are compared to those of FRII-HERGs, to understand their nature.

In particular, the goal of our analysis is to investigate the nuclear activity of sources down to the innermost regions (sub-pc/pc scales) both in terms of gas column density (N_{H}) and X-ray luminosity.

3.2 X-ray analysis and results

We performed a systematic X-ray analysis of all the FRIIs of the 3CR sample at z<0.3, exploiting archival data from the *Chandra* satellite. This is the most suited telescope to perform an X-ray analysis of RGs nucleus, given the good angular resolution ($\approx 0.5''$ in the observational energy band) and the presence of all the sources of the analyzed sample in the public archive [2].

We consider FRII-LERGs as key targets, i.e., the main sample. We also analyze X-ray data of FRII-HERGs as a control sample. FRI-LERGs (hereafter only FRIs) with X-ray information available from literature (Balmaverde et al., 2006) are considered for comparison with FRIIs.

For the FRII-LERGs with no *Chandra* detection, their presence in the XMM-*Newton* archive was checked. This is the case for 3C 349, 3C 353 and 3C 460, for which XMM-*Newton* data

[2] https://cda.harvard.edu/chaser/ .

were exploited. The energy range considered in the spectral fitting was 0.3-7 keV for *Chandra* and 0.5-10 keV for XMM-*Newton*. Using the PIMMS software for *Chandra* data and the task EPATPLOT in the SAS for *XMM-Newton* data, the presence of pile-up effects in each source has been checked. In most of the cases the pile-up was lacking or negligible ($< 10\%$) in FRII-LERGs, but it turned out to be relevant in BLO FRII-HERGs. Therefore, the *Chandra* spectral analysis has been performed only for the two BLOs for which the estimated pile-up was less than $< 10\%$: 3C 184.1 and 3C 459.

Chandra data were reprocessed using the software CIAO (Chandra Interactive Analysis of Observations), version 4.10 with calibration database CALDB version 4.8.1 and following standard procedures. When more than one observation was available, the data were combined to improve statistics. A preliminary check of the images was necessary to investigate the eventual presence of extended emission, possibly due to collisional gas emitting in the soft band. The analysis of the X-ray images showed that 6 out of 19 FRII-LERGs exhibit an extended emission. In contrast, none of the FRII-HERGs show large-scale extension in the *Chandra* images. In case the source was extended, two images were produced: a soft one (0.3-4 keV) and a hard one (4-7 keV). Subsequently, VLA radio contours at 1.4 GHz or 5 GHz (with a few arcsecs of spatial resolution) were superimposed on the hard X-ray image (4-7 keV) to correctly identify the peak of the nuclear emission. Given that all radio cores were found to be coincident with the X-ray peak, no astrometrical corrections were applied. The core spectrum was extracted from a circular region with a radius of $\approx 2''$ to collect more than 90% of photons. Instead, the background region was selected in a circular region in the same CCD of the source, avoiding any contamination from field sources or from the source itself.
To adopt the χ^2 statistics, spectra were grouped to a minimum of 20 counts per bin. If this was not possible, the C-statistics (Cash, 1979) has been applied, grouping the spectra to at least one count per bin. When the count number was less than 10, we only provided the flux and the luminosity of the sources, using the *Chandra* Proposal Planning Toolkit (PIMMS)[3] and assuming a simple power-law model with $\Gamma = 1.7$ (Grandi et al., 2006). This is the case for 3C 136.1, 3C 153 and 3C 430.

XMM-*Newton* data for FRII-LERGs have been reduced using the Scientific Analysis Software (SAS) version 16.1 with the latest calibration files and following standard procedures, exploiting the EPIC/pn data.
Source and background spectra have been extracted in 0.5-10 keV band from circular regions with radius varying between 20" and 30", depending on the extension of the source, to maximize the signal-to-noise ratio: at least 80% of photons fell within the extraction region. The background has been selected in a circular region in the same CCD as the source to avoid contamination from the source itself or the field sources.
Spectra have been grouped to a minimum of 20 counts per bin and the χ^2 statistics has been adopted.

The spectral analysis for both *Chandra* and XMM-*Newton* data has been carried out by using the XSPEC version 12.9.1 (Arnaud, 1996). The associated error has 90% confidence for one parameter of interest (Avni, 1976).

In the fitting procedure, at first, a single power-law convolved with Galactic column density (Kalberla et al. 2005; PHABS) was tested. If the power-law spectral slope was lower than 1, an intrinsic absorption component (ZPHABS) was added to the fit. In case of low statistics and/or

[3] `http://cxc.harvard.edu/toolkit/pimms.jsp`.

Table 3.1: Spectral parameters of the X-ray continuum.

Name	z	$N_{H,Gal}$ (10^{20} cm^{-2})	Fitted Model[a]	$N_{H,intr}$ (10^{22} cm^{-2})	Γ_H	$L_{2-10\ keV}$ (10^{42} erg s^{-1})	Statistics[b]
FRII-LERGs							
3C 88	0.0302	8.3	[iii]	2.0 ± 0.5	1.6 ± 0.3	0.4 ± 0.2	36.9/50
3C 132	0.214	21.3	[ii]	5^{+4}_{-3}	$1.7^{\dagger}$	22^{+12}_{-8}	4.1/5 C
3C 153*	0.2769	16.2	[i]	-	$1.7^{\dagger}$	< 1.5	-
3C 165	0.2957	19.4	[ii]	3 ± 2	$1.7^{\dagger}$	23^{+11}_{-8}	8.2/14 C
3C 166	0.2449	17.1	[i]	< 0.16	1.6 ± 0.2	80 ± 10	20.1/19
3C 173.1	0.292	4.5	[vi]	30^{+200}_{-20}	$1.7^{\dagger}$	27^{+180}_{-16}	35.3/25 C
3C 196.1	0.198	6.0	[vii]	-	-	< 9.6	20.5/13 C
3C 213.1	0.1939	2.4	[i]	< 0.43	$1.9^{+0.5}_{-0.4}$	4 ± 1	15.4/9 C
3C 236	0.1005	1.0	[ii]	$1.9^{+0.6}_{-0.5}$	1.4 ± 0.3	12^{+7}_{-4}	27.0/29
3C 288	0.246	0.8	[vii]	-	-	< 4.7	6.4/6
3C 310	0.0535	3.7	[vii]	-	-	< 0.02	10.5/17 C
3C 326	0.0895	9.0	[ii]	$2.2^{+2.8}_{-1.7}$	$1.7^{\dagger}$	$0.2^{+0.2}_{-0.1}$	3.4/3 C
3C 349	0.205	1.9	[ii]	0.9 ± 0.2	1.4 ± 0.2	60 ± 10	46.2/47
3C 353	0.0304	9.3	[vi]	$6.7^{+0.9}_{-0.8}$	1.7 ± 0.2	3 ± 1	58.0/61
3C 357	0.1662	3.1	[iii]	3 ± 2	2 ± 1	22^{+6}_{-12}	17/18 C
3C 388	0.0917	5.5	[vii]	-	-	< 0.9	62.5/59 C
3C 401	0.2011	5.9	[i]	< 0.16	1.7 ± 0.1	5.0 ± 0.5	15.9/18
3C 430*	0.0541	33.1	[i]	-	$1.7^{\dagger}$	< 0.05	-
3C 460	0.268	4.72	[iii]	25^{+23}_{-11}	$1.7^{\dagger}$	20 ± 10	5.7/6
FRII-HERGs/BLRGs							
3C 20	0.174	18.0	[ii]	15^{+4}_{-3}	$1.7^{\dagger}$	110^{+30}_{-20}	24.1/25 C
3C 33	0.0596	3.4	[v]	53^{+8}_{-7}	$1.7^{\dagger}$	100^{+30}_{-20}	32.5/40
3C 61.1	0.184	7.9	[iii]	29^{+23}_{-12}	$1.7^{\dagger}$	40^{+40}_{-20}	30/18 C
3C 79	0.2559	8.7	[iii]	33^{+12}_{-10}	$1.7^{\dagger}$	270^{+130}_{-90}	14.4/16 C
3C 98	0.0304	10.0	[iv]	$9.4^{+1.0}_{-0.9}$	$1.7^{\dagger}$	$5.3^{+0.5}_{-0.3}$	57.4/48
3C 105	0.089	12.0	[iv]	43^{+7}_{-6}	$1.7^{\dagger}$	220^{+90}_{-50}	13.6/12
3C 133	0.2775	25.0	[ii]	$0.8^{+0.4}_{-0.3}$	2.0 ± 0.3	190^{+80}_{-50}	39.4/26
3C 135	0.1253	8.7	[vi]	34^{+32}_{-19}	$1.7^{\dagger}$	14^{+23}_{-8}	15.8/13 C
3C 136.1*	0.064	32.0	[i]	-	$1.7^{\dagger}$	< 0.06	-
3C 171	0.2384	5.7	[ii]	7 ± 1	1.5 ± 0.3	130^{+80}_{-50}	33.8/26
3C 180	0.22	14.0	[iii]	70^{+160}_{-50}	$1.7^{\dagger}$	90^{+1800}_{-70}	7.1/7 C
3C 184.1	0.1182	3.2	[iii]	8 ± 1	$1.7^{\dagger}$	110 ± 10	19.8/24
3C 192	0.0598	3.9	[iii]	34^{+8}_{-7}	1.7 ± 0.5	2^{+4}_{-1}	14.3/18
3C 223	0.1368	1.0	[iii]	13^{+13}_{-7}	$1.7^{\dagger}$	20^{+16}_{-8}	10/10 C
3C 223.1	0.107	1.3	[ii]	28 ± 6	$1.7^{\dagger}$	90^{+30}_{-20}	9.3/12 C
3C 234	0.1848	1.8	[vi]	17^{+9}_{-6}	$1.7^{\dagger}$	150^{+70}_{-50}	6.6/8
3C 277.3	0.0857	0.9	[xiii]	27^{+6}_{-5}	$1.7^{\dagger}$	9^{+2}_{-1}	23.1/21
3C 284	0.2394	0.9	[i]	< 0.91	2.3 ± 1.0	$1.1^{+0.4}_{-0.5}$	1.4/5 C
3C 285	0.0794	1.3	[vi]	38^{+8}_{-6}	$1.7^{\dagger}$	35^{+10}_{-7}	7.7/11
3C 300	0.27	2.5	[i]	< 0.19	1.4 ± 0.3	13 ± 2	12.7/10 C
3C 303.1	0.267	3.0	[ii]	18^{+132}_{-16}	$1.7^{\dagger}$	15^{+400}_{-11}	0.1/2 C
3C 305	0.0416	1.3	[viii]	< 0.72	$1.7^{\dagger}$	0.04 ± 0.01	36.3/24 C
3C 321	0.096	3.8	[ix]	26^{+20}_{-13}	$1.7^{\dagger}$	4^{+4}_{-2}	61.2/40 C
3C 327	0.1041	5.9	[x]	30^{+63}_{-18}	$1.7^{\dagger}$	8^{+31}_{-4}	46.6/25
3C 379.1	0.256	5.4	[vi]	60^{+70}_{-30}	$1.7^{\dagger}$	110^{+400}_{-70}	7.3/8 C
3C 381	0.1605	9.9	[iii]	30^{+7}_{-6}	$1.7^{\dagger}$	240^{+70}_{-50}	18.9/21 C
3C 403	0.059	12.1	[xi]	46 ± 3	$1.7^{\dagger}$	78^{+10}_{-9}	51.5/57
3C 436	0.2145	6.7	[iii]	48^{+22}_{-15}	$1.7^{\dagger}$	100^{+80}_{-40}	14.4/15 C
3C 452	0.0811	9.8	[v]	53^{+8}_{-7}	$1.7^{\dagger}$	100 ± 20	77.9/78
3C 456	0.233	3.7	[ii]	7 ± 1	$1.7^{\dagger}$	160 ± 20	63.6/59 C
3C 458	0.289	5.9	[ii]	35^{+20}_{-16}	$1.7^{\dagger}$	150^{+140}_{-70}	16.8/14 C
3C 459	0.2199	5.2	[xii]	4^{+3}_{-2}	$1.7^{\dagger}$	12^{+3}_{-2}	31.2/25

[a] – All the adopted models are absorbed by the Galactic column density:[i] po;[ii] zpha*po;[iii] zphabs*po+po; [iv] zphabs*(po+zgauss)
[v] zphabs*(po+zgauss)+po+pexrav); [vi] zphabs*(po+zgauss)+po;[vii] mekal;[viii] mekal+po;[ix] zphabs*(po+zgauss)+po+2zgauss;
[x] zphabs*(po+zgauss)+po+ mekal;[xi] zphabs*(po +zgauss)+po+2zgauss+mekal; [xii] zphabs*(po)+po+mekal; [xiii] zphabs*(po+zgauss)+zphabs*po
[b] – Statistics refers to the entire energy band assuming the model listed in column (4). "C" indicates that the C-statistics was adopted.
* – luminosities estimated with PIMMS assuming a simple power law model with $\Gamma = 1.7$.
† – fixed photon index

complexity of the emission, the hard photon index was frozen ($\Gamma = 1.7$): this was necessary for 7 out of 19 FRII-LERGs and 27 out of 32 FRII-HERGs. In these case, we further checked if a variation of the photon index (Γ), could induce significant changes in the column density estimate: the column densities and the intrinsic luminosity remain consistent within the errors even considering different photon indices ($\Gamma = 1.4$ and $\Gamma = 2.0$): for all the sources with fixed spectral slope, the N_H and L_X values do not change respectively more than $\approx$15% and 40% varying the power law spectral slope from 1.4 to 2.0. As the uncertainties on these quantities are up to 70%, we are confident that the $\Gamma = 1.7$ assumption does not significantly affect our results. A Gaussian component (ZGAUSS) was also included in the hard spectrum if positive residuals were noticed in the region of the iron Kα line (5-7 keV). Once the iron line was detected, the presence of a reflection component in the hard-X-rays (Compton hump, see Section 1.1.1) was checked using the PEXRAV model. Such reflection component is produced by the same region emitting the Fe Kα line, as a consequence of the primary X-ray emission reprocessing (Lightman and White, 1988). In this case, the cut-off energy was frozen to 100 keV, while the angle between the normal to the disc and the observer was fixed to 30°. We detected Fe Kα lines for 2 FRII-LERGs and 12 FRII-HERGs, while the reflection components are detected only in 2 FRII-HERGs.

A second power-law, or a thermal emission (MEKAL), was added to the fit when residuals were still present at soft energies. Thermal emission is observed when the source is surrounded by a gaseous environment, i.e., the typical hot gas revealed in early-type galaxies (T$\approx$ 1 keV, Fabbiano et al., 1992) or ICM (IntraCluster Medium, if the source is in a cluster). If other soft lines are still present, the possible presence of photoionized gas was investigated. In two FRII-HERGs, i.e. 3C 403 and 3C 321, single soft X-ray emission lines (Gaussian profile) associated with Ne IX, O VII and Mg XI were revealed in the spectrum.

The X-ray analysis results are reported in Tables 3.1 and 3.2.

The photon index (Γ) was constrained in 8 out of 19 FRII-LERGs: the average value is 1.7 with a standard deviation of 0.3. About 50% of the sources required intrinsic cold gas obscuration, with a moderate absorption ($N_{\rm H}$) of the order of a few 10^{22} cm^{-2}. Only in two RGs, i.e. 3C 173.1 and 3C 460, the column density reaches values of few 10^{23} cm^{-2}. If present, the soft X-ray excess is well described by a power-law, that is probably scattered nuclear emission: the scattered component normalization values at 1 keV are always a few percent of the absorbed one (the average value is 6%, in agreement with those measured for type 2 Seyferts: e.g., Bianchi and Guainazzi 2007).

The cluster emission, when present in the X-ray images, generally overwhelms the core emission, preventing any study of the nucleus, as in the cases of 3C 196.1, 3C 288, 3C 310 and 3C 388. For these sources, the calculated 2-10 keV luminosity is considered an upper limit of the nuclear AGN emission. Only in 3C 88 and 3C 401 the AGN spectrum was disentangled from its thermal emission.

FRII-HERGs have, generally, more complex spectra than FRII-LERGs: in 90% of cases they are obscured, with $N_{\rm H}$ values typically higher than FRII-LERGs ($N_{\rm H} \sim 10^{23}$ cm^{-2}). Given that $N_{\rm H}$ and Γ are two correlated parameters, the photon index (Γ) could be well constrained in only 5 out of 32 of cases ($<\Gamma>= 1.8$ and $\sigma_{rms} = 0.5$). Strong iron lines are detected in 12 sources, and for two sources also, a Compton reflection model was required.

Table 3.2: Reprocessed Features.

Name	FeK_α line[(a)]	Reflection (R)
FRII-LERGs		
3C88	unconstrained	-
3C132	EW<949	-
3C165	EW<776	-
3C166	EW<388	-
3C173.1	EW≥ 886	-
3C213.1	unconstrained	-
3C236	EW<572	-
3C326	unconstrained	-
3C349	EW<339	-
3C353	EW$=100\pm78$	-
3C357	EW<610	-
3C401	unconstrained	-
3C460	EW<359	-
FRII-HERGs/BLRGs		
3C20	EW<281	-
3C33	EW$=139\pm89$	R$=1.5^{+0.4}_{-0.6}$
3C61.1	EW<359	-
3C79	EW<157	-
3C98	EW$=277\pm135$	-
3C105	EW$=178\pm132$	-
3C133	EW<453	-
3C135	EW$=916^{+1474}_{-719}$	-
3C171	EW<117	-
3C180	EW<744	-
3C184.1	EW<278	-
3C192	EW<260	-
3C223	EW<836	-
3C223.1	EW<374	-
3C234	EW$=900\pm400$	-
3C277.3	EW$=200\pm100$	-
3C284	unconstrained	-
3C285	EW$=367^{+144}_{-47}$	-
3C300	unconstrained	-
3C303.1	unconstrained	-
3C305	unconstrained	-
3C321	EW$=988^{+751}_{-474}$	-
3C327	EW$=2000^{+3000}_{-742}$	-
3C379.1	EW$=557^{+1900}_{-464}$	-
3C381	EW<2304	-
3C403	EW$=153^{+60}_{-15}$	-
3C436	EW<591	-
3C452	EW$=172^{+65}_{-65}$	R$=2^{+0.4}_{-0.5}$
3C456	EW<156	-
3C458	EW<238	-
3C459	EW<649	-

[(a)] – Observed iron line equivalent width in eV.

For most FRII-HERGs (>50%), the soft X-ray contribution is well reproduced by a power-law, which could represent the scattered component of the primary one: its average unabsorbed normalization at 1 keV is 8% of the absorbed power-law. Only in a few cases, a MEKAL model is required in addition to a second power-law. This emission could represent either collisional gas emission or mimic photoionized features (Balmaverde et al., 2012).

3.3 FRII-LERGs: evolved HERGs or a different class of RGs?

The unabsorbed X-ray luminosity ($L_{2-10\ keV}$) can be exploited to trace the nuclear activity. If it is normalized by the Eddington luminosity, $L_{2-10\ keV}$ is a direct proxy of the accretion rate ($L_{2-10\ keV}/L_{Eddington}$, Merloni et al. 2003). Note that for RGs with an ADAF-like engine, the estimated X-ray luminosity could provide an upper limit of the accretion luminosity, as there could be a significant contribution from the jet emission. To obtain the Eddington luminosity, the BH masses were calculated through the relation between the H-band host-galaxy magnitude (taken from Buttiglione et al. 2009) and M_{BH}, provided by Marconi and Hunt (2003) (with a dispersion of ~ 0.3 dex in the BH mass).

The $L_{2-10\ keV}/L_{Eddington}$ histogram is presented in the right panel of Figure 3.2. To test if two samples are drawn from the same parent population, a two-sample test univariate program, which takes into account also upper limits (TWOST, Feigelson and Nelson 1985; Isobe et al. 1986), is exploited. FRIs are clearly separated from FRII-HERGs with a probability $P_{TWOST} > 99.99\%$. FRII-LERGs are in between. They are separated from FRII-HERGs with a probability $P_{TWOST} = 99.99\%$. Instead, the probability that FRII-LERGs are distinguishable from FRIs, sharing similar LERG engines, is $P_{TWOST} = 99.42\%$. The same trend is observed when the ionizing luminosity (L_{ion}) normalized by the Eddington luminosity, is considered (see the left panel of Figure 3.2). This quantity is defined as $\log L_{ion} = \log L_{[OIII]} + 2.83$ (Buttiglione et al., 2009). L_{ion} is defined in a similar way to the already discussed L_{bol} definition by Heckman et al. (2004), they differ only for the multiplicative factor. L_{ion} is directly related to the accretion-driven radial efficiency (as L_{bol}), being responsible for the excitation of the NLR gas. FRII-LERGs have intermediate properties between the low-accreting FRIs and the high-accreting FRII-HERGs, in terms of accretion and column density (see Table 3.1).

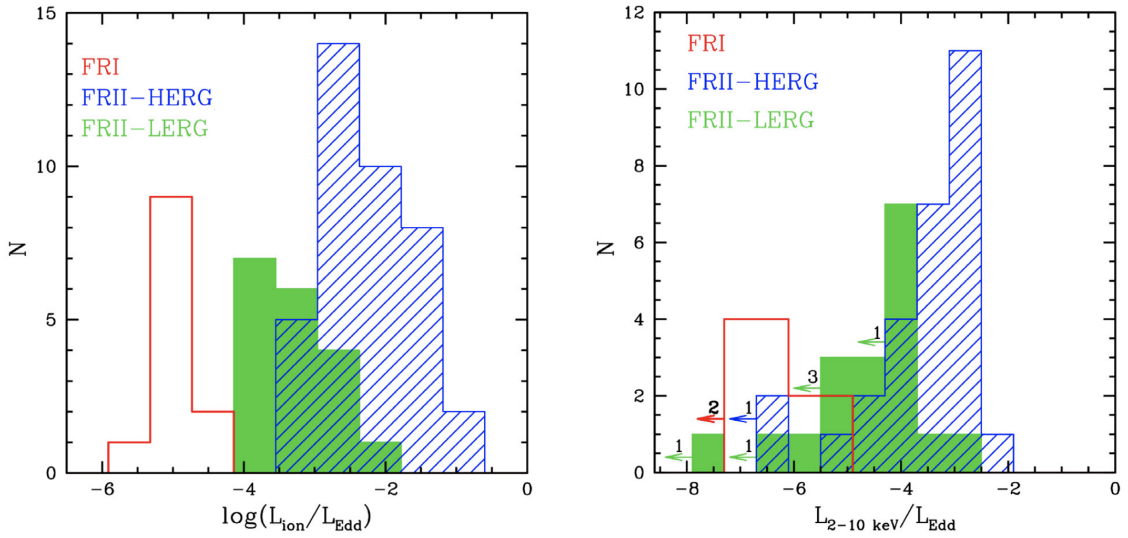

Figure 3.2: Accretion rates proxies for the 3CR sample. FRIs are in red, FRII-HERGs are in blue and FRII-LERGs are in green. In both histograms, the three populations clearly occupy distinct regions, with FRII-LERGs characterized by intermediate values between the low-accreting FRIs and the high-accreting FRII-HERGs. *Left panel:* the accretion rate is estimated through the [OIII] line luminosity. L_{ion} is defined by Buttiglione et al. (2009) as: $\log L_{ion} = \log L_{[OIII]} + 2.83$; *right panel:* accretion rate proxy as estimated from the X-ray analysis ($L_{2-10\ keV}/L_{Eddington}$). Upper limits are reported as arrows of the specific color for each population.

A first hypothesis to explain this intermediate behavior is that FRII-LERGs represent an evolutionary stage of HERGs, i.e, a possible recent change in the central activity occurred (see also Tadhunter 2016 for a recent discussion). In this case, FRII-LERGs could have recently changed their accretion mode because, for example, they have exhausted the cold material fueling the central engine. However, on lobes-scales, there is no difference in radio power between FRII-LERGs and FRII-HERGs. Therefore, it is reasonable to think that this information may not have reached radio structures yet, which are formed at kpc/Mpc distances from the central engine. In this case, a disconnection between the central engine activity and jet power is expected, as it is found in the FRII-LERG population: their large-scale radio structures are the heritage of a past AGN activity at higher efficiency.

Another possibility is that FRII-LERGs, while not as powerful accretors as FRII-HERGs, can still form typical FRII-like structures if embedded in a favorable environment. In fact, the environment is often invoked in literature as a fundamental ingredient for shaping different jets' power. For example, Gendre et al. (2013), analyzing the Mpc-environment for a large sample of radio galaxies, suggests that the connection between the central engine accretion mode and the jet power/morphology is not one-to-one, while the environment plays a crucial role. In particular, they defined a parameter to measure the Mpc-scale environment for each RG, following Wing and Blanton (2011): the cluster richness (hereafter CR). The CR parameter accounts for the number of galaxy companions identified in the optical bands within 1 Mpc around each target: CR$<$30 indicates a poor environment, while CR$>$30 is a rich one. They found that FRI sources lie in higher-density environments, on average, than FRII sources. For our 3CR sample, it is

possible to exploit the Gendre et al. (2013) CR measurement to characterize the Mpc-scale environment of RGs. In particular, it is possible to explore the relation between accretion, in terms of $L_{2-10\ keV}/L_{Edd}$, radio morphology and environment for 35 sources: 18 FRII-HERGs, 8 FRIs, and 9 FRII-LERGs (see Figure 3.3). As suggested by Gendre et al. (2013), it is possible to roughly distinguish between rich and poor environments by selecting a threshold at $CR = 30$. In this way, the situation becomes clear: FRII-HERGs occupy the poorest environments and are characterized by the largest accretion rates, FRIs are segregated to rich clusters and show the lowest accretion rates, FRII-LERGs occupy an intermediate region straddling the threshold between rich and poor environments and being characterized by intermediate accretion rates.

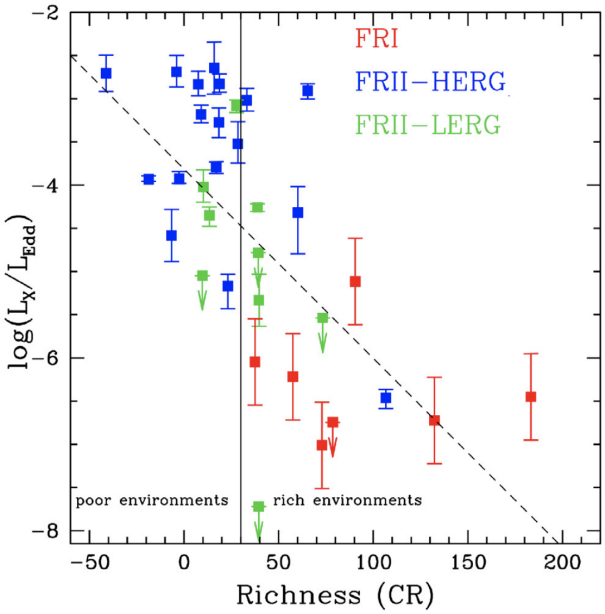

Figure 3.3: Cluster richness (CR) vs. accretion rate proxy as estimated through the 2-10 keV luminosity. FRIs are in red, FRII-HERGs are in blue, and FRII-LERGs are in green. The solid vertical black line represents the threshold between poor and rich environments ($CR = 30$) as defined by Gendre et al. (2013). The oblique dashed black line is the linear regression of all the datasets, including upper limits ($P_{Kendall-\tau} > 99.9\%$). FRII-HERGs are clustered in the top left part of the plot, i.e., they are found to reside in poor environments and to possess high accretion rates, FRIs are in rich clusters and show the lowest accretion rates values, FRII-LERGs show intermediate values between the two: they have intermediate accretion rate and are straddling the threshold bewteen poor and rich environments.

Considering all the RG populations, a clear anti-correlation between the accretion rate proxy and the CR is found: the Kendall$-\tau$ test (performed exploiting the ASURV software including upper limits through the parametric EM algorithm) provides a high probability that these quantities are correlated ($P_{Kendall-\tau} > 99.9\%$). This result suggests a strong impact of the large-scale environment on the central engine accretion regime. It agrees with environmental HERG/LERG studies in the local universe. For example, Hardcastle et al. (2007) suggests that accretion of the hot phase of the intergalactic medium is sufficient to power low-excitation radio sources (LERGs), while high-excitation sources (HERGs) are powered by accretion of cold gas that is, in general,

unrelated to the hot IGM (InterGalactic Medium). O'Sullivan et al. (2015) stated that HERGs are mainly found in poor environments, while LERGs are in a wider environmental range (from poor to rich ones). They also differ in their host galaxies' properties, with LERGs mainly hosted by massive elliptical galaxies with hot X-ray halos fuelling the central engine (Bondi-like accretion), while HERGs are characterized by ongoing star formation and abundance of cold gas availability, able to fuel the central engine with high efficiency (SSD-like). Thus, in addition to the evolutionary scenario (FRII-LERGs are starved HERGs), a possible role played by the environment in shaping RGs strongly emerges from these results and will be further investigated in the next Sections.

Chapter 4

The mJy regime

4.1 The mJy sample

The FIRST (e.g., Faint Images of the Radio Sky at Twenty-cm; Becker et al., 1995) and NVSS (National Radio Astronomy Observatory (NRAO) VLA Sky Survey; Condon et al., 1998) surveys at 1.4 GHz constituted two fundamental improvements. The main difference between the two surveys is the angular resolution due to a different array configuration of the interferometer. The NVSS survey covers the entire northern hemisphere with declination greater than -40° with an angular resolution of 45 arcsecs. It is sensitive to the radio diffuse emission but cannot resolve the different structures composing a discrete source. Its limiting point source flux density is $\approx$ 2.5 mJy at 5σ. The FIRST survey has complementary characteristics: the longer baselines of the VLA array configuration guarantee a much better angular resolution of $\approx$5 arcsecs. In this case, the disadvantage is the low sensitivity in tracing the diffuse emission. Extended sources are often resolved in multiple discrete components. Its coverage area is designed to largely overlap the optical Sloan Digital Sky Survey (hereafter SDSS), reaching a limiting point source flux density of $\approx$1 mJy at 5σ. Given the similar sky coverage and the complementarity of NVSS and FIRST surveys, they can be combined for identifying radio sources' different properties.

The SDSS dataset is the most important optical survey for galaxies data availability. It maps one-quarter of the entire sky, determining the positions, the photometry and the optical spectra from IR up to blue frequencies of hundreds of millions of celestial objects, with more than a few million galaxies and AGN.

Best et al. (2005) cross-matched the SDSS survey (DR2) with the radio surveys (NVSS and FIRST), producing a large sample of radio-emitting sources associated with optical galaxies.

Later, a larger sample of radio-emitting sources (18286 in total) in the local universe ($0.01 < z < 0.7$) was collected by Best and Heckman (2012) exploiting the SDSS DR7.

For the optical classification, Best and Heckman (2012) defined a protocol to classify RGs in LERG/HERG through six emission lines (H_α, H_β, [OIII], [NII], [SII], [OI]). If all the six lines are detected, they calculated the EI following Buttiglione et al. 2009 (see Section 2.2.2). If one or more lines are missing, they exploited other efficient methods: they used one of the Kewley et al. (2006) diagnostic diagrams when at least four out of six lines were detected; if only [OIII],[NII] and H_α lines were detected, the diagnostic diagrams by Cid Fernandes et al. (2010) were adopted; otherwise, they exploited the cited Laing et al. (1994) definition of HERGs based on the [OIII]

line EW.

They defined a subsample of local ($0.01 < z < 0.3$) galaxies as the "main galaxy sample"[1]. RL AGN were distinguished from starburst galaxies (also emitting in the radio bands) following a combination of different observables: (i) calcium break (D_n4000, an index exploited to measure the star-formation in galaxies) vs. ratio of radio luminosity to stellar mass, (ii) Hα vs. radio luminosity, (iii) standard BPT diagrams (see the A1 appendix of Best and Heckman, 2012, for details). The final number of RL AGN was 7302 Following the classification protocol described in Section 2.2.2, 6070 were classified as LERGs and 216 as HERGs. An optical classification was impossible for 14% of the objects. RGs with no optical classification are probably LERGs. This is suggested by Figure 4.1, where L[OIII] is plotted as a function of DN. LERGs and unclassified AGN occupy the same region of the plot. However, to have a conservative approach and not to include eventual biases in the results, the unclassified sources are excluded from all the analysis.

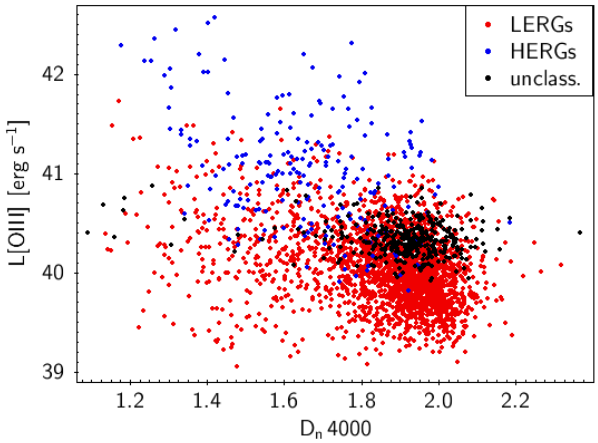

Figure 4.1: Calcium break (D_n4000) vs. [OIII] line luminosity (in erg s^{-1}) in the Best and Heckman (2012) sample: LERGs (red points), HERGs (blue points) and RGs with no optical classification available (black points) are reported. The unclassified sources follow the same trend as LERGs.)

We observed the opposite in the 3CR sample in the same redshift range, where HERGs are more numerous than LERGs. Going down from Jy to mJy, the RGs population changes. LERGs become dominant in the mJy sky, while HERGs drop in percentage.

4.1.1 Data availability

The sources are part of SDSS DR7 and, thus, plenty of information is available. Taking advantage of the MPA-JHU DR7 release of spectrum measurements[2], fundamental quantities for each galaxy can be found: the SMBH mass calculated through the stellar velocity dispersion (σ_*, the relation is: $log(M/M\odot) = 8.32 + 5.64 \times log(\sigma_*/200\ km\ s^{-1})$, taken from McConnell and Ma, 2013, which have a sample of both late-type and early-type nearby galaxies), the stellar calcium

[1] They performed an r-band magnitude restriction ($14.5 < r < 17.77$) to eliminate stellar contamination without removing genuine galaxies.

[2] https://wwwmpa.mpa-garching.mpg.de/SDSS/DR7/

break (D_n4000), and, the [OIII] line luminosity, a powerful tracer of AGN efficient/inefficient accreting activity. Since all sources are also part of the NVSS survey, we can uniformly measure each RL AGN radio luminosity at 1.4 GHz. This sample allows exploring the fainter AGN in the local universe, expanding the Jy limited knowledge to mJy RL AGN.

Capetti et al. (2017b,a) provided the radio classification of a BH12 subsample at $z < 0.15$. They visually inspected all the FIRST images available for each source to define its radio morphology properly. Only sources whose radio emission reaches distances > 30 kpc from the center are classified as FRIs or FRIIs. They found 216 FRIs in the FRICAT and 122 FRIIs forming the FRIICAT. Combining the BH12 sample and the FRCAT catalogs, we could explore more than 300 mJy RGs with solid optical and radio classification (see Figure 4.2). All FRIs are found to be LERGs, while 89 % of FRIIs are LERGs. Therefore, in the mJy sky, the FRII-LERG presence reaches its maximum, an impressive jump from the Jy catalogs: the percentage of FRIIs being LERGs is 27 % for the 3CR sample; if we consider the same FRCAT redshift range ($z < 0.15$), the 3CR FRII-LERGs percentage is even lower (i.e., 23 %).

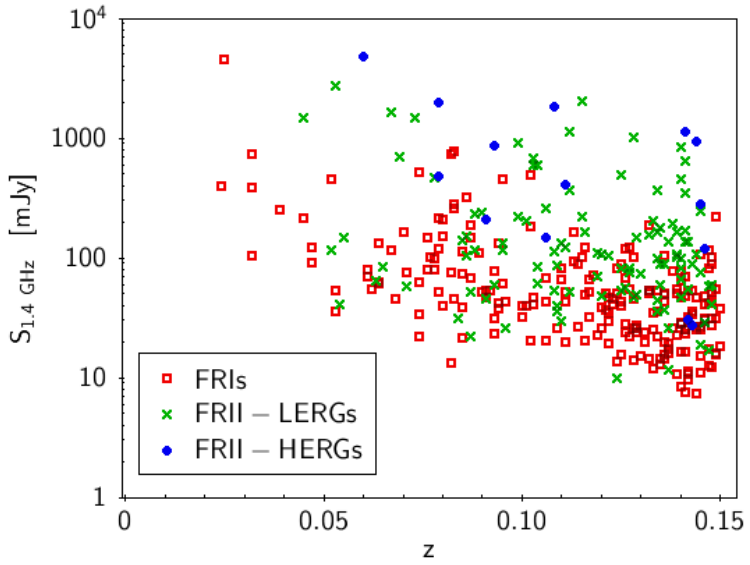

Figure 4.2: The BH12-FRCAT sample: redshift distribution vs. 1.4 GHz flux density from NVSS. FRIs are reported as empty red squares, FRII-LERGs are the green crosses and FRII-HERGs are shown as blue-filled circles.

Later, another RGs class was added to the FRCAT samples with a minimum flux density of 5 mJy at 1.4 GHz: the FR0s (Baldi et al., 2018). The 108 FR0s in the FR0CAT catalog are compact RGs with a radio size $\leq$5 kpc at $z < 0.05$ (i.e., where the cosmological scale is 1 "$\approx$1 kpc). They are all classified as LERGs (except for four FR0-HERGs, which are not included in the FR0CAT). FR0s are hosted in massive early-type galaxies, as it is also found for FRIs. In the very local universe ($z < 0.05$), they represent the dominant RGs population. In the same z-range where 108 FR0s are found, there are 21 FRIs and just one FRII, exploiting the FRCAT catalogs. Their high fraction rules out the hypothesis for which FR0s are young RGs that will be extended in the future. Among other possibilities, their compact nature can be explained if they are able to launch slow

jets only. Jets with lower bulk speed can be strongly affected by entrainment and instabilities, being disrupted within the InterStellar Medium (ISM). The cause of such jets would be a lower SMBH spin value than in FRIs/FRIIs.

4.1.2 Exploring the BH12-FRCAT sample

The study of mJy sample produced interesting results. One of the most impressive concerns the "famous " Ledlow-Owen diagram (Ledlow and Owen, 1996). It was interpreted as a fundamental result in the direction of the accretion-ejection connection. FRIs and FRIIs clearly occupy different regions of the diagram as a consequence of different accreting engines (see the left panel of Figure 4.3): low-accreting sources (LERG-like) produce low-power FRI morphologies, while high-accreting AGN (HERG-like) form powerful FRIIs (Ghisellini and Celotti, 2001). In the mJy sky, this clear FRI-FRII dichotomy is lost. FRIIs are no more found only in the top-left part of the plot (i.e., at a high accretion rate, see the right panel of Figure 4.3). The original one-to-one association (HERG-FRII and LERG-FRI) is no more present: as already discussed in the previous Section, in the mJy sky the majority of FRIIs are associated to a LERG engine, undermining the Jy FRI-FRII dichotomy.

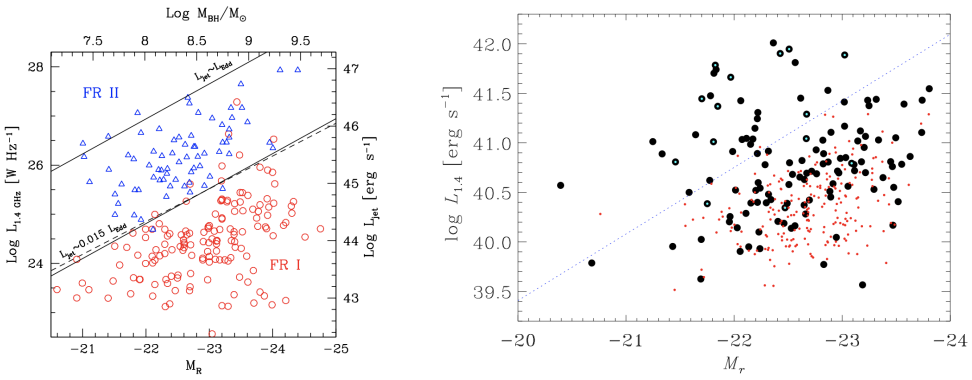

Figure 4.3: Left panel: Ledlow and Owen (1996) original diagram of the Abell sample observed with VLA, revised by Ghisellini and Celotti (2001) accounting for different accretion rates. The galactic R-band optical absolute magnitude is compared to the AGN radio power at 1.4 GHz in (W Hz^{-1}); right panel: the same plot as reported for the FRCAT by Capetti et al. (2017a). FRI-LERGs are in red and FRII-LERGs are in black (cyan centered for FRII-HERGs). The dotted line represents the separation between FRIs and FRIIs reported by Ledlow and Owen (1996), converted to the SDSS magnitude definition. FRI-LERGs are found to reside below their original threshold found in the Jy regime. Conversely, FRII-LERGs fall in both regions of the diagram.

In a recent paper, Grandi et al. (2021) performed a statistical analysis of the main observables for the FRCAT sources to compare the average properties of the three classes: FRII-HERGs, FRII-LERGs and FRIs.

Table 4.1: FRCAT Average Properties

Class	**median**	**average**	**std**	**N. objects**
($z < 0.15$)		Log ($L_{1.4GHz}$) (erg s^{-1})		
FRI	40.32	40.34	0.34	219
FRII-LERG	40.77	40.75	0.49	108
FRII-HERG	41.37	41.26	0.55	14
		Log(L_{OIII}) (erg s^{-1})		
FRI	39.87	39.86	0.23	107
FRII-LERG	39.91	39.95	0.39	66
FRII-HERG	41.42	41.30	0.52	14
		Velocity Dispersion σ_* (km s^{-1})		
FRI	254	256	35	218
FRII-LERG	246	243	39	102
FRII-HERG	209	204	23	
		Stellar Mass Log(M_*) ($M_\odot$)		
FRI	11.38	11.38	0.19	214
FRII-LERG	11.33	11.33	0.31	107
FRII-HERG	11.09	11.08	0.25	14
		Calcium break (D_n4000)		
FRI	1.96	1.94	0.12	218
FRII-LERG	1.96	1.94	0.14	108
FRII-HERG	1.59	1.53	0.19	14
		Log(BH) ($M_\odot$)		
FRI	8.91	8.91	0.39	218
FRII-LERG	8.83	8.77	0.41	102
FRII-HERG	8.43	8.36	0.28	12
		Log(L_{rad}/L_{Edd})		
FRI	-4.03	-4.03	0.40	106
FRII-LERG	-3.85	-3.74	0.55	62
FRII-HERG	-1.84	-2.1	0.57	12

The main observables for each population are reported in Table 4.1: the median, average, and relative standard deviation of all the studied properties. A comparison among the different classes was performed by applying a KS test. We conservatively assumed that two data sets are different if the KS probability is less than 10^{-3} (i.e. if the two datasets are drawn from a different distribution with a confidence level of 3σ). The KS results are reported in Table 4.2.

Table 4.2: FRCAT KS test results

Classes	**KS probability (%)**					
$z < 0.15$	Log($L_{1.4GHz}$)	$Log(L_{OIII})$	Log(BH)	Log(L_{rad}/L_{Edd})	Log(M_*)	D_n4000
FRI vs FRII-LERG	> 99.9	82	99.63	99.65	94.3	94
FRI vs FRII-HERG	> 99.9	> 99.9	> 99.9	> 99.9	> 99.9	> 99.9
FRII-LERG vs FRII-HERG	98.1	> 99.9	> 99.9	> 99.9	99.68	> 99.9

As expected, FRII-HERGs and FRIs are distinct populations from any point of view. FRII-HERGs have smaller black holes, larger radiative power (expressed in terms of L_{rad}/L_{Edd} [3]), and

[3] where L_{rad} is calculated from the [OIII] line luminosity following Heckman et al. (2004): $L_{rad} = 3500 \times L_{[OIII]}$

more stellar activity. They are younger systems. More interesting is that our analysis shows that FRII-HERGs and FRII-LERGs are also different. FRIIs with an inefficient engine have more massive black holes and a more evolved stellar population (see Figure 4.4), i.e., are more similar to FRIs. Indeed, FRI and FRII-LERG classes are almost completely overlapped in the histograms of Figure 4.4. The nuclear properties of mJy LERG sources, independently of their radio morphology are very similar.

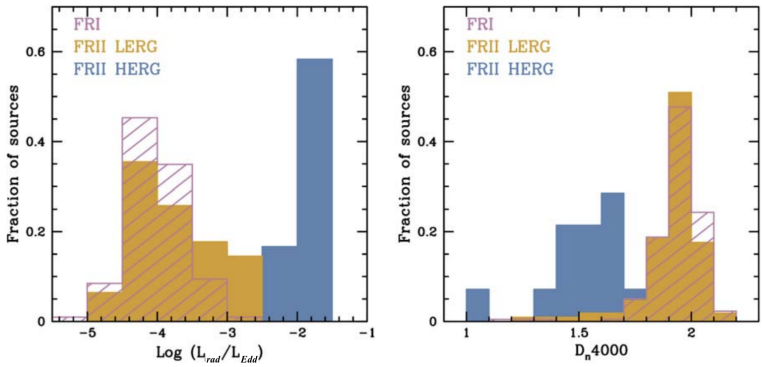

Figure 4.4: FRCAT histograms from Grandi et al. 2021. FRIs are in pink with oblique lines, FRII-LERGs are in solid yellow, FRII-HERGs are in solid blue. Left panel: $L_{rad}./L_{Edd}$; right panel: calcium break (D_n4000)

Different possibilities were explored to interpret the FRII-LERGs nature. The first possibility, proposed after the 3CR sample analysis (Macconi et al. 2020, Section 3), is that FRII-LERGs are evolved HERGs which are recently switched to an inefficient LERG-like engine for the fuel consumption, while their lobes emission is a signature of the past stronger activity.

Another option is that FRII-LERGs constitute a separate class of objects, not affected by evolution. In this case, a similar LERGs engine (left panel of Figure 4.4) would be able to produce outflowing plasma with different accelerations. This radio power spread would depend on different properties in the SMBH vicinity. The two most accreditated jet launching mechanisms are BP and BZ effects (Section 2). The first one (BP, Blandford and Payne 1982) is linked to the accretion disc, which is dragging the magnetic field lines thanks to the accretion rate; the second one (BZ, Blandford and Znajek 1977) extracts the energy for the jet power from intrinsic SMBH properties, such as its magnetic field (B) and spin (J). Different intrinsic configurations could be able to justify the wide range of radio power and different morphologies associated to a similar central engine.

Another option (already proposed in the Jy 3CR analysis, Macconi et al. 2020, Section 3) is that the environment is able to influence the jet power and morphology (the extrinsic paradigm): a jet interacting with an external medium could suffer from instabilities and matter entrainment. The interaction with a hostile environment would reduce the jet power and collimation, giving rise to edge-darkened morphologies. In this direction, FRIs are commonly found in richer environments, which could be responsible for their jet disruption on kpc scales and, consequently, the absence of distant hot-spots. Conversely, FRIIs, even with an FRI-like accretion, can keep the jet collimated and relativistic up to the hotspot region, if they inhabit poorer environments (Gendre et al., 2013; Ineson et al., 2015; Miraghaei and Best, 2017; Croston et al., 2019). Then, it is now fundamental

to study and characterize the large-scale environment of RGs in the local universe to understand its role and weight on RGs populations.

Chapter 5

The Mpc-scale environment role

To study the RGs Mpc-scale environment, we exploited the paper of Wen and Han 2015 (hereafter WH15), reporting the identification of 158103 clusters of galaxies in the SDSS (DR 12) observations at $0.05 < z < 0.75$.

They followed an iterative method (Friend-of-Friend algorithm[1]) to determine each cluster and the galaxies that constitute it. The Brightest Cluster Galaxy (BCG) was selected as the center for each cluster. The cluster radius (r_{500}) was defined as the radius at which the cluster reaches 500 times the critical density of the universe. For each cluster, they calculated the cluster richness: $R_{L*,500} = L_{500}/L* \; E(z)^{1.4}$; it is defined as the ratio between the total r-band luminosity within r_{500} and the characteristic Schechter luminosity of a galaxy in the r-band ($L*(z) = L*(z=0)10^{0.4Qz}$, with $Q = 1.16$ for a purely passive evolution (Blanton et al. 2003; Wen and Han 2015). $E(z) = \sqrt{\Lambda_\Omega + \Lambda_m \, (1+z)^3}$ is a correction factor that depends on the redshift and is significant only for clusters lying at $z > 0.45$. The catalog is more than 95 % complete for SDSS clusters with masses $> 1 \times 10^{14} \, M_\odot$ at $z < 0.42$ [2].

5.1 Matching

We matched the BH12 main sample (i.e., a subsample where stellar contamination was eliminated without removing genuine galaxies, see Section 4.1) of RL-AGN with the WH15 clusters using the following criteria:

1. separation between BH12 and WH15 positions (RA and DEC) to be less than each WH15 cluster radius (r_{500});

2. a separation in spectroscopic redshift to be less than the dispersion velocity for each cluster, calculated through the virial theorem ($\sigma = \sqrt{\frac{GM_{500}}{3R_{500}}}$, where $\sigma = \Delta z c$, M_{500} is calculated from

[1] It is a tool used to identify groups of objects in a simulation: it is demanded that any object that "finds" another one within a certain distance (i.e., the so-called linking length) is linked to the first object in forming a group. The second object (i.e., the friend of the first one) is also linked to all the other objects within the linking length from the first object (all the friends-of-friends), creating a network of objects (clusters in this case).

[2] They use Monte Carlo simulations to test the completeness of the sample. Mock clusters are simulated with assumptions for their distributions and added to the real SDSS data. The Friend-of-Friend algorithm is applied to such combined data to find the percentage of detected mock clusters. The detection rate of mock clusters is considered to indicate completeness.

the cluster richness ($R_{L*,500}$) by WH15);

3. a cut in redshift @ 0.05<z<0.3, to overlap the WH15 catalog and the BH12 main sample.

Considering only the associations with clusters having spectroscopic redshifts (89% of the WH15 sample, 31987 in this z-range), the number of RGs in dense environments turns out to be 2179 out of 7219 RGs.

There are cluster-galaxy associations that we consider uncertain. They concern: (i) RGs associated with clusters for the cluster photometric redshift, following the WH15 method ($\Delta z_p = 0.04 \times (1+z_p)$); (ii) RGs associated with a cluster within 3σ, following the same procedure explained in the matching criteria (i.e., position and redshift). We obtained 565 RGs with an uncertain association. The remaining 4475 RGs out of 7219 can be considered isolated sources.

For such sample, the stellar mass for each host-galaxy ($M_*/M_\odot$) and its specific star formation rate (sSFR, i.e., SFR/M_*) are available from the GALEX-SDSS-WISE LEGACY M2 CATALOG (Salim et al., 2016, 2018) for 3268 out of 7219 sources (45 %). In general, tracing the galactic sSFR is essential since it measures the current stellar activity and, thus, it is a proxy of the available galactic fuel to trigger both star formation and the central AGN. As it is found in various works (both observations and simulations), the most active AGN in the local universe (showing the highest AGN luminosities) are hosted in the most star-forming, gas-rich galaxies (see, e.g., Terrazas et al., 2017; Thomas et al., 2019; Piotrowska et al., 2022; Ward et al., 2022).

5.2 HERGs vs. LERGs

Table 5.1: HERGs/LERGs in clusters and in isolated environments

Class	N TOT	IN	% IN	OUT	% OUT	unc association	% unc association
LERGs	5994	1829	30	3687	62	478	8
HERGs	209	14	7	188	90	7	3
opt unclass	1016	336	33	600	59	80	8

The HERG/LERG percentages inside and outside clusters are summarized in Table 5.1. A larger percentage of AGN are found outside the cluster. More impressive, isolated LERGs are more numerous than those in galaxy-rich environments. This result is at odds with the generally accepted idea that LERGs are preferentially found in clusters. HERGs avoid rich environments.

Although they are few, there are however HERGs that are in clusters. We then checked if there is a richness ($R_{L*,500}$) difference between clusters hosting AGN with different optical classifications.

The median $R_{L*,500}$ value for LERGs is 23 and 17 for HERGs, while the average values are 29 and 21, respectively. Only 4 out of 14 HERGs ($\approx 30\%$) are in rich clusters ($R_{L*,500} > 20$ as defined by WH15, see Figure 5.1), while 1113 out of 1829 LERGs are found in rich clusters (i.e., 61%). No HERGs above $R_{L*,500} = 60$ are found. However, performing a KS test to understand if the two samples are drawn from the same distribution, we find only a 2σ probability (96.6%) that they come from a different distribution.

The 1016 RGs with no optical classification available follow a similar trend as LERGs: 336 are in clusters (33 %), 600 are isolated (59 %) and 80 have an uncertain association (8 %).

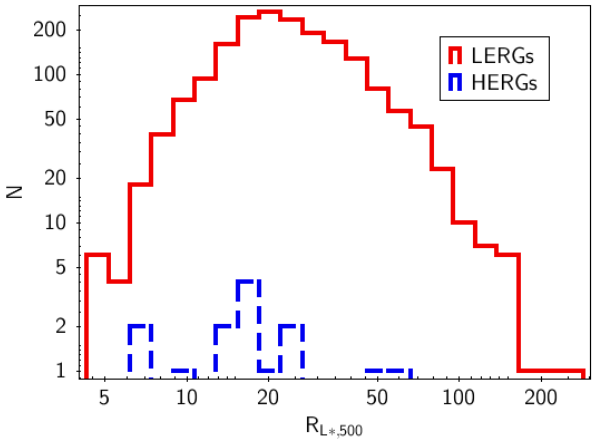

Figure 5.1: HERGs (blue dashed line) vs. LERGs (red solid line) distributions in terms of cluster richness, as defined by WH15: the sum of r-band luminosities of galaxy companions within the cluster radius normalized by the evolved characteristic (z-dependent) luminosity of galaxies in the r band. HERGs are found in poorer clusters than LERGs on average.

In summary, we confirm the HERG's preference for low-density regions, as already pointed out by many other authors (e.g., Gendre et al., 2013), but disagree with the current idea that LERGs are mainly in clusters.

Considering general analysis on host galaxy populations in the local universe (z<1), there are many studies in the literature showing differences inside vs. outside clusters: in rich Mpc-scale environments, the majority of galaxies are quiescent with lower cold gas availability and SFR rates than isolated galaxies (see e.g., Dressler, 1980; Butcher and Oemler, 1984; Moore et al., 1996; Gómez et al., 2003; Poggianti et al., 2006; Cooper et al., 2008; Guglielmo et al., 2019). In such dense environments, the galactic gas consumption should have occurred at z>1 [3], reducing the number of currently available fuel in local cluster galaxies (Balogh et al., 2004). The same is true for radio-active AGN found in clusters: more distant galaxy clusters (1<z<1.5) are more likely to host high-luminosity radio sources; conversely, the fraction of radio-active clusters drop by a factor 100 at z<0.3 (see e.g., Moravec et al., 2020; Mo et al., 2020).

The difference in galaxy populations distribution inside and outside clusters could explain the lack of HERGs in rich environments: efficiently accreting HERG engines are always found to be hosted in galaxies with high SFR rates and strong stellar activity (see, e.g. Best and Heckman, 2012; Miraghaei and Best, 2017). This is in agreement with previous works: HERGs are mainly found in poorer environments and hosted in galaxies with ongoing star-formation activity, while LERGs are found in any environment and are hosted by massive elliptical galaxies, characterized by hot-accretion and with a minimal cold gas supply (Best, 2004; Hardcastle, 2004; Gendre et al., 2013; Heckman and Best, 2014; O'Sullivan et al., 2015).

Now we focus on the isolated sample of RGs, where the large-scale environment cannot influence RGs.

[3] Two different kinds of mechanisms are possible: those that lower the gas content, and therefore the potential star formation rate in galaxies, and those that precipitate bursts of star formation (Hashimoto et al., 1998).

5.3 Outside the cluster: LERGs vs. HERGs

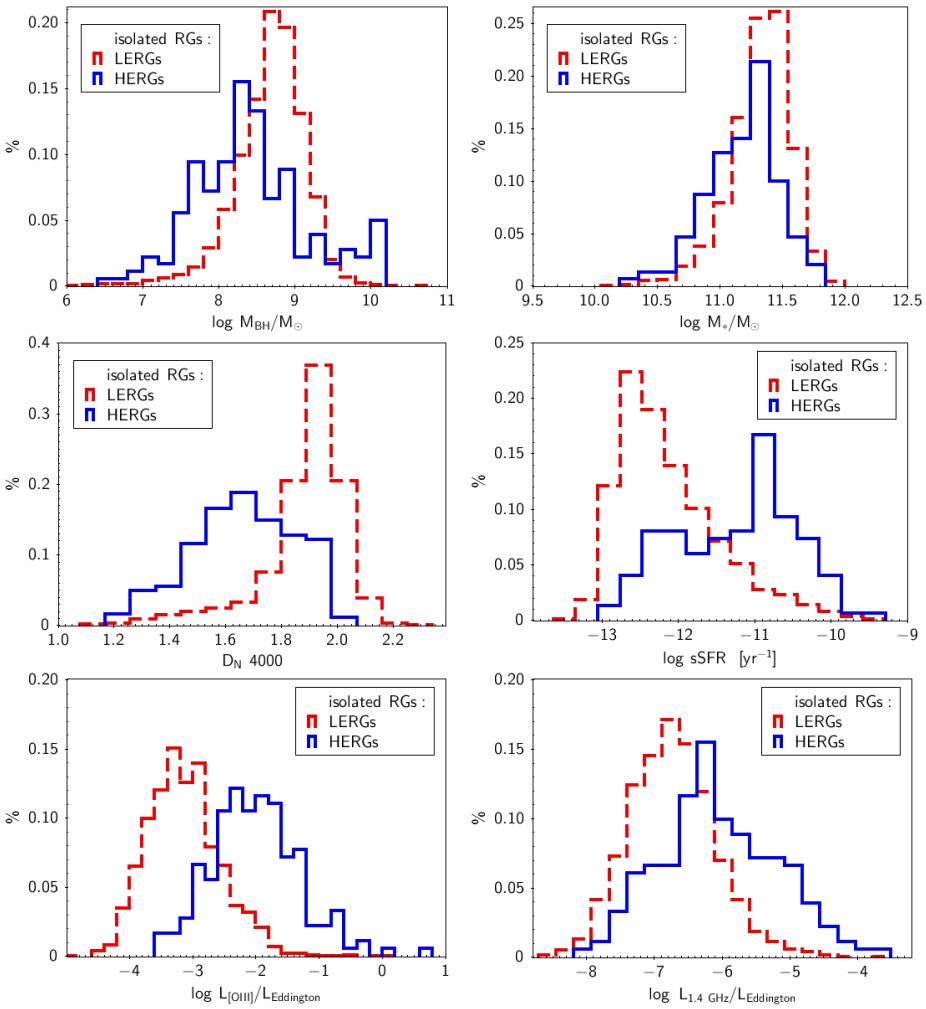

Figure 5.2: Distributions of isolated RGs: LERGs (red dashed lines) vs. HERGs (blue solid lines).

This section explores the nuclear and galactic properties of isolated LERGs and HERGs.

The median values and KS tests for each explored quantity are reported in Table 5.2. The most significant histograms are shown in Figures 5.2.

isolated RGs: LERGs vs. HERGs

M_{BH}	M_*	D_n4000	sSFR	$L_{[OIII]}/L_{Eddington}$	$L_{1.4\ GHz}/L_{Eddington}$
$M_\odot$	$M_\odot$		yr^{-1}		
isolated LERGs: 3589					
Median values					
5.3×10^8	2.3×10^{11}	1.92	5.3×10^{-13}	2.0×10^{-7}	1.8×10^{-7}
isolated HERGs: 181					
Median values					
2.4×10^8	1.7×10^{11}	1.66	8.9×10^{-12}	2.8×10^{-6}	7.2×10^{-7}
KS test probability:					
> 99.99 %	> 99.99 %	> 99.99 %	> 99.99 %	> 99.99 %	> 99.99 %

Table 5.2: Complete comparison between LERGs and HERGs without the Mpc-scale environment contamination: isolated RGs.

HERGs and LERGs show significant differences. LERGs have larger BHs than HERGs, are less luminous in radio, and live in more massive galaxies. The HERG engine is radiatively efficient, and the host galaxy is rich in star-forming.

A similar result was found by Grandi et al. (2021) on a smaller sample.

The strength of this result lies in the comparison of isolated jetted AGN. We statistically show that nuclear and galactic differences are also present outside the clusters, suggesting that the main driver in producing AGN with different accretion rates is not the environment.

5.4 Radio morphology vs. environment

Once established that the LERG and HERG dichotomy is not related to the environment, we study if surrounding conditions could cause different radio morphologies.

Ma et al. (2019) classified a BH12 subsample of 15687 RGs in the radio band. They perform both an automatic convolutional neural network classification and a manual classification, visually inspecting FIRST radio images for each source. The two classifications agree for $\approx 80\%$ of sources. Given that a manual classification is validated only if at least three authors agree on the source morphology and that the automatic classification can misclassify small-scale and ambiguous RGs, we selected the manual classification for our analysis.

The radio classification performed manually is available in our sample for 6911 sources out of 7219 (96 %).

The AGN classified as FRIs or FRIIs are 2556 and 1150, respectively. The other sources were mostly compacts (3116).

5.4.1 FRI-LERGs vs. FRII-LERGs

Benefiting from the paper of Ma et al. (2019), it is possible to focus on LERGs radio morphologies in different environments. FRI-LERGs are 2141, 1219 found in isolated environments, while 738 are in clusters. FRII-LERGs are 1013, 454 isolated and 459 in clusters.

Table 5.3: FRI-LERGs/FRII-LERGs in clusters and in isolated environments.

Class	N TOT	IN	% IN	OUT	% OUT	unc association	% unc association
FRI-LERGs	2141	738	34	1219	57	184	9
FRII-LERGs	1013	459	45	454	45	100	10

FRI-LERGs prefer a poor environment. This is a surprising result since FRIs in the past were often associated to rich clusters. This was one of the milestones for the environmental scenario. Conversely, FRII-LERGs are associated with clusters or isolated environments with the same probability, as already found in our 3CR analysis (Macconi et al., 2020).

For both FRI-LERGs and FRII-LERGs, larger masses (M_{BH} and M_*) are found in clusters (see Tables 5.4 and 5.5). This is due to the fact that the majority of RGs in cluster are associated to the cluster BCG (1741 out of 2179, $\approx 80\%$). BCGs (found to concide with the cluster center Lin and Mohr 2004) are known to be the largest galaxies present in the universe, reaching masses of $\approx 10^{13}\ M/M_{\odot}$.

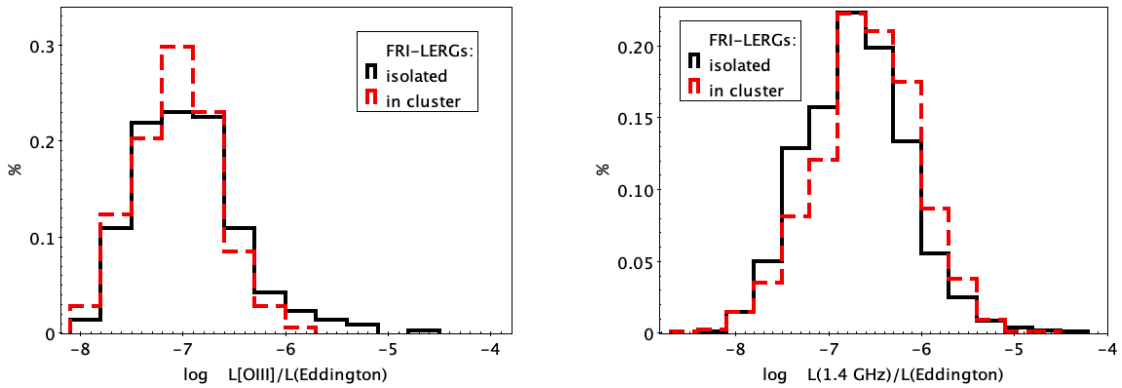

Figure 5.3: FRI-LERGs distribution in clusters (dashed red) and isolated environments (solid black) of $L_{[OIII]}/L_{Eddington}$ (left panel) and $L_{1.4\ GHz}/L_{Eddington}$ (right panel). For the [OIII] luminosity, there is no distinction between sources found in a different environment, for the radio power FRI-LERGs in cluster show larger values.

FRI-LERGs					
M_{BH}	M_*	D_n4000	sSFR	$L_{[OIII]}/L_{Eddington}$	$L_{1.4\ GHz}/L_{Eddington}$
$M_\odot$	$M_\odot$		yr^{-1}		
isolated: 1219					
Median values					
6.7×10^8	2.6×10^{11}	1.95	3.8×10^{-13}	1.0×10^{-7}	2.0×10^{-7}
cluster: 738					
Median values					
8.6×10^8	3.4×10^{11}	1.95	3.4×10^{-13}	8.9×10^{-8}	2.6×10^{-7}
KS test probability					
FRI-LERGs inside vs. outside:					
> 99.99 %	> 99.99 %	66 %	99.64 %	92.4 %	> 99.99 %

Table 5.4: Complete comparison between FRI-LERGs in a cluster and in an isolated environment.

Considering FRI-LERGs only, the stellar population (D_n4000) and sSFR do not significantly change passing from isolated to cluster environments (see Table 5.4). The same is true also considering $L_{[OIII]}/L_{Eddington}$ (see the left panel of Figure 5.3). Conversely, a significant difference is observed considering $L_{1.4\ GHz}/L_{Eddington}$. Summarizing, similar host galaxies and central engine properties are associated with larger radio power found in clusters.

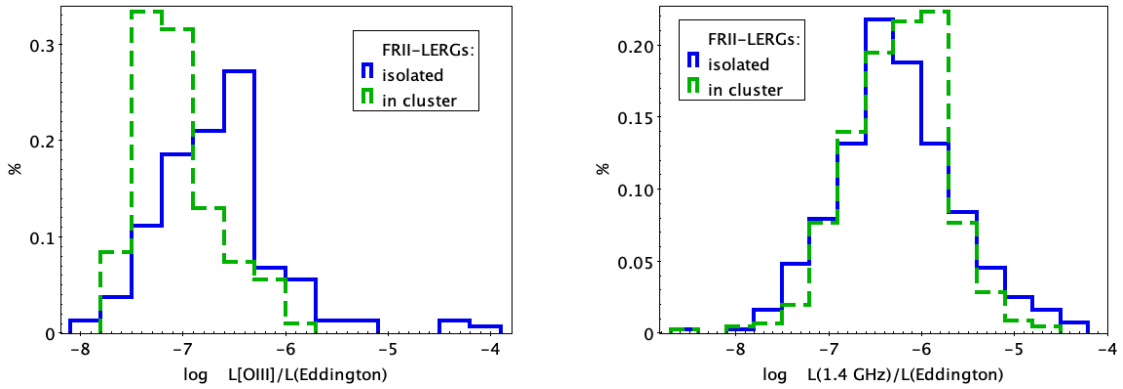

Figure 5.4: FRII-LERGs distribution in clusters (dashed green) and isolated environments (solid blue) of $L_{[OIII]}/L_{Eddington}$ (left panel) and $L_{1.4\ GHz}/L_{Eddington}$ (right panel). They show a significantly different distribution for the [OIII] line luminosity, with isolated sources characterized by larger values on average. This is not reflected in a radio power difference: they are found to show a similar distribution in terms of $L_{1.4\ GHz}/L_{Eddington}$, with cluster FRII-LERGs characterized by slightly larger (but not distinguishable) values on average.

FRII-LERGs					
M_{BH}	M_*	D_n4000	sSFR	$L_{[OIII]}/L_{Eddington}$	$L_{1.4\ GHz}/L_{Eddington}$
$M_\odot$	$M_\odot$		yr^{-1}		
isolated: 454					
Median values					
5.1×10^8	2.5×10^{11}	1.93	4.0×10^{-13}	2.2×10^{-7}	5.0×10^{-7}
cluster: 459					
Median values					
1.0×10^9	3.9×10^{11}	1.96	2.4×10^{-13}	7.5×10^{-8}	5.9×10^{-7}
KS test probability					
FRII-LERGs inside vs. outside:					
> 99.99 %	> 99.99 %	> 99.99 %	> 99.99 %	> 99.99 %	80%

Table 5.5: Complete comparison between FRII-LERGs in a cluster and in an isolated environment.

For FRII-LERGs, moving from isolated environments to clusters, the host galaxies' properties (D_n4000, sSFR) change significantly, with isolated sources characterized by larger current star-forming activity (see Table 5.5). Also the central engine activity ($L_{[OIII]}/L_{Eddington}$) is significantly more efficient in isolated environments, producing a similar radio power in both environments. Also in this case the environment is able to enhance the radio power, given a certain accretion rate. This agrees with what is found in the Jy sky, with FRII-LERGs being characterized by lower accretions when found in clusters (Macconi et al., 2020).

LERGs: FRIs vs. FRIIs					
M_{BH}	M_*	D_n4000	sSFR	$L_{[OIII]}/L_{Eddington}$	$L_{1.4\ GHz}/L_{Eddington}$
$M_\odot$	$M_\odot$		yr^{-1}		
KS test probability					
FRI-LERGs vs. FRII-LERGs in cluster:					
99.62 %	> 99.99 %	99.76 %	> 99.99 %	75 %	> 99.99 %
FRI-LERGs vs. FRII-LERGs in isolated environment:					
> 99.99 %	99.0 %	95.8 %	90.2 %	> 99.99 %	> 99.99 %

Table 5.6: KS tests between FRI-LERGs and FRII-LERGs.

FRI-LERGs and FRII-LERGs span a similar distribution of $L_{[OIII]}/L_{Eddington}$ when found in clusters, while they are distinguishable, with FRIIs being characterized by larger values, in isolated environments (see Table 5.6).

Conversely, in any environment they are characterized by different $L_{1.4\ GHz}/L_{Eddington}$ values: FRIIs are always found to possess larger values on average.

It is important to note that the $L_{1.4\ GHz}/L_{Eddington}$ distributions for different RGs populations is continuous and not sharp passing from FRI-LERGs to FRII-LERGs. This will be further discussed in Section 7, where a possible solution to the problem will be proposed.

Finally, we can compare the cluster richness for FRI-LERGs vs. FRII-LERGs found in clusters, to understand if the Mpc-scale environment is different for these classes.

FRI-LERGs have average and median values of 28 and 23, respectively. Instead, FRII-LERGs have an average value of 31 and a median value of 26. Therefore, the situation is: when found in clusters, FRI-LERGs and FRII-LERGs are found to reside in clusters with no distinguishable

richness ($P_{KS} = 99.53\%$, see Figure 5.5).

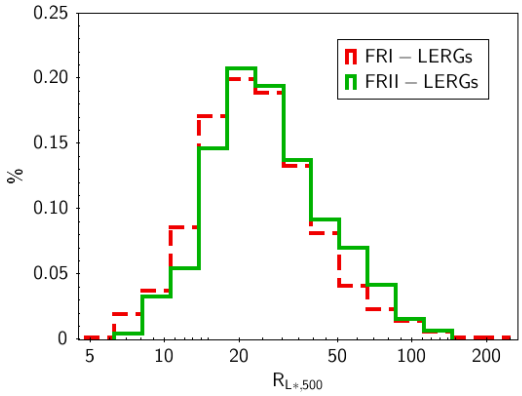

Figure 5.5: Comparison of FRI-LERGs (dashed red) with FRII-LERGs (solid green) cluster richness ($R_{L*,500}$) distribution. The two samples show a general overlap with FRII-LERGs found to reside in richer clusters on average.

Summarizing, the cluster can influence the radio power with a similar accretion; however, its role appears limited: (i) FRI-LERGs differ from FRII-LERGs in terms of radio power in any environment, (ii) they are found to span similar richness values when found in clusters, (iii) half of FRIIs (45%) and the majority of FRIs ($\approx 60\%$) are isolated, (iv) FRI-LERGs and FRII-LERGs show a significantly different $L_{[OIII]}/L_{Eddington}$ distributions when the large-scale environment cannot influence (i.e., in the isolated sub-sample). Thus, although the cluster can have a role in shaping RGs, it is not the main driver.

In the following Chapter, a single RG which jets interact with the medium is presented: NGC 5141. This interesting source was serendipitously discovered to host an X-ray cavity within its ISM.

The general discussion and conclusions about the main thesis project are in Section 7.

Chapter 6

The case of NGC 5141 X-ray cavity

During the X-ray analysis of a source belonging to the FRCAT sample (Capetti et al., 2017b), an X-ray surface brightness depression, compatible with an X-ray cavity (see e.g., Bîrzan et al., 2004), was serendipitously found within an elliptical/lenticular galaxy: NCG 5141 (a.k.a. UGC 08433).

6.1 NGC 5141 general properties

This local galaxy (z=0.017) was classified as lenticular by Nilson (1973); Condon and Broderick (1988), as a spiral-barred by Courteau et al. (2003) and as elliptical by Calvani et al. (1989); Véron-Cetty and Véron (2001); Pagotto et al. (2017). Huertas-Company et al. (2011) performed a Bayesian automated classification of SDSS DR7 galaxies, defined the classification as uncertain for NGC 5141, with a probability of 65% and of 32% of being an elliptical and an S0, respectively. Its disturbed morphology is probably the cause of a controversial classification. In fact, it is an interacting galaxy, as shown by its non-elliptical isophotes (Gonzalez-Serrano et al., 1993): NGC 5141 forms a dual system with its galaxy companion NGC 5142 (located $2.3'$ to the northeast, i.e., ≈ 50 kpc, Soares 1989). Signs of interaction between NGC 5141 and its companion were also provided by Emonts et al. (2010): two HI emitting clouds with mass of $\sim 6.9 \times 10^7$ $M_\odot$ were identified at a distance of 20 kpc from NGC 5141 center toward NGC 5142 direction, and HI absorbing gas slightly extended in the same direction, probably being part of the same structure. Both NGC 5141 and NGC 5142 are part of a group containing six galaxies.

The AGN within NGC 5141 is classified as LERG by Best and Heckman (2012). Being part of the GALEX-SDSS-WISE legacy, many information about the host galaxy are available (Salim et al., 2016, 2018): its stellar mass is $log\frac{M}{M_\odot} = 10.97 \pm 0.09$ $M_\odot$, with an associated star formation rate of $log(SFR) = -0.529 \pm 0.054$ $M_\odot$ yr^{-1}. Its stellar activity is compatible with an early-type galaxy, and its age is $t_{sys} \geq 12$ Gyrs (as calculated by Maraston 2005 and Maraston et al. 2009). Its central SMBH has a mass of $M_{BH} = (4 \pm 2) \times 10^8$ $M_\odot$, following the correlation by Marconi and Hunt (2003).

From the radio point of view, NGC 5141 was identified with the RG 4C +36.24 by Caswell and Wills (1967) and classified as a twin-jet Fanaroff-Riley type I (FRI) by Owen and Laing (1989). Its total radio luminosity at 1.4 GHz is $L(1.4\ GHz) = (8.2 \pm 0.3) \times 10^{39}$ erg s^{-1} (Condon and Broderick, 1988). Its radio emission is totally confined within the host galaxy, with a total linear extent of only

$\approx$ 19 kpc (Emonts et al., 2010). Parma et al. (1999), which studied the spectral aging of a sample of RGs in the 1.4-5 GHz spectral range, found that NGC 5141 is a radiatively young source, with a radiative age upper limit of $t_{age} < 4$ Myrs.

6.2 X-ray analysis

From the X-ray point of view, a single *Chandra* ACIS-S observation of this source (November 25, 2003, ObsID 4055) is available in the public archive with an exposure time of 31 ks. It was analyzed by Kharb et al. (2012), who focused on NGC 5141 nuclear emission, founding an extended structure ($\approx$ 4") associated with the southern radio jet.

Chandra data were reprocessed using the software CIAO 4.11 with CALDB 4.8.1. Good time intervals were defined by using the light curve to filter out times of background flares from the event file: the net exposure time is 26.8 ks. In the 0.5-7 keV image, the most interesting feature is the northern X-ray cavity. If VLA radio contours at 1.4 GHz, taken from the NRAO public archive, are superimposed on the smoothed X-ray image, the X-ray cavity position corresponds to the northern radio lobe (see Figure 6.3). In the southern hemisphere, X-ray emission is lacking on the galactic scale.

6.2.1 X-ray cavity significance

The cavity presence and its statistical significance were evaluated through various tests. Accounting for X-ray emission with radio contours superimposed, the cavity size was selected as a circle with 4.5 " radius.

As the first test, we compared the surface brightness (i.e., the counts number per unit area) inside the cavity vs. an annulus perfectly containing the cavity and posed at the same distance from the nucleus. From the control region, the cavity region and its surrounding bright rims were excluded. The cavity value is 0.094 counts arcsec^{-2}, while for the control region, it is 0.255 counts arcsec^{-2}. The cavity has a surface brightness reduced by $\approx$ 60% with respect to the control region. It was then possible to associate a significance level to the cavity detection following Ubertosi et al. (2021): the significance level is defined as $D/\Delta D$, where D is the percentage depression, calculated through the cavity (S_{CAV}) and control region (S_{CR}) surface brightnesses ($D = (1 - \frac{S_{CAV}}{S_{CR}}) \times 100$), while ΔD is the surface brightness propagation of uncertainty. Such calculated significance level is $\approx 4\sigma$.

Then, we calculated the cavity depression and its associated significance level by exploiting three other different control regions (all the control regions are reported in Figure 6.1):

1. the same annulus as before, not excluding the bright rims surrounding the X-ray cavity (control region=annulus-cavity). The resulting depression is $\approx$ 67% with a 4.9σ significance;

2. the same annulus as before, excluding the cavity, the surrounding bright rims and also a bright region in the west direction (control region=annulus-cavity-rims-west spot). In this case, the cavity depression is $\approx$ 39% with a significance of 1.5σ;

3. the same annulus as before, excluding also a putative southern cavity supposed to be at the same distance from the center as the northern one, with the same size and overlapping the southern radio lobe (control region=annulus-cavity-rims-west spot-putative southern cavity). The depression, in this case, is $\approx$ 45% with a significance of 1.9σ.

Following Pasini et al. (2021), another test was performed to check for the significance level of the cavity detection. The counts' number inside the cavity (six) was compared to the counts found within two circular regions with the same size, selected to be the nearest to the cavity region (but avoiding the bright rims, see Figure 6.1) at the same distance from the central nucleus. The significance level was calculated as a signal-to-noise ratio: $\frac{N_O - N_I}{\sqrt{N_O + N_I}}$, where N_I is the number of counts inside the cavity, and N_O is the counts' number of the control region. In this way, we obtained $\approx 2\sigma$ significance level, comparing the cavity counts with both control regions.

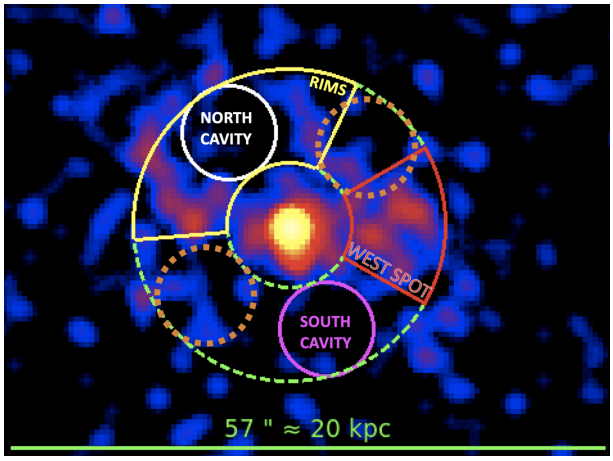

Figure 6.1: NGC 5141 in the 0.5-7 keV band and in logarithmic scale with scale parameter $\geq$0.035 counts per pixel and $\sigma = 2$ pixels of Gaussian smoothing. The regions exploited to test the cavity depression level and significance are highlighted: the detected cavity (north cavity) is in white, the region of the bright rims is in yellow, the west spot region is in red, the eventual south cavity is in purple, the two outer circles with same cavity size are in dashed orange and the 6-15 " annulus in dashed green.

Once the cavity detection is strengthened by these different statistical tests, an X-ray spectral analysis was performed to study the X-ray properties of the AGN and the gas surrounding the cavity.

6.2.2 Spectral analysis

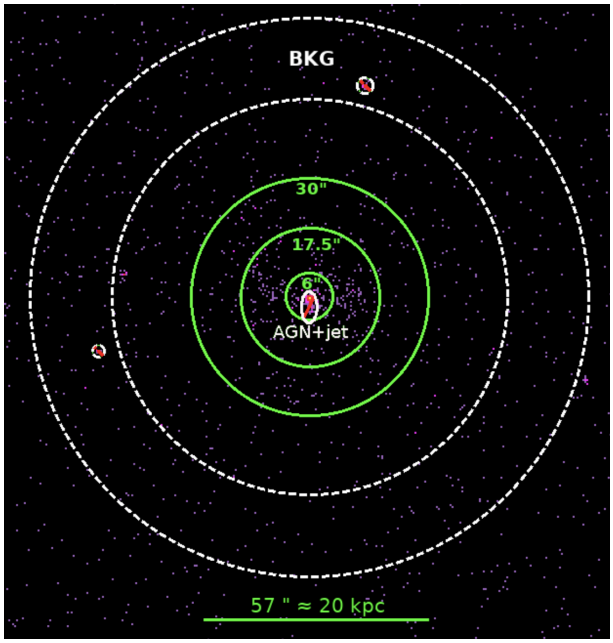

Figure 6.2: NGC 5141 0.5-7 keV Chandra image in logarithmic scale with no smoothing. The spectra extraction regions are reported as green annuli, the central AGN and jet contributions subtracted to study the diffuse X-ray emission are reported as the white central ellipse, the background region is reported as the large white dashed annulus.

For the spectral extraction and analysis, an annular background region within the same CCD was selected with inner and outer radii of 50" and 70", respectively, avoiding NGC 5141 extended structures (see Figure 6.2). Point-like sources falling within the background region were excluded. The X-ray spectral analysis was performed in the 0.5-7 keV energy band, exploiting XSPEC12.11.1 (Arnaud, 1996). Data were binned to contain at least two counts per bin, and Poissonian statistics was applied (i.e., the Cash statistics, Cstat, Cash 1979). The errors are at 1σ confidence level.

At first, the X-ray emission arising from the nucleus was analyzed: an X-ray spectrum from a circular region of 1.3" was extracted. The best-fit model is a power-law absorbed by an intrinsic column density, in addition to the Galactic column density absorption ($NH_{Gal} = 1.02 \times 10^{20}$ cm^{-2}, Kalberla et al. 2005). The intrinsic column density and spectral index values are $NH_{int} = 6 \pm 2 \times 10^{21}$ cm^{-2} and $\Gamma = 1.3 \pm 0.3$, respectively, consistent with the analysis performed by Kharb et al. (2012). It is then possible to calculate the unabsorbed 2-10 keV luminosity and to exploit it as a proxy of the accretion rate: the luminosity is $L_{2-10\ keV} = (8^{+4}_{-2}) \times 10^{40}$ erg s^{-1}, then the accretion-proxy value is $L_{2-10\ keV}/L_{Edd} = (2 \pm 1) \times 10^{-6}$. Such value is typical of LERG RGs (Macconi et al., 2020), in agreement with the optical classification performed by Best and Heckman (2012).

As we were interested in the properties of the gas surrounding the cavity, we followed an interactive procedure: (i) we analyzed the entire diffuse X-ray emission within the galaxy and found the best-fit; (ii) we divided such extended emission in annuli to characterize each specific region of the galaxy; (iii) we de-projected the emission to obtain electron density (n_e) values for

each region, including the region containing the cavity.

(i) The spectrum was extracted in a circular region centered on the nucleus with a radius of 30" from which the nuclear emission was carefully excluded (the elliptical region with a semi-major axis of 4" and semi-minor axis of 2"). The such region roughly corresponds to the optical galactic scale and contains all the detected galactic X-ray emission. The best-fit model is composed by a thermal emission (APEC, Astrophysical Plasma Emission Code, Smith et al. 2001) and a power-law spectrum, attenuated by the Galactic absorption. Given the poor statistics, the metal abundance was kept frozen to the solar value. The best-fit values are kT=0.80 ± 0.05 keV for the thermal emission and $\Gamma = 1.5 \pm 0.3$ for the power-law. The power-law addition strongly improved the fit statistics: the Cstat values changed from 107 with 110 degrees of freedom, with the thermal component only, to 69 for 108 degrees of freedom with power-law and thermal component. The power-law slope and 0.5-8 keV luminosity are fully compatible with unresolved emission from low-mass X-ray binaries (Irwin et al., 2003; Boroson et al., 2011; Lehmer et al., 2019), which are typically observed in nearby early-type galaxies ($L_{0.5-8\ keV} = (2.8 \pm 0.8) \times 10^{40}$ erg s^{-1}).

(ii) The same spectrum (APEC+POWER-LAW) was applied to three annular regions with radii 6, 17.5 and 30" (see Figure 6.2). The power-law slope was fixed to the 0-30" value ($\Gamma = 1.5$), while the APEC temperature was left free to vary in each annulus: $kT_{0-6} = 0.6^{+0.2}_{-0.3}$ keV, $kT_{6-17.5} = 0.89 \pm 0.07$ keV, and $kT_{17.5-30} = 0.75^{+0.08}_{-0.09}$ keV. Since all the found temperatures are compatible with the 0-30" temperature (kT=0.8 keV), this parameter was fixed to the 0-30" value for each annulus.

(iii) The PROJCT model was applied to the APEC component. The PROJCT model assumes spherical symmetry to de-projects 2D spectra (Smith et al., 2002). The obtained de-projected APEC normalization (N_{APEC}) is directly connected to each shell electron density for a collisionally ionized plasma with solar abundance (see, e.g. Gitti et al., 2012):

$$n_e = \sqrt{\frac{4\pi \cdot 10^{14} \cdot N_{\rm APEC} \cdot [D_L/(1+z)]^2}{0.82 \cdot V}} \tag{6.1}$$

where D_L is the luminosity distance ($D_L = 75.5$ Mpc with the adopted cosmology), z the redshift of the source, V the volume of the emitting region, and n_e the electron density (cm^{-3}). Thus, the n_e radial profile can be obtained for each shell and is reported in the left panel of Figure 6.4. In this fitting procedure, the power-law was left out of the de-projection with its normalization free to vary (see Su et al., 2017; Lakhchaura et al., 2018, for an analogous procedure)[1].

[1]We also verified the changes when both the power-law and thermal components are de-projected. This model is valid in the case of a spherical distribution for the X-ray binaries. The deprojected APEC normalization, in this case, is in full agreement with our best-fit model.

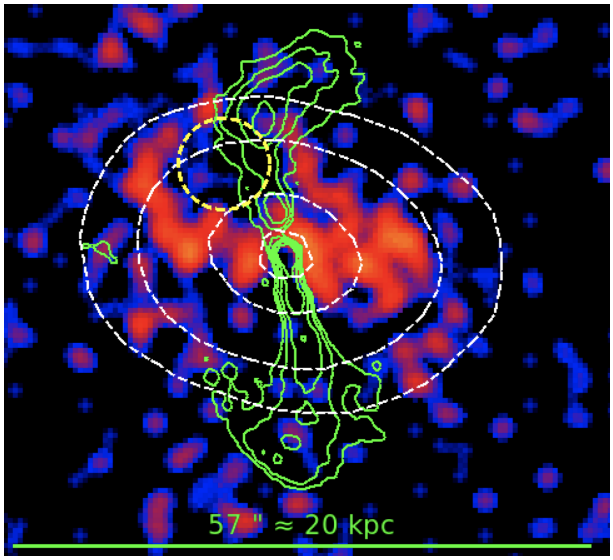

Figure 6.3: NGC 5141 Chandra 0.5-7 keV image with a logarithmic scale, Gaussian smoothing ($\sigma = 2$ pixels) and scale parameter ≥ 0.035 counts per pixels. The contribution from the central AGN and jets are subtracted as an ellipse (see text and Figure 6.2 for details). The cavity is shown as a yellow dashed circle with a radius of 4.5". Optical and radio contours are superimposed as white dashed and green contours, respectively. The optical emission is taken from SDSS g-band emission within 70% of NGC 5141 emitted light. The radio contours are taken from VLA at 1.4 GHz (NRAO Science Data Archive, with a resolution of 1.4" and an RMS of 0.1 mJy beam^{-1}) with contours level of -9, 9, 18, 36, 72, 144 $\times$RMS.

6.3 NGC 5141 heating power and cooling luminosity

6.3.1 The heating power

As described in the previous Section, through the X-ray spectral analysis, the electron density (n_e) in the region surrounding the X-ray cavity (annulus centered on the AGN with 6-17.5" radii) can be calculated: its value is $n_e = (3.3 \pm 0.3) \times 10^{-3}$ cm^{-3}. From this quantity, it is possible to calculate the corresponding gas pressure (e.g., Gitti et al., 2012) as: $P = nkT \approx 1.82 n_e kT \approx (7.7 \pm 0.9) \times 10^{-12}$ erg cm^{-3}. Then, from the gas pressure, it is possible to calculate the jet energy required to excavate the medium and produce the observed cavity as the sum of the work done by the lobes and their internal thermal energy (McNamara and Nulsen, 2007): $E_{cav} = \frac{\gamma}{\gamma - 1} P V_{cav}$, where γ is the ratio of the specific heats (equal to $\gamma = 4/3$ for relativistic plasma) and V_{cav} is the cavity volume. The energy obtained is $E_{cav} = (1.5 \pm 0.2) \times 10^{55}$ erg.

To estimate the average jet power, it is necessary to measure the cavity age. To this aim, all the three methods proposed by Bîrzan et al. (2004) were considered to estimate the cavity age: (i) the cavity rises from the nuclear vicinities through the ISM at the sound speed ($t_s = D/c_s$, where D is the projected distance and c_s is the sound speed); (ii) the cavity rises with buoyant speed ($t_b = D/\sqrt{\frac{2gV_{cav}}{SC}}$, where g is the gravitational acceleration, C is the drag coefficient, assumed to be 0.75 Churazov et al. 2001 and S is the cavity cross-section); (iii) the time required to refill its volume ($t_r = 2\sqrt{R_C/g}$). All three possible times and the resulting cavity power are calculated as

$P_{cav} = E_{cav}/t_{cav}$.

The estimated values are: (i) $(6.0 \pm 0.8) \times 10^{40}$ erg for t_s, (ii) $(5.6 \pm 0.8) \times 10^{40}$ erg for t_b and (iii) $(3.4 \pm 0.5) \times 10^{40}$ erg for t_r.

Since in the X-ray analysis, the gas metallicity was fixed to the solar abundance, which can affect the APEC normalization and then the estimated cavity power, different metallicities were also tested to evaluate the eventual variation of the P_{cav} values. We considered two extreme limits for solar metallicity: 0.3 and 2.0 solar abundance. In both cases, the estimated cavity power is within a factor 2 from our best-fit estimate ($E_{cav}/t_b \approx 9.6 \times 10^{40}$ erg s^{-1} for 0.3 and $E_{cav}/t_b \approx 3.5 \times 10^{40}$ erg s^{-1} for two solars). An eventual metallicity divergence from the one solar abundance does not have a strong impact on the final result.

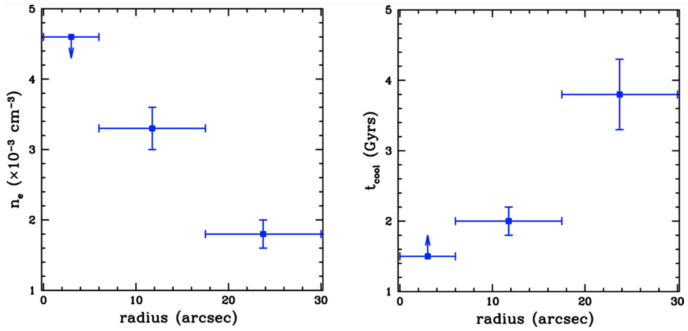

Figure 6.4: NGC 5141 radial profiles of the three concentric galaxy regions for the electron density (n_e, left panel, see Section 6.2.2) and cooling time (t_{cool}, right panel, Section 6.3.2) as calculated from the X-ray spectral analysis values.

6.3.2 The cooling luminosity

Once the gas density and temperature for a specific region are known, it is possible to estimate its cooling time: the time required by the gas to cool efficiently through radiative emission phenomena. This time is defined as $t_{cool} = \frac{\gamma}{\gamma-1} \frac{k\,T}{\mu X n_e \Lambda(T,Z)}$, where $\gamma = 5/3$ for monoatomic gas, μ is the mean molecular weight ($\mu \approx 0.61$ for solar abundances), X is the hydrogen mass fraction ($X = 0.71$ for solar abundances) and Λ is the cooling function, which value, for the source metallicity and temperature, is $\Lambda = 3.5 \times 10^{-23}$ erg cm^3 s^{-1} (Sutherland and Dopita, 1993). The values for each region are reported in the right panel of Figure 6.4.

The cooling time can be exploited to define the cooling radius (r_{cool}): the radius within which the cooling time equals the age of the system. It is a fundamental parameter since it delimits where the gas is able to cool effectively and, thus, the region where the cooling luminosity (L_{cool}), i.e., the thermal X-ray bolometric luminosity (0.1 - 100 keV), has to be calculated.

The age of the systems is often selected as the lookback time at z=1 for clusters and groups in literature, corresponding to a value of 7.7 Gyrs (Bîrzan et al., 2004, 2008; Cavagnolo et al., 2010; Eckert et al., 2021). To compare our results with previous studies, the same threshold was selected for NGC 5141. The 7.7 Gyrs value is longer than each region cooling time (see the right panel of Figure 6.4). Thus, the entire region (0-30") was considered to calculate the cooling luminosity: its value is $L_{cool} = (2.1 \pm 0.3) \times 10^{40}$ erg s^{-1}. We also considered 3 Gyrs as another possible threshold for t_{cool} to calculate L_{cool}, this value was proposed by Panagoulia et al. 2014. In this

case the 0-17.5" region is involved (Figure 6.4, right panel) and we obtain $L_{cool} \approx 1.2 \times 10^{40}$ erg s^{-1}. Thus, the cooling luminosity value is within a factor of 2 from our estimate.

6.3.3 Comparison with the literature

At first, it is interesting to compare NGC 5141 general properties with one of the largest sample of cavities (148), collected by Shin et al. (2016) exploiting *Chandra* data with different exposures (from a few to hundreds of ks). Such a sample covers a huge dynamical range, from isolated galaxies to rich clusters, and thus, a large range of values in terms of size, luminosity, temperature and power. As it is shown in Figure 6.5, NGC 5141 (the magenta star) is compared to the Shin et al. (2016) sample in terms of area, linear size, temperature and distance from the center, perfectly fitting the previously found correlations. This agreement, together with the statistical tests reported in Section 6.2.1, supports the effectiveness of NGC 5141 cavity detection.

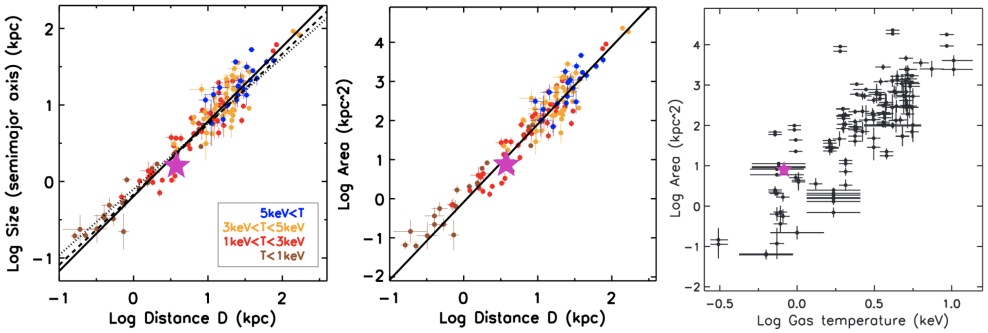

Figure 6.5: Plots from the large sample of X-ray cavities (148 in total) of Shin et al. (2016). The NGC 5141 cavity is reported as the magenta sta. *Left panel:* distance from the AGN vs. linear cavity size; *central panel:* distance vs. cavity area; *right panel:* X-ray thermal gas temperature vs. cavity area.

Once we have both P_{cav} and L_{cool} values, it is interesting to investigate if the system is balanced between heating and cooling and to compare NGC 5141 with literature cavities. In Figure 6.6 the NGC 5141 P_{cav}-L_{cool} values are compared with various systems found in literature, from giant ellipticals (Cavagnolo et al., 2010) to rich clusters(Bîrzan et al., 2008), passing through galaxy groups O'Sullivan et al. (2011). NGC 5141 is reported as the magenta star; it follows the general trend in the bottom left corner of the plot. To the best of our knowledge, there are only other two galaxies with a low cavity power as NGC 5141, i.e., $< 10^{41}$ erg s^{-1}: they are NGC 3608 and NGC 4477. NGC 3608 is part of the Cavagnolo et al. (2010) sample and is reported in Figure 6.6 as a yellow-filled red square. It has a cavity power similar to NGC 5141 ($\approx 10^{40}$ erg s^{-1}). NGC 4477 was discovered by Li et al. (2018) and it is the weakest cavity known ($P_{cav} \approx 10^{39}$ erg s^{-1}). Unfortunately, NGC 4477 cannot be reported in Figure 6.6, since a different cooling time threshold was selected to calculate its cooling luminosity. However, NGC 5141 shows fundamental differences with both NGC 3608 and NGC 4477:

1. NGC 3608 and NGC 4477 have a cooler ISM (kT$\approx$ 0.3 keV) than NGC 5141;
2. NGC 3608 and NGC 4477 show multiple cavities within their galaxy, while NGC 5141 shows a single cavity;

3. most importantly, *NGC 3608 and NGC 4477 do not show extended radio emission, the only evidence for a clear connection between jet activity and X-ray cavities. They are both ghost cavities* (Bîrzan et al., 2004)). NGC 3608 was not detected in the radio band even with LOFAR (Bîrzan et al., 2020).

Thus, NGC 5141 represents a unique example of a galaxy possessing a low-power X-ray cavity within the ISM and clearly connected to jet activity, as demonstrated by the lobes emission. Thanks to NGC 5141, the P_{cav}/L_{cool} relation is expanded at the lower edge of power for radio-filled systems. This confirms that the heating-cooling relation, mainly tested for giant ellipticals, groups, and clusters, also works for such low-power systems (Macconi et al., 2022).

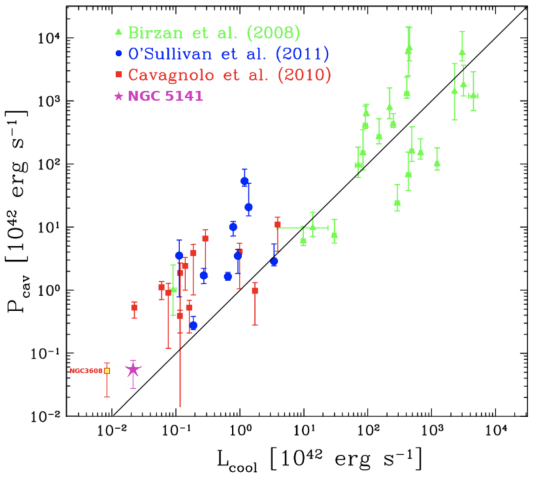

Figure 6.6: X-ray cooling luminosity (Section 6.3.2) vs. cavity power (Section 6.3.1) plot taken from Gitti et al. (2012). X-ray cavities found in different environments are represented with different symbols: red squares from Cavagnolo et al. (2010) are in giant ellipticals, blue circles from O'Sullivan et al. (2011) are in groups, green triangles from Bîrzan et al. (2008). The black diagonal line represents the equilibrium between heating and cooling ($P_{cav} = L_{cool}$).

Chapter 7

Discussion and conclusions

The RGs "classical" view - the stronger the accretion the more powerful the jet (discussed in Section 2.2.3) - has been questioned by the study of FRII-LERGs, i.e., jetted AGN showing low accretion rates and FRII morphologies. As they do not fit the general picture, their exploration is unavoidable in better understanding the accretion and ejection processes in AGN.

This thesis presents our results based on multiwavelength studies of local ($z < 0.3$) jetted AGN, spanning radio flux density from a few mJy to several Jy. The X-ray study of the powerful (Jy) radio galaxies belonging to the 3CR sample has allowed us to exclude that FRII-LERGs are highly obscured sources. The X-ray properties are intermediate, as attested by their moderate intrinsic column density ($N_H \approx 10^{22} cm^{-2}$) and Eddington-scaled X-ray luminosities between FRII-HERGs and FRI-LERGs. These results outlined at least two different scenarios: 1) FRII-LERGs represent an evolutionary stage of classical FRII-HERGs. They accreted efficiently in the past, producing powerful jets, then they recently switched off their nuclear activity, possibly because of the exhaustion of cold gas fuel; 2) FRII-LERGs represent a third class of RGs in addition to FRI-LERGs and FRII-HERGs.Their accretion mode was, and still is, inefficient. The launched relativistic plasma can assume different morphologies depending on the medium through which it passes.

Our study was then expanded to the mJy sky to disentangle between these possibilities, allowing us to explore richer samples of RGs with a thousand times lower flux density in the same redshift range.

From Jy to mJy flux densities, there are two major changes in the RGs populations: (i) LERGs become the dominant population, and (ii) the majority of FRIIs are observed at low radio power and with accretion levels lower than “classical” FRII-HERGs. In the local mJy universe, the FRII morphology associated with an inefficient accretion is the most probable configuration. FRIs are still the fainter objects in agreeement with Mingo et al. (2019). who explored the first LOFAR data release (Shimwell et al., 2019; Williams et al., 2019) at low frequencies.

We note that the scarcity of low-power FRII-LERGs in the Jy sky compared to the mJy surveys can be explained as an observational bias. In Figure 7.1, the $L_{1.4\ GHz}$ vs. z plot is presented for Jy (3CR) and mJy (FRCAT) sources. It is evident that going down in radio flux densities, the region of low luminosity becomes more populated. The 3CR sample represents the tip of the iceberg of a more variegated population that was missed by the Jy surveys because of the high flux density threshold.

This threshold is is reported as the red dashed line in Figure 7.1. It is calculated by converting the 3CR flux limit threshold (9 Jy at 178 MHz, Bennett 1962) at 1.4 GHz using $\alpha = -0.7$ as spectral index.

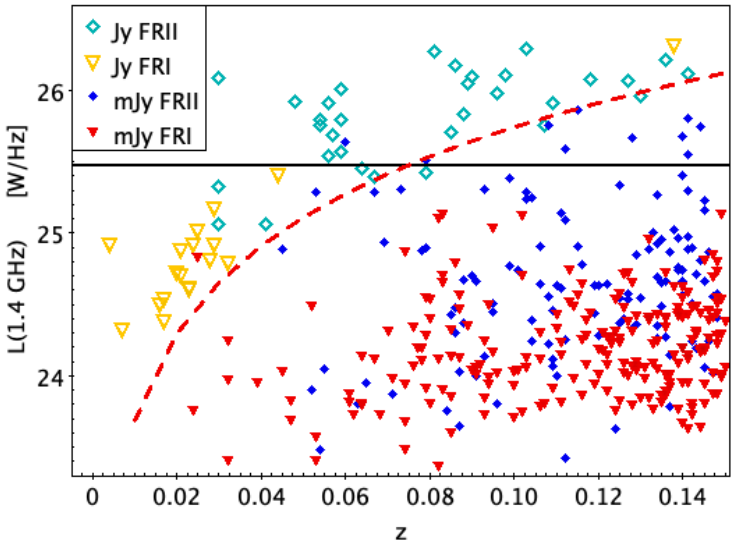

Figure 7.1: Redshift vs. radio luminosity at 1.4 GHz (in W Hz^{-1}) for the 3CR sample (Jy flux density limited) and the FRCAT sample (mJy flux density limited). For both samples, triangles indicate FRIs (yellow for 3CR and red for FRCAT), while rhombuses are for FRIIs (cyan for 3CR and blue for FRCAT). For the 3CR sample, the symbols are empty, while they are filled for the FRCAT. The solid black line highlights the power dichotomy threshold between FRIs and FRIIs at 1.4 GHz in the Jy sky ($logL \approx 25.48\ W\ Hz^{-1}$, i.e., $L \approx 3 \times 10^{25}\ W\ Hz^{-1}$, Tadhunter 2016). The red dashed curve indicates the radio luminosity corresponding to 2 Jy flux density limit for different redshift values.

From a comparison between Jy and mJy FRII-LERGs, it emerges that lower radio flux density sources have, on average, FRI-like characteristics, while FRII-LERGs of the 3C sample are more "active", with intermediate properties between FRIs and FRII-HERGs. Statistical analysis of the FRCAT catalogs (see section 4.1.2) indicates that FRII-LERGs have more massive black holes, larger stellar masses and a more evolved stellar population than FRII-HERGs. This would point towards an evolutive scenario, which can be tested following different methods.

(I) In the FRIICAT sample, FRIIs hosting LERGs engine are 89% of the total. A similar result was found by Miraghaei and Best (2017), who analyzed another Best and Heckman (2012) subsample performing an independent FRI/FRII classification, with FRII-LERGs being $\approx 80\%$ of the total FRII at z<0.1. Thus, about eight/nine FRIIs out of ten in the local mJy universe would be in a transitory stage being the engine has changed its accretion mode. It is necessary to understand if such a large percentage of transitory sources is compatible with FRIIs properties. A typical FRII edge-brightened morphology produces hot-spots. Such structures rapidly disappear, with a fading time scale $\leq 10^6$ yr (Saxton et al., 2010; Turner and Shabala, 2015; Godfrey et al., 2017). A change in the accretion mode from efficient to inefficient should prevent plasma replenishing at the lobe's edge and the hot-spots are expected to disappear in such a short time. In this case,

FRII-LERGs should be a rare configuration. In particular, if we assume the hot-spot fading time as an estimate of the FRII-LERG life and we divide it by the typical RL-AGN duty cycle of $\approx$ 10–100 Myrs (Kaiser and Cotter, 2002; Martini, 2004; Antognini et al., 2012; Kapinska et al., 2015; Godfrey et al., 2017; Turner et al., 2018; Shabala et al., 2020), from a statistical point of view FRII-LERGs should not exceed $\leq 10\%$ of the sample (i.e., one source out of 10–100). In the 3CR sample, FRII-LERGs represent $\approx 17\%$ of the sources with optical and radio classification at $z < 0.15$ (one out of six). In the FRCAT, FRII-LERGs are one out of three sources with both classifications at $z < 0.15$. The same percentage ($\approx 32\%$) is found in our sample at $0.05 < z < 0.3$. In the Miraghaei and Best (2017) sample, FRII-LERGs are one out of four RGs at $z < 0.1$. The FRII-LERGs high percentage in the local universe cannot be reconciled, as the unique solution, with a transitory phase. Any high ($>> 10\%$) observed fraction of remnant and restarted sources would require a dominant population of short-lived jets (Shabala et al., 2020).

(II) To evaluate evolution, it is also possible to consider the FRII-LERGs progenitors number, i.e., FRII-HERGs. The number of FRII-HERGs in our sample is 45 in total (Section 5), while the total number of cross-classified AGN is 3231. For the typical AGN duty cycle of $10^7 - 10^8$ yr, the only two possibilities to justify the number discrepancy are: (i) FRII-HERGs are an uncommon configuration in the local universe, which would make it impossible to justify the large FRII-LERGs number if FRII-HERGs are their progenitors; (ii) FRII-HERG engines are common but really short-lived configurations. It is possible to estimate the FRII-HERGs life-time as $\propto N(FRII-HERGs)/N(classified\ AGN) \times t_{duty} \approx 45/3231 \times t_{duty} \approx 10^5 - 10^6$ yr. Such a short life-time is not supported by age estimates of FRII engines (see, e.g. Bird et al., 2008).

(III) It is also possible to exploit the host-galaxies properties of HERGs and compare them with those of FRII-LERGs. If FRIIs have just become LERGs from an original HERG engine within a short time scale (to not be visible on lobes-scales), they should span similar values in the stellar population, which have longer time scales ($> 10^8$ yr): i.e., D_n 4000, sSFR, $L_{H\alpha}$. As shown in Figure 7.2, this is not the case: the two populations show different distributions for all the analyzed quantities with a probability above 3σ, independently of the environment.

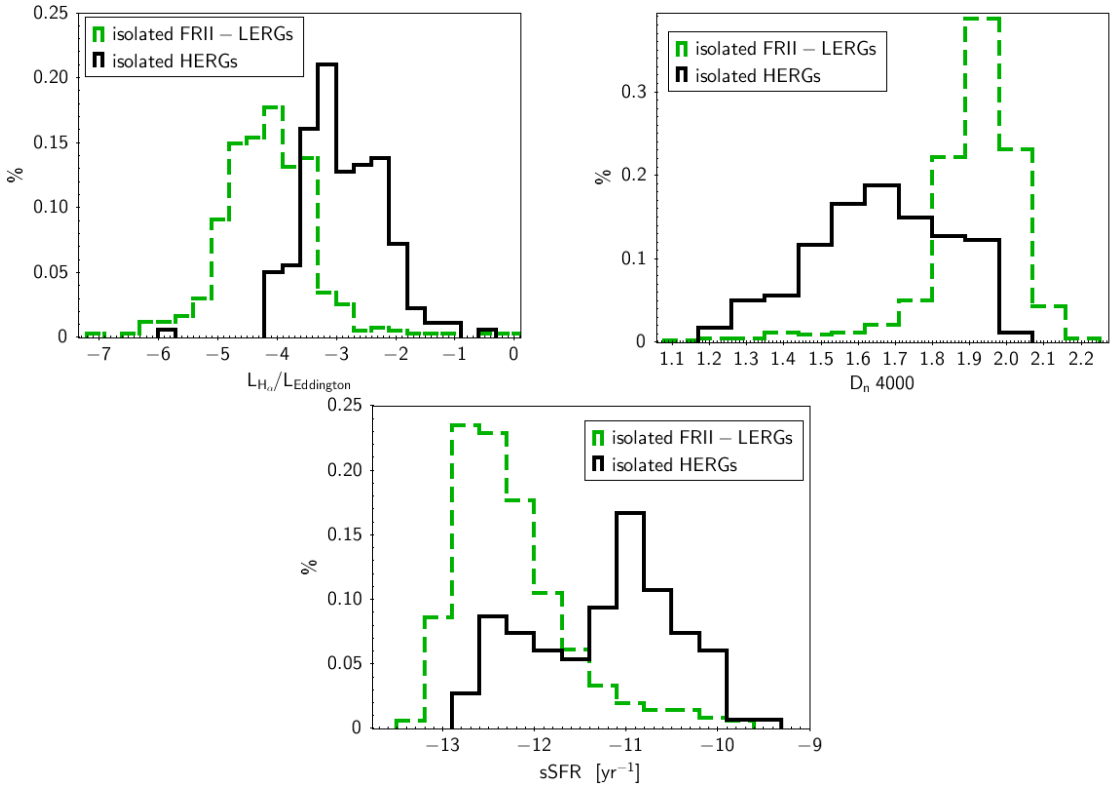

Figure 7.2: Isolated FRII-LERGs (dashed green) host galaxies properties are compared to isolated HERGs (solid black) to test the evolutionary scenario. Left panel: $L_{H\alpha}$ as normalized by the Eddington luminosity; central panel: calcium break; right panel: sSFR.

We cannot reject the hypothesis that FRII-LERGs are a separate class. Theoretical studies show that inefficient accretion configurations between an ADAF and a cold, efficient disc can exist (see Figure 1 of Yuan and Narayan (2014)). If, for some reason, more viscous dissipated energy is transferred into electrons and radiated away, the ADAF accretion flow can enter into a more luminous hot accretion flow regime (Xie and Yuan, 2012). If the electron cooling becomes too strong, the matter in accretion collapses in a cold disc or in cold, dense clumps embedded in a hot flow (Yuan and Narayan, 2014). We could then be observing the inverse trend. FRII-LERGs are a separate and independent class with an inefficient accretion regime able to produce extended FRII radio structures. In this latter case, the environment could not play an important role.

Thanks to a galaxy clusters sample taken by Wen and Han (2015), the role of Mpc-scale environment was investigated for 7219 RGs belonging to the Best and Heckman (2012) main sample at $0.05 < z < 0.3$ (section 5). The most important result is that RGs are preferentially isolated, avoiding crowded environments. In the HERG-LERG dichotomy, the sources are characterized by different central engine accretion rates, different stellar populations, host galaxy masses, and different radio power. More importantly, the LERGs and HERGs dichotomy remains in RGs outside the clusters. The different accretion configurations are independent of the environment.

When the radio classification is also considered, it turns out that FRI-LERGs generally live in isolated ambients. This impressive result completely changes the current picture (and our conclu-

sions based on the 3CR sample), assuming that FRI-LERGs generally lie in clusters. The idea that the environment is not the main driver of the jet morphology is strengthened, even if we cannot exclude it still plays some role. Indeed, (i) for RGs in clusters, the interaction with the external environment enhances their radio power and, (ii) comparing LERGs sources inside and outside the clusters, the former show lower star formation rates, massive BHs and galaxies independently of their FRI-FRII classification. This is because most RGs associated with a cluster are found to be BCG ($\approx 80\%$), i.e., the most evolved and massive galaxies known. In addition, inside galaxy clusters, mergings phenomena and/or other possible galaxies interactions contributed in increasing the galaxy mass earlier than in isolated galaxies.

As discussed in Section 2.2.3, from the theoretical point of view, two mechanisms are thought to be responsible for launching relativistic jets: the BZ effect (Blandford and Znajek, 1977) and/or the BP effect (Blandford and Payne, 1982). These two mechanisms are not mutually exclusive and can collaborate. A spinning BH is observed to be necessary in producing ballistic jets in X-ray binaries (Narayan and McClintock, 2012; Steiner et al., 2013). However, many RQ Seyfert galaxies are found to possess a large spin value (see, e.g. Reynolds, 2014). A spinning BH appears necessary to produce jets but not a sufficient condition (Saikia, 2022). Therefore, the spin alone (the so-called spin paradigm, Blandford 1990; Blandford and Begelman 1999; Wilson and Colbert 1995) cannot explain the RL-RQ dichotomy.

From a theoretical point of view, the spin could be fundamental within RL AGN: sources characterized by a geometrically thick, inefficient accretion disc (ADAF) are found to span a wide range of jet power (≥ 1000) only changing the spin value within the range 0.2–1.0 (Tchekhovskoy et al., 2010). The same is not valid for a thin disc (SSD), where a substantial change in the spin value does not correspond to a significant change in the jet power (≈ 10). Thus, RGs characterized by thick discs with a similar accretion could span a wide P_{jet} value depending on their SMBH spin only.

From an observational perspective, the jet power is correlated with the accretion disc, in a large sample of blazars (i.e., face-on RGs, see Section 2.1), with the jet extracting more energy than those accreted (Ghisellini et al., 2014): the spin contribution (in addition to the accretion rate contribution) is thought to be fundamental for the resulting jet power/morphology also for Blazars.

A large spin range value would naturally justify the wide jet power distribution values associated with similar accretion rates, as shown in Section 5.4.1. Since the role of the environment is limited (see Section 5) and the majority of sources are found in isolated environments, the two main ingredients necessary to shape different jet power and morphologies are the central engine accretion mode and the SMBH spin. Given the independence of such two parameters, their combined distribution would be consistent with a wide and continuous jet power distribution for LERGs.

In particular, the different radio luminosities observed in LERGs having comparable radiative power ($L_{[OIII]}/L_{Eddington}$) might indicate that similar nuclear engines produce different accelerations to the outflowing plasma. Thus, the accretion mode is not the key parameter to explain the class segregation of LERGs. The FRI/FRII dichotomy could directly depend on different values of the SMBH spin (Blandford and Znajek, 1977), with FRII-LERGs supposed to host the fastest spinning SMBHs (Grandi et al., 2021).

This scenario also enables us to explain the nature of the recently discovered FR0s (Baldi et al., 2018). These sources are characterized by similar properties as FRI-LERGs, except for their jet

extension ($<$ 5 kpc). In this case, a slow-rotating SMBH would prevent the formation of a strong and collimated relativistic jet, even if all the other ingredients are present.

7.1 Future perspectives

7.1.1 High-resolution X-ray/radio monitoring

The simultaneous study of the RGs nuclear emission in radio and X-ray bands can provide fundamental improvements in testing the evolutionary scenario. Thanks to the high angular resolution achieved in both bands ($<$arcsec), sub-kpc regions can be characterized in the local universe. In this context, a systematic study can be performed. The two bands are tracing different AGN emissions: X-rays define the accretion efficiency onto the SMBH, radio band traces the resulting power of the launched jet. Both Chandra and XMM-Newton archives can be exploited in the X-ray band, since a huge amount of RGs data are available with many observations over years. From the radio point of view, different monitoring surveys are present: MOJAVE and TANAMI monitoring have been tracing AGN activity near the jet launching region for more than ten years. MOJAVE (Monitoring Of Jets in Active galactic nuclei with VLBA Experiments, Lister et al. 2018) is a long-term systematic Very Long Baselines Array (VLBA) monitoring program to characterize jets produced by AGN at different radio frequencies (7mm, 1.3cm, 2cm). It ensures an angular resolution ≤ 1 milliarcsec, enabling a pc-scale resolution at $z < 0.05$. There are more than 200 AGN present with systematic monitoring since 1994 and still ongoing.

The TANAMI project (i.e., Tracking Active Galactic Nuclei with Austral Milliarcsecond Interferometry, Ojha et al. 2010) represents a similar project observing in the southern sky since 2007 still ongoing. It monitors 135 RL AGN with a milliarcsec resolution at two different wavelengths: 1.3 and 3.5 cm. It has a multiwavelength approach with a high-energy counterpart observations program (Swift, XMM-Newton, Suzaku, INTEGRAL, Fermi/LAT).

7.1.2 Spectral mapping of radio emission with new radio facilities

Exploiting the present (VLASS, LOFAR) and future (SKA) radio surveys, a spectral mapping study of the extended radio emission for local RGs can be explored. In particular, performing a spectral analysis mapping for RGs with different optical and radio classifications would allow an understanding of the particles ageing. As already discussed, there are structures rapidly sensitive to jet changes (i.e., hot-spots), for which a recent jet speed/structure modification is seen within 10^6 yr. The spectral mapping trend of jet radio emission (lobes, plumes, hot-spots) can verify different scenarios proposed in this work: (i) the evolutionary possibility and (ii) the matter entrainment by the jet in different environments. In this case, the interaction between the jet and its surrounding medium can be analyzed and the role of a large-scale environment can be quantified.

List of Figures

Bibliography

Kevork N. Abazajian, Jennifer K. Adelman-McCarthy, Marcel A. Agüeros, Sahar S. Allam, Carlos Allende Prieto, Deokkeun An, Kurt S. J. Anderson, Scott F. Anderson, James Annis, Neta A. Bahcall, C. A. L. Bailer-Jones, J. C. Barentine, Bruce A. Bassett, Andrew C. Becker, Timothy C. Beers, Eric F. Bell, Vasily Belokurov, Andreas A. Berlind, Eileen F. Berman, Mariangela Bernardi, Steven J. Bickerton, Dmitry Bizyaev, John P. Blakeslee, Michael R. Blanton, John J. Bochanski, William N. Boroski, Howard J. Brewington, Jarle Brinchmann, J. Brinkmann, Robert J. Brunner, Tamás Budavári, Larry N. Carey, Samuel Carliles, Michael A. Carr, Francisco J. Castander, David Cinabro, A. J. Connolly, István Csabai, Carlos E. Cunha, Paul C. Czarapata, James R. A. Davenport, Ernst de Haas, Ben Dilday, Mamoru Doi, Daniel J. Eisenstein, Michael L. Evans, N. W. Evans, Xiaohui Fan, Scott D. Friedman, Joshua A. Frieman, Masataka Fukugita, Boris T. Gänsicke, Evalyn Gates, Bruce Gillespie, G. Gilmore, Belinda Gonzalez, Carlos F. Gonzalez, Eva K. Grebel, James E. Gunn, Zsuzsanna Györy, Patrick B. Hall, Paul Harding, Frederick H. Harris, Michael Harvanek, Suzanne L. Hawley, Jeffrey J. E. Hayes, Timothy M. Heckman, John S. Hendry, Gregory S. Hennessy, Robert B. Hindsley, J. Hoblitt, Craig J. Hogan, David W. Hogg, Jon A. Holtzman, Joseph B. Hyde, Shin-ichi Ichikawa, Takashi Ichikawa, Myungshin Im, Željko Ivezić, Sebastian Jester, Linhua Jiang, Jennifer A. Johnson, Anders M. Jorgensen, Mario Jurić, Stephen M. Kent, R. Kessler, S. J. Kleinman, G. R. Knapp, Kohki Konishi, Richard G. Kron, Jurek Krzesinski, Nikolay Kuropatkin, Hubert Lampeitl, Svetlana Lebedeva, Myung Gyoon Lee, Young Sun Lee, R. French Leger, Sébastien Lépine, Nolan Li, Marcos Lima, Huan Lin, Daniel C. Long, Craig P. Loomis, Jon Loveday, Robert H. Lupton, Eugene Magnier, Olena Malanushenko, Viktor Malanushenko, Rachel Mandelbaum, Bruce Margon, John P. Marriner, David Martínez-Delgado, Takahiko Matsubara, Peregrine M. McGehee, Timothy A. McKay, Avery Meiksin, Heather L. Morrison, Fergal Mullally, Jeffrey A. Munn, Tara Murphy, Thomas Nash, Ada Nebot, Jr. Neilsen, Eric H., Heidi Jo Newberg, Peter R. Newman, Robert C. Nichol, Tom Nicinski, Maria Nieto-Santisteban, Atsuko Nitta, Sadanori Okamura, Daniel J. Oravetz, Jeremiah P. Ostriker, Russell Owen, Nikhil Padmanabhan, Kaike Pan, Changbom Park, George Pauls, Jr. Peoples, John, Will J. Percival, Jeffrey R. Pier, Adrian C. Pope, Dimitri Pourbaix, Paul A. Price, Norbert Purger, Thomas Quinn, M. Jordan Raddick, Paola Re Fiorentin, Gordon T. Richards, Michael W. Richmond, Adam G. Riess, Hans-Walter Rix, Constance M. Rockosi, Masao Sako, David J. Schlegel, Donald P. Schneider, Ralf-Dieter Scholz, Matthias R. Schreiber, Axel D. Schwope, Uroš Seljak, Branimir Sesar, Erin Sheldon, Kazu Shimasaku, Valena C. Sibley, A. E. Simmons, Thirupathi Sivarani, J. Allyn Smith, Martin C. Smith, Vernesa Smolčić, Stephanie A. Snedden, Albert Stebbins, Matthias Steinmetz, Chris Stoughton, Michael A. Strauss, Mark SubbaRao, Yasushi Suto, Alexander S. Szalay, István Szapudi, Paula Szkody, Masayuki Tanaka, Max Tegmark,

Luis F. A. Teodoro, Aniruddha R. Thakar, Christy A. Tremonti, Douglas L. Tucker, Alan Uomoto, Daniel E. Vanden Berk, Jan Vandenberg, S. Vidrih, Michael S. Vogeley, Wolfgang Voges, Nicole P. Vogt, Yogesh Wadadekar, Shannon Watters, David H. Weinberg, Andrew A. West, Simon D. M. White, Brian C. Wilhite, Alainna C. Wonders, Brian Yanny, D. R. Yocum, Donald G. York, Idit Zehavi, Stefano Zibetti, and Daniel B. Zucker. The Seventh Data Release of the Sloan Digital Sky Survey. ApJS, 182(2):543–558, June 2009. doi: 10.1088/0067-0049/182/2/543.

A. A. Abdo, M. Ackermann, M. Ajello, W. B. Atwood, L. Baldini, J. Ballet, G. Barbiellini, D. Bastieri, B. M. Baughman, K. Bechtol, R. Bellazzini, B. Berenji, R. D. Blandford, Bloom ..., and Fermi LAT Collaboration. Fermi Gamma-Ray Imaging of a Radio Galaxy. Science, 328: 725, May 2010. doi: 10.1126/science.1184656.

M. Ackermann, M. Ajello, L. Baldini, J. Ballet, G. Barbiellini, D. Bastieri, R. Bellazzini, E. Bissaldi, R. D. Blandford, E. D. Bloom, R. Bonino, T. J. Brandt, J. Bregeon, P. Bruel, R. Buehler, S. Buson, G. A. Caliandro, R. A. Cameron, M. Caragiulo, P. A. Caraveo, E. Cavazzuti, C. Cecchi, E. Charles, A. Chekhtman, S. Cheung, C. ..., and Fermi LAT Collaboration. Fermi Large Area Telescope Detection of Extended Gamma-Ray Emission from the Radio Galaxy Fornax A. ApJ, 826:1, July 2016. doi: 10.3847/0004-637X/826/1/1.

Joe Antognini, Jonathan Bird, and Paul Martini. The Lifetime and Powers of FR IIs in Galaxy Clusters. ApJ, 756(2):116, September 2012. doi: 10.1088/0004-637X/756/2/116.

Robert Antonucci. Unified models for active galactic nuclei and quasars. Annual Review of Astronomy and Astrophysics, 31:473–521, January 1993. doi: 10.1146/annurev.aa.31.090193.002353.

K. A. Arnaud. XSPEC: The First Ten Years. In George H. Jacoby and Jeannette Barnes, editors, Astronomical Data Analysis Software and Systems V, volume 101 of Astronomical Society of the Pacific Conference Series, page 17, January 1996.

Y. Avni. Energy spectra of X-ray clusters of galaxies. ApJ, 210:642–646, Dec 1976. doi: 10.1086/154870.

R. D. Baldi, A. Capetti, and F. Massaro. FR0CAT: a FIRST catalog of FR 0 radio galaxies. A & A, 609:A1, January 2018. doi: 10.1051/0004-6361/201731333.

J. A. Baldwin, M. M. Phillips, and R. Terlevich. Classification parameters for the emission-line spectra of extragalactic objects. Publications of the Astronomical Society of the Pacific, 93: 5–19, February 1981. doi: 10.1086/130766.

B. Balmaverde, A. Capetti, and P. Grandi. The Chandra view of the 3C/FR I sample of low luminosity radio-galaxies. A & A, 451:35–44, May 2006. doi: 10.1051/0004-6361:20053799.

B. Balmaverde, A. Capetti, P. Grandi, E. Torresi, M. Chiaberge, J. Rodriguez Zaurin, G. R. Tremblay, D. J. Axon, S. A. Baum, G. Giovannini, P. Kharb, F. D. Macchetto, C. P. O'Dea, and W. Sparks. Extended soft X-ray emission in 3CR radio galaxies at z < 0.3: high excitation and broad line galaxies. A & A, 545:A143, Sep 2012. doi: 10.1051/0004-6361/201219561.

Michael Balogh, Vince Eke, Chris Miller, Ian Lewis, Richard Bower, Warrick Couch, Robert Nichol, Joss Bland-Hawthorn, Ivan K. Baldry, Carlton Baugh, Terry Bridges, Russell Cannon, Shaun Cole, Matthew Colless, Chris Collins, Nicholas Cross, Gavin Dalton, Roberto de Propris, Simon P. Driver, George Efstathiou, Richard S. Ellis, Carlos S. Frenk, Karl Glazebrook, Percy Gomez, Alex Gray, Edward Hawkins, Carole Jackson, Ofer Lahav, Stuart Lumsden, Steve Maddox, Darren Madgwick, Peder Norberg, John A. Peacock, Will Percival, Bruce A. Peterson, Will Sutherland, and Keith Taylor. Galaxy ecology: groups and low-density environments in the SDSS and 2dFGRS. MNRAS, 348(4):1355–1372, March 2004. doi: 10.1111/j.1365-2966.2004.07453.x.

Peter D. Barthel. Is Every Quasar Beamed? ApJ, 336:606, January 1989. doi: 10.1086/167038.

Robert H. Becker, Richard L. White, and David J. Helfand. The FIRST Survey: Faint Images of the Radio Sky at Twenty Centimeters. ApJ, 450:559, September 1995. doi: 10.1086/176166.

A. S. Bennett. The revised 3C catalogue of radio sources. Memoirs of the Royal Astronomical Society, 68:163, January 1962.

P. N. Best. The environmental dependence of radio-loud AGN activity and star formation in the 2dFGRS. MNRAS, 351(1):70–82, June 2004. doi: 10.1111/j.1365-2966.2004.07752.x.

P. N. Best and T. M. Heckman. On the fundamental dichotomy in the local radio-AGN population: accretion, evolution and host galaxy properties. MNRAS, 421(2):1569–1582, April 2012. doi: 10.1111/j.1365-2966.2012.20414.x.

P. N. Best, G. Kauffmann, T. M. Heckman, and Ž. Ivezić. A sample of radio-loud active galactic nuclei in the Sloan Digital Sky Survey. MNRAS, 362(1):9–24, September 2005. doi: 10.1111/j.1365-2966.2005.09283.x.

Stefano Bianchi and Matteo Guainazzi. The nature of the soft X-ray emission in obscured AGN. In Tiziana di Salvo, Gian Luca Israel, Luciano Piersant, Luciano Burderi, Giorgio Matt, Amedeo Tornambe, and Maria Teresa Menna, editors, The Multicolored Landscape of Compact Objects and Their Explosive Origins, volume 924 of American Institute of Physics Conference Series, pages 822–829, Aug 2007. doi: 10.1063/1.2774948.

Jonathan Bird, Paul Martini, and Christian Kaiser. The Lifetime of FR II Sources in Groups and Clusters: Implications for Radio-Mode Feedback. ApJ, 676(1):147–162, March 2008. doi: 10.1086/527534.

L. Bîrzan, D. A. Rafferty, B. R. McNamara, M. W. Wise, and P. E. J. Nulsen. A Systematic Study of Radio-induced X-Ray Cavities in Clusters, Groups, and Galaxies. ApJ, 607(2):800–809, June 2004. doi: 10.1086/383519.

L. Bîrzan, B. R. McNamara, P. E. J. Nulsen, C. L. Carilli, and M. W. Wise. Radiative Efficiency and Content of Extragalactic Radio Sources: Toward a Universal Scaling Relation between Jet Power and Radio Power. ApJ, 686(2):859–880, Oct 2008. doi: 10.1086/591416.

L. Bîrzan, D. A. Rafferty, M. Brüggen, A. Botteon, G. Brunetti, V. Cuciti, A. C. Edge, R. Morganti, H. J. A. Röttgering, and T. W. Shimwell. LOFAR observations of X-ray cavity systems. MNRAS, 496(3):2613–2635, June 2020. doi: 10.1093/mnras/staa1594.

G. M. Blake. Fluid dynamic stability of double radio sources. MNRAS, 156:67, January 1972. doi: 10.1093/mnras/156.1.67.

R. D. Blandford. Physical processes in active galactic nuclei. In R. D. Blandford, H. Netzer, L. Woltjer, T. J. L. Courvoisier, and M. Mayor, editors, Active Galactic Nuclei, pages 161–275, January 1990.

R. D. Blandford and A. Königl. Relativistic jets as compact radio sources. ApJ, 232:34–48, August 1979. doi: 10.1086/157262.

R. D. Blandford and D. G. Payne. Hydromagnetic flows from accretion disks and the production of radio jets. MNRAS, 199:883–903, Jun 1982. doi: 10.1093/mnras/199.4.883.

R. D. Blandford and R. L. Znajek. Electromagnetic extraction of energy from Kerr black holes. MNRAS, 179:433–456, May 1977. doi: 10.1093/mnras/179.3.433.

Roger D. Blandford and Mitchell C. Begelman. On the fate of gas accreting at a low rate on to a black hole. MNRAS, 303(1):L1–L5, February 1999. doi: 10.1046/j.1365-8711.1999.02358.x.

Michael R. Blanton, David W. Hogg, Neta A. Bahcall, J. Brinkmann, Malcolm Britton, Andrew J. Connolly, István Csabai, Masataka Fukugita, Jon Loveday, Avery Meiksin, Jeffrey A. Munn, R. C. Nichol, Sadanori Okamura, Thomas Quinn, Donald P. Schneider, Kazuhiro Shimasaku, Michael A. Strauss, Max Tegmark, Michael S. Vogeley, and David H. Weinberg. The Galaxy Luminosity Function and Luminosity Density at Redshift z = 0.1. ApJ, 592(2):819–838, August 2003. doi: 10.1086/375776.

B. Boccardi, T. P. Krichbaum, E. Ros, and J. A. Zensus. Radio observations of active galactic nuclei with mm-VLBI. The Astronomy and Astrophysics Review, 25(1):4, November 2017. doi: 10.1007/s00159-017-0105-6.

B. Boccardi, M. Perucho, C. Casadio, P. Grandi, D. Macconi, E. Torresi, S. Pellegrini, T. P. Krichbaum, M. Kadler, G. Giovannini, V. Karamanavis, L. Ricci, E. Madika, U. Bach, E. Ros, M. Giroletti, and J. A. Zensus. Jet collimation in NGC 315 and other nearby AGN. A & A, 647:A67, March 2021. doi: 10.1051/0004-6361/202039612.

J. G. Bolton, G. J. Stanley, and O. B. Slee. Positions of Three Discrete Sources of Galactic Radio-Frequency Radiation. Nature, 164(4159):101–102, July 1949. doi: 10.1038/164101b0.

M. Bonzini, P. Padovani, V. Mainieri, K. I. Kellermann, N. Miller, P. Rosati, P. Tozzi, and S. Vattakunnel. The sub-mJy radio sky in the Extended Chandra Deep Field-South: source population. MNRAS, 436(4):3759–3771, December 2013. doi: 10.1093/mnras/stt1879.

Bram Boroson, Dong-Woo Kim, and Giuseppina Fabbiano. REVISITING WITHCHANDRATHE SCALING RELATIONS OF THE x-RAY EMISSION COMPONENTS (BINARIES, NUCLEI, AND HOT GAS) OF EARLY-TYPE GALAXIES. The Astrophysical Journal, 729(1):12, feb 2011. doi: 10.1088/0004-637x/729/1/12. URL https://doi.org/10.1088%2F0004-637x%2F729%2F1%2F12.

L. Burtscher, K. Meisenheimer, K. R. W. Tristram, W. Jaffe, S. F. Hönig, R. I. Davies, M. Kishimoto, J. U. Pott, H. Röttgering, M. Schartmann, G. Weigelt, and S. Wolf. A diversity of dusty AGN tori. Data release for the VLTI/MIDI AGN Large Program and first results for 23 galaxies. A & A, 558:A149, October 2013. doi: 10.1051/0004-6361/201321890.

H. Butcher and Jr. Oemler, A. The evolution of galaxies in clusters. V. A study of populations since Z 0.5. ApJ, 285:426–438, October 1984. doi: 10.1086/162519.

S. Buttiglione, A. Capetti, A. Celotti, D. J. Axon, M. Chiaberge, F. D. Macchetto, and W. B. Sparks. An optical spectroscopic survey of the 3CR sample of radio galaxies with z < 0.3. I. Presentation of the data. A & A, 495:1033–1060, March 2009. doi: 10.1051/0004-6361:200811102.

S. Buttiglione, A. Capetti, A. Celotti, D. J. Axon, M. Chiaberge, F. D. Macchetto, and W. B. Sparks. An optical spectroscopic survey of the 3CR sample of radio galaxies with z < 0.3 . II. Spectroscopic classes and accretion modes in radio-loud AGN. A & A, 509:A6, January 2010. doi: 10.1051/0004-6361/200913290.

Massimo Calvani, Giovanni Fasano, and Alberto Franceschini. On the Relationship between Radio Emission and Optical Properties in Early-Type Galaxies. ApJ, 97:1319, May 1989. doi: 10.1086/115075.

A. Capetti, F. Massaro, and R. D. Baldi. FRIICAT: A FIRST catalog of FR II radio galaxies. A & A, 601:A81, May 2017a. doi: 10.1051/0004-6361/201630247.

A. Capetti, F. Massaro, and R. D. Baldi. FRICAT: A FIRST catalog of FR I radio galaxies. A & A, 598:A49, February 2017b. doi: 10.1051/0004-6361/201629287.

W. Cash. Parameter estimation in astronomy through application of the likelihood ratio. ApJ, 228: 939–947, March 1979. doi: 10.1086/156922.

J. L. Caswell and D. Wills. Identifications of radio sources with bright galaxies. MNRAS, 135: 231, January 1967. doi: 10.1093/mnras/135.2.231.

K. W. Cavagnolo, B. R. McNamara, P. E. J. Nulsen, C. L. Carilli, C. Jones, and L. Bîrzan. A Relationship Between AGN Jet Power and Radio Power. ApJ, 720(2):1066–1072, Sep 2010. doi: 10.1088/0004-637X/720/2/1066.

Marco Chiaberge, F. Duccio Macchetto, William B. Sparks, Alessandro Capetti, Mark G. Allen, and André R. Martel. The Nuclei of Radio Galaxies in the Ultraviolet: The Signature of Different Emission Processes. ApJ, 571(1):247–255, May 2002. doi: 10.1086/339846.

E. Churazov, M. Brüggen, C. R. Kaiser, H. Böhringer, and W. Forman. Evolution of Buoyant Bubbles in M87. ApJ, 554(1):261–273, June 2001. doi: 10.1086/321357.

R. Cid Fernandes, G. Stasińska, M. S. Schlickmann, A. Mateus, N. Vale Asari, W. Schoenell, and L. Sodré. Alternative diagnostic diagrams and the 'forgotten' population of weak line galaxies in the SDSS. MNRAS, 403(2):1036–1053, April 2010. doi: 10.1111/j.1365-2966.2009.16185.x.

J. J. Condon and J. J. Broderick. Radio Identification of UGC Galaxies: Starbursts and Monsters. ApJ, 96:30, July 1988. doi: 10.1086/114788.

J. J. Condon, W. D. Cotton, E. W. Greisen, Q. F. Yin, R. A. Perley, G. B. Taylor, and J. J. Broderick. The NRAO VLA Sky Survey. ApJ, 115(5):1693–1716, May 1998. doi: 10.1086/300337.

Michael C. Cooper, Jeffrey A. Newman, Benjamin J. Weiner, Renbin Yan, Christopher N. A. Willmer, Kevin Bundy, Alison L. Coil, Christopher J. Conselice, Marc Davis, S. M. Faber, Brian F. Gerke, Puragra Guhathakurta, David C. Koo, and Kai G. Noeske. The DEEP2 Galaxy Redshift Survey: the role of galaxy environment in the cosmic star formation history. MNRAS, 383(3):1058–1078, January 2008. doi: 10.1111/j.1365-2966.2007.12613.x.

Stéphane Courteau, David R. Andersen, Matthew A. Bershady, Lauren A. MacArthur, and Hans-Walter Rix. The Tully-Fisher Relation of Barred Galaxies. ApJ, 594(1):208–224, September 2003. doi: 10.1086/376754.

J. H. Croston, M. J. Hardcastle, B. Mingo, P. N. Best, J. Sabater, T. M. Shimwell, W. L. Williams, K. J. Duncan, H. J. A. Röttgering, M. Brienza, G. Gürkan, J. Ineson, G. K. Miley, L. M. Morabito, S. P. O'Sullivan, and I. Prandoni. The environments of radio-loud AGN from the LOFAR Two-Metre Sky Survey (LoTSS). A & A, 622:A10, February 2019. doi: 10.1051/0004-6361/201834019.

Chris Done, S. W. Davis, C. Jin, O. Blaes, and M. Ward. Intrinsic disc emission and the soft X-ray excess in active galactic nuclei. MNRAS, 420(3):1848–1860, March 2012. doi: 10.1111/j.1365-2966.2011.19779.x.

A. Dressler. Galaxy morphology in rich clusters: implications for the formation and evolution of galaxies. ApJ, 236:351–365, March 1980. doi: 10.1086/157753.

Dominique Eckert, Massimo Gaspari, Fabio Gastaldello, Amandine M. C. Le Brun, and Ewan O'Sullivan. Feedback from Active Galactic Nuclei in Galaxy Groups. Universe, 7(5):142, May 2021. doi: 10.3390/universe7050142.

B. H. C. Emonts, R. Morganti, C. Struve, T. A. Oosterloo, G. van Moorsel, C. N. Tadhunter, J. M. van der Hulst, E. Brogt, J. Holt, and N. Mirabal. Large-scale HI in nearby radio galaxies - II. The nature of classical low-power radio sources. MNRAS, 406(2):987–1006, August 2010. doi: 10.1111/j.1365-2966.2010.16706.x.

G. Fabbiano, D. W. Kim, and G. Trinchieri. An X-Ray Catalog and Atlas of Galaxies. The Astrophysical Journal Supplement Series, 80:531, Jun 1992. doi: 10.1086/191675.

A. C. Fabian, K. Iwasawa, C. S. Reynolds, and A. J. Young. Broad Iron Lines in Active Galactic Nuclei. Publication of the Astronomical Society of the Pacific, 112(775):1145–1161, September 2000. doi: 10.1086/316610.

Andrew C. Fabian and Giovanni Miniutti. The X-ray spectra of accreting Kerr black holes. arXiv e-prints, art. astro-ph/0507409, July 2005.

B. L. Fanaroff and J. M. Riley. The morphology of extragalactic radio sources of high and low luminosity. MNRAS, 167:31P–36P, May 1974. doi: 10.1093/mnras/167.1.31P.

E. D. Feigelson and P. I. Nelson. Statistical methods for astronomical data with upper limits. I. Univariate distributions. ApJ, 293:192–206, Jun 1985. doi: 10.1086/163225.

G. Fossati, L. Maraschi, A. Celotti, A. Comastri, and G. Ghisellini. A unifying view of the spectral energy distributions of blazars. MNRAS, 299:433–448, September 1998. doi: 10.1046/j.1365-8711.1998.01828.x.

M. A. Gendre, P. N. Best, J. V. Wall, and L. M. Ker. The relation between morphology, accretion modes and environmental factors in local radio AGN. MNRAS, 430:3086–3101, Apr 2013. doi: 10.1093/mnras/stt116.

G. Ghisellini and A. Celotti. The dividing line between FR I and FR II radio-galaxies. A & A, 379:L1–L4, Nov 2001. doi: 10.1051/0004-6361:20011338.

G. Ghisellini, A. Celotti, G. Fossati, L. Maraschi, and A. Comastri. A theoretical unifying scheme for gamma-ray bright blazars. MNRAS, 301(2):451–468, December 1998. doi: 10.1046/j.1365-8711.1998.02032.x.

G. Ghisellini, F. Tavecchio, L. Maraschi, A. Celotti, and T. Sbarrato. The power of relativistic jets is larger than the luminosity of their accretion disks. Nature, 515(7527):376–378, Nov 2014. doi: 10.1038/nature13856.

Myriam Gitti, Fabrizio Brighenti, and Brian R. McNamara. Evidence for AGN Feedback in Galaxy Clusters and Groups. Advances in Astronomy, 2012:950641, January 2012. doi: 10.1155/2012/950641.

L. E. H. Godfrey and S. S. Shabala. AGN Jet Kinetic Power and the Energy Budget of Radio Galaxy Lobes. ApJ, 767(1):12, Apr 2013. doi: 10.1088/0004-637X/767/1/12.

L. E. H. Godfrey, R. Morganti, and M. Brienza. On the population of remnant Fanaroff-Riley type II radio galaxies and implications for radio source dynamics. MNRAS, 471(1):891–907, October 2017. doi: 10.1093/mnras/stx1538.

Percy L. Gómez, Robert C. Nichol, Christopher J. Miller, Michael L. Balogh, Tomotsugu Goto, Ann I. Zabludoff, A. Kathy Romer, Mariangela Bernardi, Ravi Sheth, Andrew M. Hopkins, Francisco J. Castander, Andrew J. Connolly, Donald P. Schneider, Jon Brinkmann, Don Q. Lamb, Mark SubbaRao, and Donald G. York. Galaxy Star Formation as a Function of Environment in the Early Data Release of the Sloan Digital Sky Survey. ApJ, 584(1):210–227, February 2003. doi: 10.1086/345593.

J. I. Gonzalez-Serrano, R. Carballo, and I. Perez-Fournon. The Optical Properties of Low Luminosity Radio Galaxies With Radio Jets. ApJ, 105:1710, May 1993. doi: 10.1086/116548.

Paola Grandi, Giuseppe Malaguti, and Mariateresa Fiocchi. BeppoSAX View of Radio-loud Active Galactic Nuclei. ApJ, 642:113–125, May 2006. doi: 10.1086/500100.

Paola Grandi, Eleonora Torresi, Duccio Macconi, Bia Boccardi, and Alessandro Capetti. Jet-Accretion System in the Nearby mJy Radio Galaxies. ApJ, 911(1):17, April 2021. doi: 10.3847/1538-4357/abe776.

V. Guglielmo, B. M. Poggianti, B. Vulcani, S. Maurogordato, J. Fritz, M. Bolzonella, S. Fotopoulou, C. Adami, and M. Pierre. The XXL Survey. XXXVII. The role of the environment in shaping the stellar population properties of galaxies at $0.1 \leq z \leq 0.5$. A & A, 625:A112, May 2019. doi: 10.1051/0004-6361/201834970.

F. Haardt and L. Maraschi. A Two-Phase Model for the X-Ray Emission from Seyfert Galaxies. ApJL, 380:L51, October 1991. doi: 10.1086/186171.

M. J. Hardcastle. B_{gg} revisited: The environments of low-excitation radio galaxies and unified models. A & A, 414:927–929, February 2004. doi: 10.1051/0004-6361:20035605.

M. J. Hardcastle, D. A. Evans, and J. H. Croston. Hot and cold gas accretion and feedback in radio-loud active galaxies. MNRAS, 376:1849–1856, Apr 2007. doi: 10.1111/j.1365-2966.2007.11572.x.

Yasuhiro Hashimoto, Jr. Oemler, Augustus, Huan Lin, and Douglas L. Tucker. The Influence of Environment on the Star Formation Rates of Galaxies. ApJ, 499(2):589–599, May 1998. doi: 10.1086/305657.

T. M. Heckman. An Optical and Radio Survey of the Nuclei of Bright Galaxies - Activity in the Normal Galactic Nuclei. A & A, 87:152, July 1980.

Timothy M. Heckman and Philip N. Best. The Coevolution of Galaxies and Supermassive Black Holes: Insights from Surveys of the Contemporary Universe. Annual Review of Astronomy and Astrophysics, 52:589–660, Aug 2014. doi: 10.1146/annurev-astro-081913-035722.

Timothy M. Heckman, Guinevere Kauffmann, Jarle Brinchmann, Stéphane Charlot, Christy Tremonti, and Simon D. M. White. Present-Day Growth of Black Holes and Bulges: The Sloan Digital Sky Survey Perspective. ApJ, 613(1):109–118, September 2004. doi: 10.1086/422872.

R. G. Hine and M. S. Longair. Optical spectra of 3CR radio galaxies. MNRAS, 188:111–130, July 1979. doi: 10.1093/mnras/188.1.111.

M. Huertas-Company, J. A. L. Aguerri, M. Bernardi, S. Mei, and J. Sánchez Almeida. Revisiting the Hubble sequence in the SDSS DR7 spectroscopic sample: a publicly available Bayesian automated classification. A & A, 525:A157, January 2011. doi: 10.1051/0004-6361/201015735.

J. Ineson, J. H. Croston, M. J. Hardcastle, R. P. Kraft, D. A. Evans, and M. Jarvis. The link between accretion mode and environment in radio-loud active galaxies. MNRAS, 453:2682–2706, Nov 2015. doi: 10.1093/mnras/stv1807.

Jimmy A. Irwin, Alex E. Athey, and Joel N. Bregman. X-Ray Spectral Properties of Low-Mass X-Ray Binaries in Nearby Galaxies. ApJ, 587(1):356–366, April 2003. doi: 10.1086/368179.

T. Isobe, E. D. Feigelson, and P. I. Nelson. Statistical Methods for Astronomical Data with Upper Limits. II. Correlation and Regression. ApJ, 306:490, Jul 1986. doi: 10.1086/164359.

Christian R. Kaiser and Garret Cotter. The death of FR II radio sources and their connection with radio relics. MNRAS, 336(2):649–658, October 2002. doi: 10.1046/j.1365-8711.2002.05799.x.

P. M. W. Kalberla, W. B. Burton, Dap Hartmann, E. M. Arnal, E. Bajaja, R. Morras, and W. G. L. Pöppel. The Leiden/Argentine/Bonn (LAB) Survey of Galactic HI. Final data release of the combined LDS and IAR surveys with improved stray-radiation corrections. A & A, 440:775–782, Sep 2005. doi: 10.1051/0004-6361:20041864.

A. D. Kapinska, M. Hardcastle, C. Jackson, T. An, W. Baan, and M. Jarvis. Unravelling lifecycles and physics of radio-loud AGN in the SKA Era. In Advancing Astrophysics with the Square Kilometre Array (AASKA14), page 173, April 2015. doi: 10.22323/1.215.0173.

Jun Kataoka and Łukasz Stawarz. X-Ray Emission Properties of Large-Scale Jets, Hot Spots, and Lobes in Active Galactic Nuclei. ApJ, 622:797–810, April 2005. doi: 10.1086/428083.

Y. Kato, S. Mineshige, and K. Shibata. Magnetohydrodynamic Accretion Flows: Formation of Magnetic Tower Jet and Subsequent Quasi-Steady State. ApJ, 605(1):307–320, April 2004. doi: 10.1086/381234.

K. I. Kellermann, R. Sramek, M. Schmidt, D. B. Shaffer, and R. Green. VLA Observations of Objects in the Palomar Bright Quasar Survey. ApJ, 98:1195, Oct 1989. doi: 10.1086/115207.

K. I. Kellermann, R. A. Sramek, M. Schmidt, R. F. Green, and D. B. Shaffer. The Radio Structure of Radio Loud and Quiet Quasars in the Palomar Bright Quasar Survey. ApJ, 108:1163, October 1994. doi: 10.1086/117145.

Lisa J. Kewley, Brent Groves, Guinevere Kauffmann, and Tim Heckman. The host galaxies and classification of active galactic nuclei. MNRAS, 372:961–976, November 2006. doi: 10.1111/j.1365-2966.2006.10859.x.

P. Kharb, C. P. O'Dea, A. Tilak, S. A. Baum, E. Haynes, J. Noel-Storr, C. Fallon, and K. Christiansen. VLBA and Chandra Observations of Jets in FRI Radio Galaxies: Constraints on Jet Evolution. ApJ, 754(1):1, July 2012. doi: 10.1088/0004-637X/754/1/1.

John Kormendy and Luis C. Ho. Coevolution (Or Not) of Supermassive Black Holes and Host Galaxies. ARAA, 51(1):511–653, August 2013. doi: 10.1146/annurev-astro-082708-101811.

John Kormendy and Douglas Richstone. Inward Bound—The Search For Supermassive Black Holes In Galactic Nuclei. ARAA, 33:581, January 1995. doi: 10.1146/annurev.aa.33.090195.003053.

Julian H. Krolik and Gerard A. Kriss. Observable Properties of X-Ray–heated Winds in Active Galactic Nuclei: Warm Reflectors and Warm Absorbers. ApJ, 447:512, July 1995. doi: 10.1086/175896.

R. A. Laing, C. R. Jenkins, J. V. Wall, and S. W. Unger. Spectrophotometry of a Complete Sample of 3CR Radio Sources: Implications for Unified Models. In Geoffrey V. Bicknell, Michael A. Dopita, and Peter J. Quinn, editors, The Physics of Active Galaxies, volume 54 of Astronomical Society of the Pacific Conference Series, page 201, January 1994.

K. Lakhchaura, N. Werner, M. Sun, R. E. A. Canning, M. Gaspari, S. W. Allen, T. Connor, M. Donahue, and C. Sarazin. Thermodynamic properties, multiphase gas, and AGN feedback in a large sample of giant ellipticals. MNRAS, 481(4):4472–4504, December 2018. doi: 10.1093/mnras/sty2565.

A. Lawrence. The relative frequency of broad-lined and narrow-lined active galactic nuclei : implications for unified schemes. MNRAS, 252:586, October 1991. doi: 10.1093/mnras/252.4.586.

Michael J. Ledlow and Frazer N. Owen. 20 CM VLA Survey of Abell Clusters of Galaxies. VI. Radio/Optical Luminosity Functions. ApJ, 112:9, July 1996. doi: 10.1086/117985.

Bret D. Lehmer, Rafael T. Eufrasio, Panayiotis Tzanavaris, Antara Basu-Zych, Tassos Fragos, Andrea Prestwich, Mihoko Yukita, Andreas Zezas, Ann E. Hornschemeier, and Andrew Ptak. X-Ray Binary Luminosity Function Scaling Relations for Local Galaxies Based on Subgalactic Modeling. ApJS, 243(1):3, July 2019. doi: 10.3847/1538-4365/ab22a8.

Yijia Li, Yuanyuan Su, and Christine Jones. X-ray cavities in the hot corona of the lenticular galaxy NGC 4477. MNRAS, 480(4):4279–4286, November 2018. doi: 10.1093/mnras/sty2125.

Alan P. Lightman and Timothy R. White. Effects of Cold Matter in Active Galactic Nuclei: A Broad Hump in the X-Ray Spectra. ApJ, 335:57, Dec 1988. doi: 10.1086/166905.

Yen-Ting Lin and Joseph J. Mohr. K-band Properties of Galaxy Clusters and Groups: Brightest Cluster Galaxies and Intracluster Light. ApJ, 617(2):879–895, December 2004. doi: 10.1086/425412.

M. L. Lister, M. F. Aller, H. D. Aller, M. A. Hodge, D. C. Homan, Y. Y. Kovalev, A. B. Pushkarev, and T. Savolainen. MOJAVE. XV. VLBA 15 GHz Total Intensity and Polarization Maps of 437 Parsec-scale AGN Jets from 1996 to 2017. ApJS, 234(1):12, January 2018. doi: 10.3847/1538-4365/aa9c44.

D. Lynden-Bell. Gravity power. , 17:185–191, March 1978. doi: 10.1088/0031-8949/17/3/009.

Zhixian Ma, Haiguang Xu, Jie Zhu, Dan Hu, Weitian Li, Chenxi Shan, Zhenghao Zhu, Liyi Gu, Jinjin Li, Chengze Liu, and Xiangping Wu. A Machine Learning Based Morphological Classification of 14,245 Radio AGNs Selected from the Best-Heckman Sample. ApJS, 240(2):34, February 2019. doi: 10.3847/1538-4365/aaf9a2.

D. Macconi, E. Torresi, P. Grandi, B. Boccardi, and C. Vignali. Radio morphology-accretion mode link in Fanaroff-Riley type II low-excitation radio galaxies. MNRAS, 493(3):4355–4366, April 2020. doi: 10.1093/mnras/staa560.

Duccio Macconi, Paola Grandi, Myriam Gitti, Cristian Vignali, Eleonora Torresi, and Fabrizio Brighenti. Detection of a radio-filled X-ray cavity within the interstellar medium of NGC 5141. A & A, 660:A32, April 2022. doi: 10.1051/0004-6361/202143024.

John Magorrian, Scott Tremaine, Douglas Richstone, Ralf Bender, Gary Bower, Alan Dressler, S. M. Faber, Karl Gebhardt, Richard Green, Carl Grillmair, John Kormendy, and Tod Lauer. The Demography of Massive Dark Objects in Galaxy Centers. ApJ, 115:2285–2305, June 1998. doi: 10.1086/300353.

Claudia Maraston. Evolutionary population synthesis: models, analysis of the ingredients and application to high-z galaxies. MNRAS, 362(3):799–825, September 2005. doi: 10.1111/j.1365-2966.2005.09270.x.

Claudia Maraston, G. Strömbäck, D. Thomas, D. A. Wake, and R. C. Nichol. Modelling the colour evolution of luminous red galaxies - improvements with empirical stellar spectra. MNRAS, 394 (1):L107–L111, March 2009. doi: 10.1111/j.1745-3933.2009.00621.x.

Alessandro Marconi and Leslie K. Hunt. The Relation between Black Hole Mass, Bulge Mass, and Near-Infrared Luminosity. ApJ, 589:L21–L24, May 2003. doi: 10.1086/375804.

André R. Martel, Stefi A. Baum, William B. Sparks, Eric Wyckoff, John A. Biretta, Daniel Golombek, Ferdinando D. Macchetto, Sigrid de Koff, Patrick J. McCarthy, and George K. Miley. Hubble Space Telescope Snapshot Survey of 3CR Radio Source Counterparts. III. Radio Galaxies with z<0.1. ApJS, 122(1):81–108, May 1999. doi: 10.1086/313205.

Paul Martini. QSO Lifetimes. In Luis C. Ho, editor, Coevolution of Black Holes and Galaxies, page 169, January 2004.

F. Massaro, D. E. Harris, G. R. Tremblay, D. Axon, S. A. Baum, A. Capetti, M. Chiaberge, R. Gilli, G. Giovannini, P. Grandi, F. D. Macchetto, C. P. O'Dea, G. Risaliti, and W. Sparks. Chandra Observations of 3C Radio Sources with z < 0.3: Nuclei, Diffuse Emission, Jets, and Hotspots. ApJ, 714:589–604, May 2010. doi: 10.1088/0004-637X/714/1/589.

F. Massaro, G. R. Tremblay, D. E. Harris, P. Kharb, D. Axon, B. Balmaverde, S. A. Baum, A. Capetti, M. Chiaberge, R. Gilli, G. Giovannini, P. Grandi, F. D. Macchetto, C. P. O'Dea, G. Risaliti, W. Sparks, and E. Torresi. Chandra Observations of 3C Radio Sources with z < 0.3. II. Completing the Snapshot Survey. The Astrophysical Journal Supplement Series, 203: 31, Dec 2012. doi: 10.1088/0067-0049/203/2/31.

Thomas A. Matthews, William W. Morgan, and Maarten Schmidt. A Discussion of Galaxies Indentified with Radio Sources. ApJ, 140:35, July 1964. doi: 10.1086/147890.

Nicholas J. McConnell and Chung-Pei Ma. Revisiting the Scaling Relations of Black Hole Masses and Host Galaxy Properties. ApJ, 764(2):184, February 2013. doi: 10.1088/0004-637X/764/2/184.

Nicholas J. McConnell, Chung-Pei Ma, Karl Gebhardt, Shelley A. Wright, Jeremy D. Murphy, Tod R. Lauer, James R. Graham, and Douglas O. Richstone. Two ten-billion-solar-mass black holes at the centres of giant elliptical galaxies. Nature, 480:215–218, December 2011. doi: 10.1038/nature10636.

B. R. McNamara and P. E. J. Nulsen. Heating Hot Atmospheres with Active Galactic Nuclei. ARAA, 45(1):117–175, September 2007. doi: 10.1146/annurev.astro.45.051806.110625.

D. L. Meier. A Magnetically Switched, Rotating Black Hole Model for the Production of Extragalactic Radio Jets and the Fanaroff and Riley Class Division. ApJ, 522(2):753–766, September 1999. doi: 10.1086/307671.

David L. Meier, Shinji Koide, and Yutaka Uchida. Magnetohydrodynamic Production of Relativistic Jets. Science, 291(5501):84–92, January 2001. doi: 10.1126/science.291.5501.84.

Andrea Merloni, Sebastian Heinz, and Tiziana di Matteo. A Fundamental Plane of black hole activity. MNRAS, 345(4):1057–1076, Nov 2003. doi: 10.1046/j.1365-2966.2003.07017.x.

Giulia Migliori, Paola Grandi, Giorgio G. C. Palumbo, Gianfranco Brunetti, and Carlo Stanghellini. Radio Lobes of Pictor A: An X-Ray Spatially Resolved Study. ApJ, 668:203–208, October 2007. doi: 10.1086/520870.

B. Mingo, J. H. Croston, M. J. Hardcastle, P. N. Best, K. J. Duncan, R. Morganti, H. J. A. Rottgering, J. Sabater, T. W. Shimwell, W. L. Williams, M. Brienza, G. Gurkan, V. H. Mahatma, L. K. Morabito, I. Prandoni, M. Bondi, J. Ineson, and S. Mooney. Revisiting the Fanaroff-Riley dichotomy and radio-galaxy morphology with the LOFAR Two-Metre Sky Survey (LoTSS). MNRAS, 488(2):2701–2721, September 2019. doi: 10.1093/mnras/stz1901.

H. Miraghaei and P. N. Best. The nuclear properties and extended morphologies of powerful radio galaxies: the roles of host galaxy and environment. MNRAS, 466:4346–4363, Apr 2017. doi: 10.1093/mnras/stx007.

Wenli Mo, Anthony Gonzalez, Mark Brodwin, Bandon Decker, Peter Eisenhardt, Emily Moravec, S. A. Stanford, Daniel Stern, and Dominika Wylezalek. The Massive and Distant Clusters of WISE Survey. VIII. Radio Activity in Massive Galaxy Clusters. ApJ, 901(2):131, October 2020. doi: 10.3847/1538-4357/abb08d.

Ben Moore, Neal Katz, George Lake, Alan Dressler, and Augustus Oemler. Galaxy harassment and the evolution of clusters of galaxies. Nature, 379(6566):613–616, February 1996. doi: 10.1038/379613a0.

Emily Moravec, Anthony H. Gonzalez, Simon Dicker, Stacey Alberts, Mark Brodwin, Tracy E. Clarke, Thomas Connor, Bandon Decker, Mark Devlin, Peter R. M. Eisenhardt, Brian S. Mason, Wenli Mo, Tony Mroczkowski, Alexandra Pope, Charles E. Romero, Craig Sarazin, Jonathan Sievers, Spencer A. Stanford, Daniel Stern, Dominika Wylezalek, and Fernando Zago. The Massive and Distant Clusters of WISE Survey. IX. High Radio Activity in a Merging Cluster. ApJ, 898(2):145, August 2020. doi: 10.3847/1538-4357/aba0b2.

R. Narayan, R. Mahadevan, and E. Quataert. Advection-dominated accretion around black holes. In M. A. Abramowicz, G. Björnsson, and J. E. Pringle, editors, Theory of Black Hole Accretion Disks, pages 148–182, January 1998a. doi: 10.48550/arXiv.astro-ph/9803141.

Ramesh Narayan and Jeffrey E. McClintock. Observational evidence for a correlation between jet power and black hole spin. MNRAS, 419(1):L69–L73, January 2012. doi: 10.1111/j.1745-3933.2011.01181.x.

Ramesh Narayan and Insu Yi. Advection-dominated Accretion: A Self-similar Solution. ApJ, 428:L13, June 1994. doi: 10.1086/187381.

Ramesh Narayan, Rohan Mahadevan, Jonathan E. Grindlay, Robert G. Popham, and Charles Gammie. Advection-dominated accretion model of Sagittarius A*: evidence for a black hole at the Galactic center. ApJ, 492(2):554–568, Jan 1998b. doi: 10.1086/305070.

Hagai Netzer. Revisiting the Unified Model of Active Galactic Nuclei. ARAA, 53:365–408, August 2015. doi: 10.1146/annurev-astro-082214-122302.

Peter Nilson. Uppsala general catalogue of galaxies. 1973.

R. Ojha, M. Kadler, M. Böck, R. Booth, M. S. Dutka, P. G. Edwards, A. L. Fey, L. Fuhrmann, R. A. Gaume, H. Hase, S. Horiuchi, D. L. Jauncey, K. J. Johnston, U. Katz, M. Lister, J. E. J. Lovell, C. Müller, C. Plötz, J. F. H. Quick, E. Ros, G. B. Taylor, D. J. Thompson, S. J. Tingay, G. Tosti, A. K. Tzioumis, J. Wilms, and J. A. Zensus. TANAMI: tracking active galactic nuclei with austral milliarcsecond interferometry . I. First-epoch 8.4 GHz images. A & A, 519:A45, September 2010. doi: 10.1051/0004-6361/200912724.

E. O'Sullivan, S. Giacintucci, L. P. David, M. Gitti, J. M. Vrtilek, S. Raychaudhury, and T. J. Ponman. Heating the Hot Atmospheres of Galaxy Groups and Clusters with Cavities: The Relationship between Jet Power and Low-frequency Radio Emission. ApJ, 735(1):11, July 2011. doi: 10.1088/0004-637X/735/1/11.

S. P. O'Sullivan, B. M. Gaensler, M. A. Lara-López, S. van Velzen, J. K. Banfield, and J. S. Farnes. The Magnetic Field and Polarization Properties of Radio Galaxies in Different Accretion States. ApJ, 806(1):83, June 2015. doi: 10.1088/0004-637X/806/1/83.

Frazer N. Owen and Robert A. Laing. CCD surface photometry of radio galaxies -I. FR class I and II sources. MNRAS, 238:357–378, May 1989. doi: 10.1093/mnras/238.2.357.

P. Padovani, D. M. Alexander, R. J. Assef, B. De Marco, P. Giommi, R. C. Hickox, G. T. Richards, V. Smolčić, E. Hatziminaoglou, V. Mainieri, and M. Salvato. Active galactic nuclei: what's in a name? The Astronomy and Astrophysics Review, 25(1):2, Aug 2017. doi: 10.1007/s00159-017-0102-9.

Paolo Padovani. The faint radio sky: radio astronomy becomes mainstream. The Astronomy and Astrophysics Review, 24(1):13, Sep 2016. doi: 10.1007/s00159-016-0098-6.

I. Pagotto, E. M. Corsini, E. Dalla Bontà, A. Beifiori, L. Costantin, V. Cuomo, L. Morelli, A. Pizzella, and M. Sarzi. Stringent limits on the masses of the supermassive black holes in seven nearby galaxies. Astronomische Nachrichten, 338(7):841–853, August 2017. doi: 10.1002/asna.201713370.

E. K. Panagoulia, A. C. Fabian, J. S. Sanders, and J. Hlavacek-Larrondo. A volume-limited sample of X-ray galaxy groups and clusters - II. X-ray cavity dynamics. MNRAS, 444(2):1236–1259, October 2014. doi: 10.1093/mnras/stu1499.

P. Parma, M. Murgia, R. Morganti, A. Capetti, H. R. de Ruiter, and R. Fanti. Radiative ages in a representative sample of low luminosity radio galaxies. A & A, 344:7–16, April 1999.

T. Pasini, M. Gitti, F. Brighenti, E. O'Sullivan, F. Gastaldello, P. Temi, and S. L. Hamer. A First Chandra View of the Cool Core Cluster A1668: Offset Cooling and AGN Feedback Cycle. ApJ, 911(1):66, April 2021. doi: 10.3847/1538-4357/abe85f.

V. Patiño-Álvarez, V. Chavushyan, J. León-Tavares, J. R. Valdés, A. Carramiñana, L. Carrasco, and J. Torrealba. Optical Spectrophotometric Monitoring of Fermi/LAT Bright Sources. arXiv e-prints, art. arXiv:1303.1893, March 2013.

J. A. Peacock, L. Miller, and M. S. Longair. The statistics of radio emission from quasars. MNRAS, 218:265–278, January 1986. doi: 10.1093/mnras/218.2.265.

E. Piconcelli, E. Jimenez-Bailón, M. Guainazzi, N. Schartel, P. M. Rodríguez-Pascual, and M. Santos-Lleó. The XMM-Newton view of PG quasars. I. X-ray continuum and absorption. A & A, 432(1):15–30, March 2005. doi: 10.1051/0004-6361:20041621.

Joanna M. Piotrowska, Asa F. L. Bluck, Roberto Maiolino, and Yingjie Peng. On the quenching of star formation in observed and simulated central galaxies: evidence for the role of integrated AGN feedback. MNRAS, 512(1):1052–1090, May 2022. doi: 10.1093/mnras/stab3673.

Planck Collaboration, P. A. R. Ade, N. Aghanim, M. Arnaud, M. Ashdown, J. Aumont, C. Baccigalupi, A. J. Banday, R. B. Barreiro, J. G. Bartlett, N. Bartolo, E. Battaner, R. Battye, K. Benabed, A. Benoît, A. Benoit-Lévy, J. P. Bernard, M. Bersanelli, P. Bielewicz, J. J. Bock, A. Bonaldi, L. Bonavera, J. R. Bond, J. Borrill, F. R. Bouchet, F. Boulanger, M. Bucher, C. Burigana, R. C. Butler, E. Calabrese, J. F. Cardoso, A. Catalano, A. Challinor, A. Chamballu, R. R. Chary, H. C. Chiang, J. Chluba, P. R. Christensen, S. Church, D. L. Clements, S. Colombi, L. P. L. Colombo, C. Combet, A. Coulais, B. P. Crill, A. Curto, F. Cuttaia, L. Danese, R. D. Davies, R. J. Davis, P. de Bernardis, A. de Rosa, G. de Zotti, J. Delabrouille, F. X. Désert, E. Di Valentino, C. Dickinson, J. M. Diego, K. Dolag, H. Dole, S. Donzelli, O. Doré, M. Douspis, A. Ducout, J. Dunkley, X. Dupac, G. Efstathiou, F. Elsner, T. A. Enßlin, H. K. Eriksen, M. Farhang, J. Fergusson, F. Finelli, O. Forni, M. Frailis, A. A. Fraisse, E. Franceschi, A. Frejsel, S. Galeotta, S. Galli, K. Ganga, C. Gauthier, M. Gerbino, T. Ghosh, M. Giard, Y. Giraud-Héraud, E. Giusarma, E. Gjerløw, J. González-Nuevo, K. M. Górski, S. Gratton, A. Gregorio, A. Gruppuso, J. E. Gudmundsson, J. Hamann, F. K. Hansen, D. Hanson, D. L. Harrison, G. Helou, S. Henrot-Versillé, C. Hernández-Monteagudo, D. Herranz, S. R. Hildebrandt, E. Hivon, M. Hobson, W. A. Holmes, A. Hornstrup, W. Hovest, Z. Huang, K. M. Huffenberger, G. Hurier, A. H. Jaffe, T. R. Jaffe, W. C. Jones, M. Juvela, E. Keihänen, R. Keskitalo, T. S. Kisner, R. Kneissl, J. Knoche, L. Knox, M. Kunz, H. Kurki-Suonio, G. Lagache, A. Lähteenmäki, J. M. Lamarre, A. Lasenby, M. Lattanzi, C. R. Lawrence, J. P. Leahy, R. Leonardi, J. Lesgourgues, F. Levrier, A. Lewis, M. Liguori, P. B. Lilje, M. Linden-Vørnle, M. López-Caniego, P. M. Lubin, J. F. Macías-Pérez, G. Maggio, D. Maino, N. Mandolesi, A. Mangilli, A. Marchini, M. Maris, P. G. Martin, M. Martinelli, E. Martínez-González, S. Masi, S. Matarrese, P. McGehee, P. R. Meinhold, A. Melchiorri, J. B. Melin, L. Mendes, A. Mennella, M. Migliaccio, M. Millea, S. Mitra, M. A. Miville-Deschênes, A. Moneti, L. Montier, G. Morgante, D. Mortlock, A. Moss, D. Munshi, J. A. Murphy, P. Naselsky, F. Nati, P. Natoli, C. B. Netterfield, H. U. Nørgaard-Nielsen, F. Noviello, D. Novikov, I. Novikov, C. A. Oxborrow, F. Paci, L. Pagano, F. Pajot, R. Paladini, D. Paoletti, B. Partridge, F. Pasian, G. Patanchon, T. J. Pearson, O. Perdereau, L. Perotto, F. Perrotta, V. Pettorino, F. Piacentini, M. Piat, E. Pierpaoli, D. Pietrobon, S. Plaszczynski, E. Pointecouteau, G. Polenta, L. Popa, G. W. Pratt, G. Prézeau, S. Prunet, J. L. Puget, J. P. Rachen, W. T. Reach, R. Rebolo, M. Reinecke, M. Remazeilles, C. Renault, A. Renzi, I. Ristorcelli, G. Rocha, C. Rosset, M. Rossetti, G. Roudier, B. Rouillé d'Orfeuil, M. Rowan-Robinson, J. A. Rubiño-Martín, B. Rusholme, N. Said, V. Salvatelli, L. Salvati, M. Sandri, D. Santos, M. Savelainen, G. Savini, D. Scott, M. D. Seiffert, P. Serra, E. P. S. Shellard, L. D. Spencer, M. Spinelli, V. Stolyarov, R. Stompor, R. Sudiwala, R. Sunyaev, D. Sutton, A. S. Suur-Uski, J. F. Sygnet, J. A. Tauber, L. Terenzi, L. Toffolatti, M. Tomasi, M. Tristram, T. Trombetti, M. Tucci, J. Tuovinen, M. Türler, G. Umana, L. Valenziano, J. Valiviita, F. Van Tent, P. Vielva, F. Villa, L. A. Wade, B. D. Wandelt, I. K. Wehus, M. White, S. D. M.

White, A. Wilkinson, D. Yvon, A. Zacchei, and A. Zonca. Planck 2015 results. XIII. Cosmological parameters. A & A, 594:A13, September 2016. doi: 10.1051/0004-6361/201525830.

Bianca M. Poggianti, Anja von der Linden, Gabriella De Lucia, Vandana Desai, Luc Simard, Claire Halliday, Alfonso Aragón-Salamanca, Richard Bower, Jesus Varela, Philip Best, Douglas I. Clowe, Julianne Dalcanton, Pascale Jablonka, Bo Milvang-Jensen, Roser Pello, Gregory Rudnick, Roberto Saglia, Simon D. M. White, and Dennis Zaritsky. The Evolution of the Star Formation Activity in Galaxies and Its Dependence on Environment. ApJ, 642(1):188–215, May 2006. doi: 10.1086/500666.

David Raban, Walter Jaffe, Huub Röttgering, Klaus Meisenheimer, and Konrad R. W. Tristram. Resolving the obscuring torus in NGC 1068 with the power of infrared interferometry: revealing the inner funnel of dust. MNRAS, 394(3):1325–1337, April 2009. doi: 10.1111/j.1365-2966.2009.14439.x.

C. S. Reynolds and A. C. Fabian. Warm absorbers in active galactic nuclei. MNRAS, 273(4):1167–1176, April 1995. doi: 10.1093/mnras/273.4.1167.

Christopher S. Reynolds. Measuring Black Hole Spin Using X-Ray Reflection Spectroscopy. Science & Space Review, 183(1-4):277–294, September 2014. doi: 10.1007/s11214-013-0006-6.

G. Risaliti and M. Elvis. A Panchromatic View of AGN. In A. J. Barger, editor, Supermassive Black Holes in the Distant Universe, volume 308 of Astrophysics and Space Science Library, page 187, August 2004. doi: 10.1007/978-1-4020-2471-9_6.

D. J. Saikia. Jets in radio galaxies and quasars: an observational perspective. Journal of Astrophysics and Astronomy, 43(2):97, December 2022. doi: 10.1007/s12036-022-09863-2.

Samir Salim, Janice C. Lee, Steven Janowiecki, Elisabete da Cunha, Mark Dickinson, Médéric Boquien, Denis Burgarella, John J. Salzer, and Stéphane Charlot. GALEX-SDSS-WISE Legacy Catalog (GSWLC): Star Formation Rates, Stellar Masses, and Dust Attenuations of 700,000 Low-redshift Galaxies. ApJS, 227(1):2, November 2016. doi: 10.3847/0067-0049/227/1/2.

Samir Salim, Médéric Boquien, and Janice C. Lee. Dust Attenuation Curves in the Local Universe: Demographics and New Laws for Star-forming Galaxies and High-redshift Analogs. ApJ, 859(1):11, May 2018. doi: 10.3847/1538-4357/aabf3c.

E. E. Salpeter. Accretion of Interstellar Matter by Massive Objects. ApJ, 140:796–800, August 1964. doi: 10.1086/147973.

Curtis J. Saxton, Kinwah Wu, Svetlana Korunoska, Khee-Gan Lee, Kai-Yan Lee, and Nicola Beddows. Time-dependent radio emission from evolving jets. MNRAS, 405(3):1816–1830, July 2010. doi: 10.1111/j.1365-2966.2010.16554.x.

M. Schmidt. 3C 273 : A Star-Like Object with Large Red-Shift. Nature, 197(4872):1040, March 1963. doi: 10.1038/1971040a0.

Carl K. Seyfert. Nuclear Emission in Spiral Nebulae. ApJ, 97:28, January 1943. doi: 10.1086/144488.

Stanislav S. Shabala, Nika Jurlin, Raffaella Morganti, Marisa Brienza, Martin J. Hardcastle, Leith E. H. Godfrey, Martin G. H. Krause, and Ross J. Turner. The duty cycle of radio galaxies revealed by LOFAR: remnant and restarted radio source populations in the Lockman Hole. MNRAS, 496(2):1706–1717, August 2020. doi: 10.1093/mnras/staa1172.

N. I. Shakura and R. A. Sunyaev. Reprint of 1973A&A....24..337S. Black holes in binary systems. Observational appearance. A & A, 500:33–51, June 1973.

T. W. Shimwell, C. Tasse, M. J. Hardcastle, A. P. Mechev, W. L. Williams, P. N. Best, H. J. A. Röttgering, J. R. Callingham, T. J. Dijkema, F. de Gasperin, D. N. Hoang, B. Hugo, M. Mirmont, J. B. R. Oonk, I. Prandoni, D. Rafferty, J. Sabater, O. Smirnov, R. J. van Weeren, G. J. White, M. Atemkeng, L. Bester, E. Bonnassieux, M. Brüggen, G. Brunetti, K. T. Chyży, R. Cochrane, J. E. Conway, J. H. Croston, A. Danezi, K. Duncan, M. Haverkorn, G. H. Heald, M. Iacobelli, H. T. Intema, N. Jackson, M. Jamrozy, M. J. Jarvis, R. Lakhoo, M. Mevius, G. K. Miley, L. Morabito, R. Morganti, D. Nisbet, E. Orrú, S. Perkins, R. F. Pizzo, C. Schrijvers, D. J. B. Smith, R. Vermeulen, M. W. Wise, L. Alegre, D. J. Bacon, I. M. van Bemmel, R. J. Beswick, A. Bonafede, A. Botteon, S. Bourke, M. Brienza, G. Calistro Rivera, R. Cassano, A. O. Clarke, C. J. Conselice, R. J. Dettmar, A. Drabent, C. Dumba, K. L. Emig, T. A. Enßlin, C. Ferrari, M. A. Garrett, R. T. Génova-Santos, A. Goyal, G. Gürkan, C. Hale, J. J. Harwood, V. Heesen, M. Hoeft, C. Horellou, C. Jackson, G. Kokotanekov, R. Kondapally, M. Kunert-Bajraszewska, V. Mahatma, E. K. Mahony, S. Mandal, J. P. McKean, A. Merloni, B. Mingo, A. Miskolczi, S. Mooney, B. Nikiel-Wroczyński, S. P. O'Sullivan, J. Quinn, W. Reich, C. Roskowiński, A. Rowlinson, F. Savini, A. Saxena, D. J. Schwarz, A. Shulevski, S. S. Sridhar, H. R. Stacey, S. Urquhart, M. H. D. van der Wiel, E. Varenius, B. Webster, and A. Wilber. The LOFAR Two-metre Sky Survey. II. First data release. A & A, 622:A1, February 2019. doi: 10.1051/0004-6361/201833559.

Jaejin Shin, Jong-Hak Woo, and John S. Mulchaey. A Systematic Search for X-Ray Cavities in Galaxy Clusters, Groups, and Elliptical Galaxies. ApJS, 227(2):31, December 2016. doi: 10.3847/1538-4365/227/2/31.

David A. Smith, Andrew S. Wilson, Keith A. Arnaud, Yuichi Terashima, and Andrew J. Young. A Chandra X-Ray Study of Cygnus A. III. The Cluster of Galaxies. ApJ, 565(1):195–207, January 2002. doi: 10.1086/324539.

Randall K. Smith, Nancy S. Brickhouse, Duane A. Liedahl, and John C. Raymond. Collisional Plasma Models with APEC/APED: Emission-Line Diagnostics of Hydrogen-like and Helium-like Ions. ApJL, 556(2):L91–L95, August 2001. doi: 10.1086/322992.

Domingos Savio De Lima Soares. Investigations of binary galaxies. 1989.

James F. Steiner, Jeffrey E. McClintock, and Ramesh Narayan. Jet Power and Black Hole Spin: Testing an Empirical Relationship and Using it to Predict the Spins of Six Black Holes. ApJ, 762(2):104, January 2013. doi: 10.1088/0004-637X/762/2/104.

Yuanyuan Su, Paul E. J. Nulsen, Ralph P. Kraft, William R. Forman, Christine Jones, Jimmy A. Irwin, Scott W. Randall, and Eugene Churazov. Buoyant AGN Bubbles in the Quasi-isothermal Potential of NGC 1399. ApJ, 847(2):94, October 2017. doi: 10.3847/1538-4357/aa8954.

Ralph S. Sutherland and M. A. Dopita. Cooling Functions for Low-Density Astrophysical Plasmas. ApJS, 88:253, September 1993. doi: 10.1086/191823.

C. N. Tadhunter, R. Morganti, A. Robinson, R. Dickson, M. Villar-Martin, and R. A. E. Fosbury. The nature of the optical-radio correlations for powerful radio galaxies. MNRAS, 298(4):1035–1047, August 1998. doi: 10.1046/j.1365-8711.1998.01706.x.

Clive Tadhunter. Radio AGN in the local universe: unification, triggering and evolution. Astronomy and Astrophysics Review, 24:10, June 2016. doi: 10.1007/s00159-016-0094-x.

Alexander Tchekhovskoy, Ramesh Narayan, and Jonathan C. McKinney. Black Hole Spin and The Radio Loud/Quiet Dichotomy of Active Galactic Nuclei. ApJ, 711(1):50–63, March 2010. doi: 10.1088/0004-637X/711/1/50.

Yuichi Terashima and Andrew S. Wilson. Chandra Snapshot Observations of Low-Luminosity Active Galactic Nuclei with a Compact Radio Source. ApJ, 583:145–158, January 2003. doi: 10.1086/345339.

Bryan A. Terrazas, Eric F. Bell, Joanna Woo, and Bruno M. B. Henriques. Supermassive Black Holes as the Regulators of Star Formation in Central Galaxies. ApJ, 844(2):170, August 2017. doi: 10.3847/1538-4357/aa7d07.

Nicole Thomas, Romeel Davé, Daniel Anglés-Alcázar, and Matt Jarvis. Black hole - Galaxy correlations in SIMBA. MNRAS, 487(4):5764–5780, August 2019. doi: 10.1093/mnras/stz1703.

Scott Tremaine, Karl Gebhardt, Ralf Bender, Gary Bower, Alan Dressler, S. M. Faber, Alexei V. Filippenko, Richard Green, Carl Grillmair, Luis C. Ho, John Kormendy, Tod R. Lauer, John Magorrian, Jason Pinkney, and Douglas Richstone. The Slope of the Black Hole Mass versus Velocity Dispersion Correlation. ApJ, 574:740–753, August 2002. doi: 10.1086/341002.

K. R. W. Tristram, K. Meisenheimer, W. Jaffe, M. Schartmann, H. W. Rix, Ch. Leinert, S. Morel, M. Wittkowski, H. Röttgering, G. Perrin, B. Lopez, D. Raban, W. D. Cotton, U. Graser, F. Paresce, and Th. Henning. Resolving the complex structure of the dust torus in the active nucleus of the Circinus galaxy. A & A, 474(3):837–850, November 2007. doi: 10.1051/0004-6361:20078369.

Ross J. Turner and Stanislav S. Shabala. Energetics and Lifetimes of Local Radio Active Galactic Nuclei. ApJ, 806(1):59, June 2015. doi: 10.1088/0004-637X/806/1/59.

Ross J. Turner, Jonathan G. Rogers, Stanislav S. Shabala, and Martin G. H. Krause. RAiSE II: resolved spectral evolution in radio AGN. MNRAS, 473(3):4179–4196, January 2018. doi: 10.1093/mnras/stx2591.

F. Ubertosi, M. Gitti, F. Brighenti, G. Brunetti, M. McDonald, P. Nulsen, B. McNamara, S. Randall, W. Forman, M. Donahue, A. Ignesti, M. Gaspari, S. Ettori, L. Feretti, E. L. Blanton, C. Jones, and M. Calzadilla. The Deepest Chandra View of RBS 797: Evidence for Two Pairs of Equidistant X-ray Cavities. ApJL, 923(2):L25, December 2021. doi: 10.3847/2041-8213/ac374c.

C. Megan Urry and Paolo Padovani. Unified Schemes for Radio-Loud Active Galactic Nuclei. Publications of the Astronomical Society of the Pacific, 107:803, September 1995. doi: 10.1086/133630.

M. P. Véron-Cetty and P. Véron. Are all radio galaxies genuine ellipticals? A & A, 375:791–796, September 2001. doi: 10.1051/0004-6361:20010902.

Nektarios Vlahakis and Arieh Königl. Magnetic Driving of Relativistic Outflows in Active Galactic Nuclei. I. Interpretation of Parsec-Scale Accelerations. ApJ, 605(2):656–661, April 2004. doi: 10.1086/382670.

J. V. Wall and J. A. Peacock. Bright extragalactic radio sources at 2.7 GHz- III. The all-sky catalogue. MNRAS, 216:173–192, September 1985. doi: 10.1093/mnras/216.2.173.

S. R. Ward, C. M. Harrison, T. Costa, and V. Mainieri. Cosmological simulations predict that AGN preferentially live in gas-rich, star-forming galaxies despite effective feedback. MNRAS, 514(2):2936–2957, August 2022. doi: 10.1093/mnras/stac1219.

Z. L. Wen and J. L. Han. Calibration of the Optical Mass Proxy for Clusters of Galaxies and an Update of the WHL12 Cluster Catalog. ApJ, 807(2):178, July 2015. doi: 10.1088/0004-637X/807/2/178.

W. L. Williams, M. J. Hardcastle, P. N. Best, J. Sabater, J. H. Croston, K. J. Duncan, T. W. Shimwell, H. J. A. Röttgering, D. Nisbet, G. Gürkan, L. Alegre, R. K. Cochrane, A. Goyal, C. L. Hale, N. Jackson, M. Jamrozy, R. Kondapally, M. Kunert-Bajraszewska, V. H. Mahatma, B. Mingo, L. K. Morabito, I. Prandoni, C. Roskowinski, A. Shulevski, D. J. B. Smith, C. Tasse, S. Urquhart, B. Webster, G. J. White, R. J. Beswick, J. R. Callingham, K. T. Chyży, F. de Gasperin, J. J. Harwood, M. Hoeft, M. Iacobelli, J. P. McKean, A. P. Mechev, G. K. Miley, D. J. Schwarz, and R. J. van Weeren. The LOFAR Two-metre Sky Survey. III. First data release: Optical/infrared identifications and value-added catalogue. A & A, 622:A2, February 2019. doi: 10.1051/0004-6361/201833564.

Chris J. Willott, Steve Rawlings, Katherine M. Blundell, and Mark Lacy. The emission line-radio correlation for radio sources using the 7C Redshift Survey. MNRAS, 309(4):1017–1033, Nov 1999. doi: 10.1046/j.1365-8711.1999.02907.x.

A. S. Wilson and E. J. M. Colbert. The Difference between Radio-loud and Radio-quiet Active Galaxies. ApJ, 438:62, January 1995. doi: 10.1086/175054.

A. S. Wilson, A. J. Young, and P. L. Shopbell. Chandra X-Ray Observations of Pictor A: High-Energy Cosmic Rays in a Radio Galaxy. ApJ, 547:740–753, February 2001. doi: 10.1086/318412.

Joshua D. Wing and Elizabeth L. Blanton. Galaxy Cluster Environments of Radio Sources. ApJ, 141(3):88, Mar 2011. doi: 10.1088/0004-6256/141/3/88.

Fu-Guo Xie and Feng Yuan. Radiative efficiency of hot accretion flows. MNRAS, 427(2):1580–1586, December 2012. doi: 10.1111/j.1365-2966.2012.22030.x.

Feng Yuan and Ramesh Narayan. Hot Accretion Flows Around Black Holes. ARAA, 52:529–588, August 2014. doi: 10.1146/annurev-astro-082812-141003.